LASER INTERFEROMETER GRAVITATIONAL WAVE OBSERVATORY
- LIGO -
CALIFORNIA INSTITUTE OF TECHNOLOGY
MASSACHUSETTS INSTITUTE OF TECHNOLOGY

Design Document **LIGO-T980068-00 - D** 7/29/98
Length Sensing & Control Subsystem Final Design
ISC team

Distribution of this draft:

LSC Final Design Review Board

This is an internal working note
of the LIGO Project.

California Institute of Technology
LIGO Project - MS 51-33
Pasadena CA 91125
Phone (818) 395-2129
Fax (818) 304-9834
E-mail: info@ligo.caltech.edu

Massachusetts Institute of Technology
LIGO Project - MS 20B-145
Cambridge, MA 01239
Phone (617) 253-4824
Fax (617) 253-7014
E-mail: info@ligo.mit.edu

WWW: http://www.ligo.caltech.edu/

LIGO-DRAFT

Contents

LIGO-DRAFT

LIGO-DRAFT

1 INTRODUCTION & SCOPE

The LIGO Detector Length Sensing and Control (LSC) subsystem is responsible for maintaining optical resonance in the interferometer such that a linear signal, proportional to metric strain, is available at the readout. To accomplish this, LSC must determine and control four independent length degrees of freedom and the laser wavelength, as shown in Figure 1. Each of these lengths must be held to an integral number of half-wavelengths of the laser light ($\lambda = 1.06\ \mu m$) with high accuracy, ranging from nm to less than .1 pm, to achieve the required precision in the strain read-out. The readout is derived from the correction signal required to counteract $\mathbf{L_-}$, the difference in the Fabry-Perot arm cavity lengths. In addition, LSC is required to provide means for calibrating this readout, and support diagnostic testing of LSC itself and of the detector as a whole.

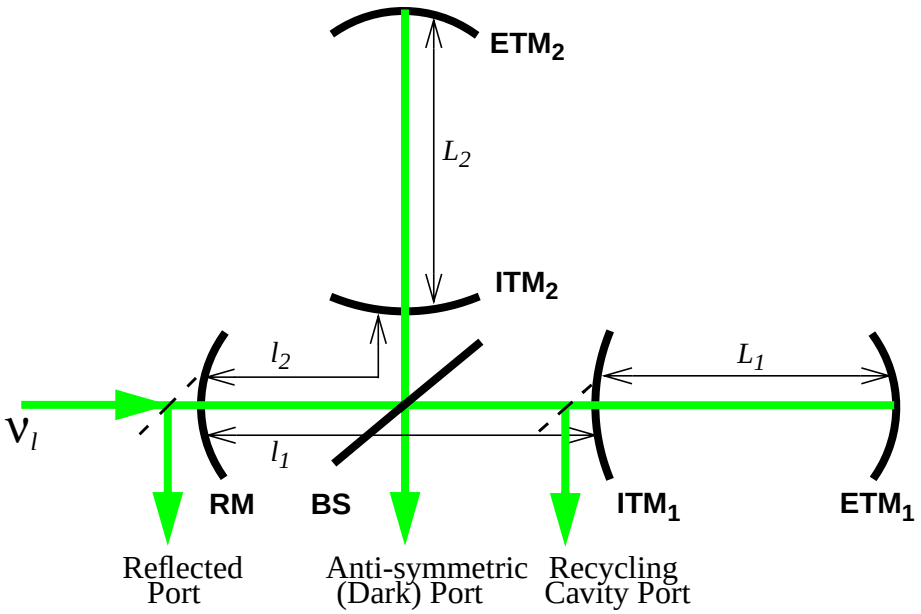

Name	*Symbols*[a]	*Definition*
Differential Arm Length	L_-, L_m	$L_1 - L_2$
Common Arm Length	L_+, L_p	$L_1 + L_2$
Michelson Length	l_-, l_m	$l_1 - l_2$
Recycling Cavity Length	l_+, l_p	$l_1 + l_2$
Michelson Asymmetry	Δl	$(l_1 - l_2)/2$

a. Unfortunately, different symbols for the same d.o.f. have been used in the documentation.

Figure 1 Definitions of length degrees-of-freedom and output ports. 'ITM' stands for input test mass, 'ETM' for end test mass, 'BS' for beamsplitter, and 'RM' for recycling mirror. The frequency, wavelength and propagation constant of the laser light is denoted by ν_l , λ_l , and k_l respectively.

LIGO DRAFT

These functions, operating modes, and much of the terminology used here are detailed in the *LSC Preliminary Design* LIGO-T970122-00-D. We refer the uninitiated reader to the introductory portions of that document for basic orientation; for brevity, we have not reproduced this material here.

The LSC system design is an integrated collective effort by ISC and CDS personnel.This document delineates the designs for control dynamics, signal conditioning, gain and noise allocation, dynamic reserve, diagnostics and other top-level functional aspects of the LIGO LSC subsystem. Detailed electronic design implementation will be covered in a separate (LSC/CDS) design document. However, practical electronic design constraints ultimately drive many of these top-level design choices, so we have necessarily assumed a very definite model for the implementation. These assumptions may need to be revisited in the course of the detailed electronics design, and are noted.

1.1. Design highlights & departures from prior design

Here we note some design highlights, and call attention to significant departures from the Preliminary Design (LIGO-T970122).

- **Digital controls:** The Pentek 6102 ADC/DAC module was selected for LSC controls and extensively characterized. The results allow an efficient allocation of whitening, dewhitening and digital filter functions, as described in Section 5. Also, a closed-loop digital control test was completed on the Phase Noise Interferometer with good results for noise, controllability, and robustness (matching those obtained with analog controls).
- **Modulation system:** We moved from a purpose-built high-performance oscillator to a commercial synthesizer (Marconi 2023), which offers greater diagnostic and initial tuning flexibility, reduced engineering investment and significantly lower cost. The principal disadvantage of off-the-shelf oscillators (excess residual AM) is addressed by a simple feedback stabilizer add-on; with this enhancement, a first article was demonstrated to meet all requirements (Section 2.2.).
- **Photodetectors:** An improved photodiode device (EG&G C30642G) was selected in place of the Hamamatsu part considered in the preliminary design. Its primary advantage is significantly lower junction capacitance. More exhaustive testing if this device, and a complete detector first-article system test at the PNI dark port (closely simulating LIGO operating conditions), were successfully completed (Section 2.1.).
- **Detection mode controls:** Extensive improvements to the detection-mode controls (Section 4) include:
  - An off-diagonal control path was introduced to increase the dark port's immunity from shot noise in the Michelson (*lm*) signal. Loosening this noise infiltration constraint allows much more robust gain distribution. Analysis of the sensitivity of the SNR to variation in plant parameters, once this off-diagonal gain has been set, indicates it is robust and non-critical.
  - A detailed model was incorporated for the common-mode feedback, including the dynamics of the combined mode cleaner/prestabilized laser "frequency actuator" and crossovers between mirror drive (Lp) and frequency actuation. A satisfactory trade-off between dynamic reserve of each actuation path and "true" frequency noise suppression factor was achieved.

LIGO-DRAFT

  - Phase margins have been increased to at least 50° in all loops.
  - Spurious coupling between common and differential modes due to plausible suspension drive imbalances were taken into account and accommodated in the design.
  - Resonant gain stages have been included to suppress the large (previously unanticipated) contribution of vertical bounce in the pendula. The largest coupling of this mode into optical pathlengths is through the vertical beam deflection introduced by the ITM wedges. A very simple IIR digital filter resonant gain stage was tested and proved to be extremely effective.

- **Lock Acquisition:** Lock acquisition threshold velocity has been improved by an order of magnitude, to approximately 3 μm/s, due to improvements in acquisition controller bandwidths, gain scheduling, and (very importantly) the SMAC simulation tool itself. Estimated mean-time-to-lock (MTTL) is now down to a few seconds. As a result, guided lock acquisition is not likely to be required and has been dropped from the baseline design (hooks are retained for a future addition, however).

LIGO-DRAFT

2 SENSING: PHOTODETECTION AND PHASE MODULATION

2.1. RF Photodetectors

LSC will provide RF Photodetector assemblies to detect the modulated output beam intensities corresponding to optical path length and light frequency changes in the interferometer. These photodetector assemblies are integrated with ASC Wavefront Sensing equipment and certain IO, PSL and COS components on external ISC platforms located in the LVEA's. Location-specific conditions for these applications are listed in Table 3. These positions corresponds to the reflected port (R), anti-symmetric or dark port (A) and recycling cavity pickoff port (P), plus the IO mode cleaner reflected port (MC). Figure 2 schematically depicts these locations for one interferometer (the Louisiana 4km; refer to D970308-A-D, *ISC Equipment Layout, Corner Station* for specific locations). No LSC RF detectors are deployed in mid- or end-stations.

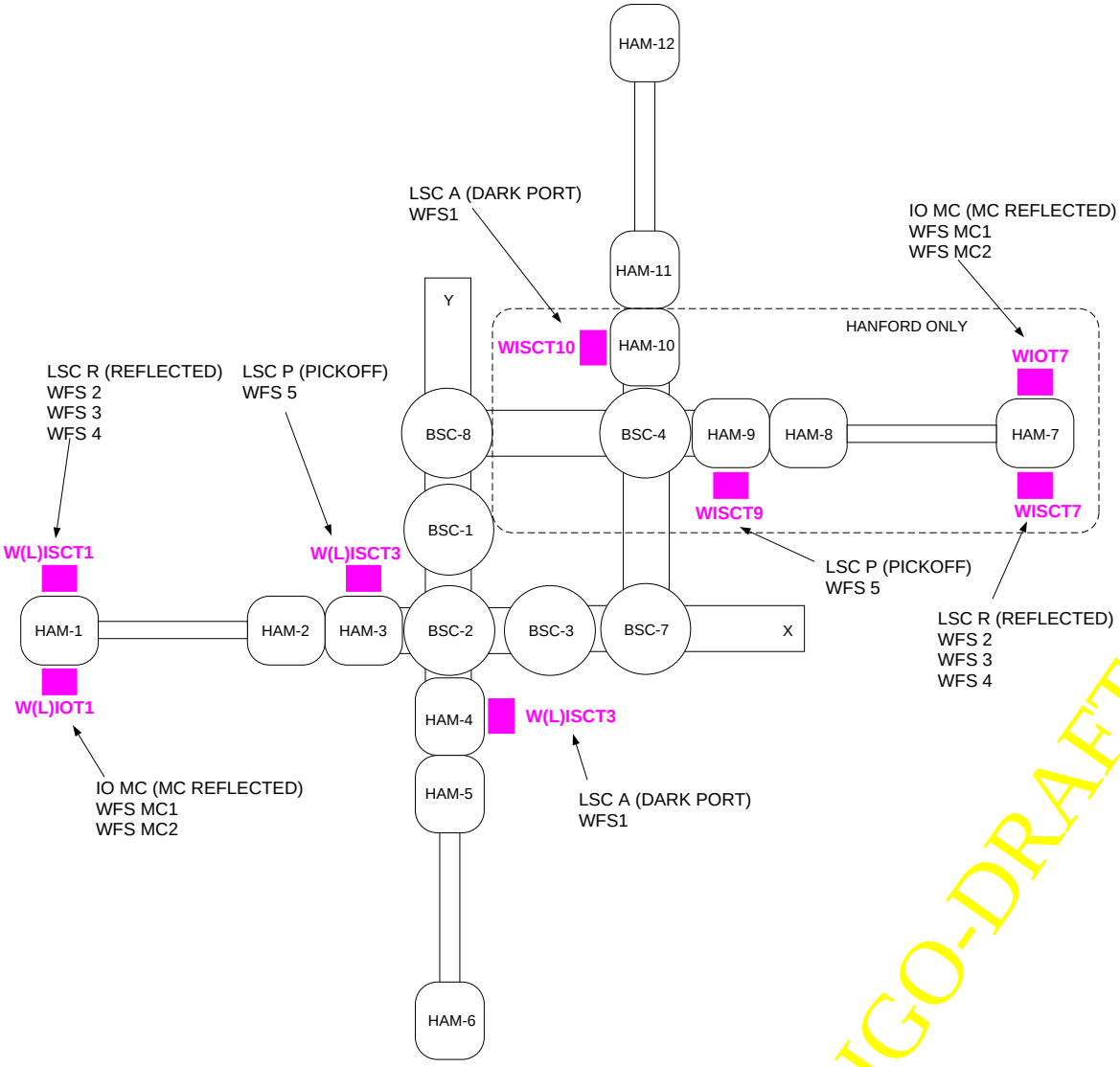

Figure 2: LSC equipment location schematic; vertex station at Hanford (Livingston designations in parentheses, except diagonal section as indicated).

LIGO-DRAFT

Length and frequency signals are encoded at the primary or "resonant" modulation frequency f_R for each interferometer. The frequency f_R is constrained by joint optical path length and RF wavelength conditions, as described in LIGO-T960122, *Proposed Initial Detector MC and RC Baseline Lengths* and LIGO-T970068-00-D, *Recycling Cavity and Mode Cleaner Cavity Baseline Dimensions*. The chosen modulation frequencies for 2 km and 4 km LIGO interferometers are as follows:

IFO	FSR_{MC} (MHz)	f_R (MHz)
WA, LA 4 km	12.231	24.463
WA 2 km	9.816	29.449

Table 1: Baseline frequencies for the resonant sidebands

In addition to the photodetector itself, LSC will provide an electromechanical shutter for diagnostics and redundant protection of equipment and personnel, as well as a fast electrooptic shutter (where required) for sensor protection. These actuators are integrated with the detector unit(s) into the ISC optics table.

Basic requirements for the photodetector system components are briefly summarized in Table 2. For discussion and derivations motivating these requirements, see T960058-03-D, *LSC Design Requirements.*:

Requirement	***Value***	***Driven by***
quantum efficiency[a]	> 80%	shot noise
steady-state power capacity	> 1.2 W	thermal lensing, coating figure
transient energy capacity	> 3 J	loss of lock transients, dark port
electronic noise	SRD/10	sensitivity
backscattering[b]	$x_{sc} \cdot m \cdot \sqrt{\mathrm{BRDF}} \le 2.4\times10^{-11}\,\mathrm{m\text{-}str^{-1/2}}/\sqrt{\mathrm{Hz}}$	scattered-field phase noise

Table 2: Photodetector system requirements summary (at dark port, except as noted)

a. Transmission efficiency of extra-vacuo COS telescopes, which are physically integrated with ISC components the external ISC tables, is regulated separately; see T970071-01-D, *COS Design Requirements*.

b. x_{sc} is the motion (spectral density) of the photodetector (w.r.t. the IFO optics); m is the ratio of the beam size at the beamsplitter to the beam size at the photodiode; and BRDF is the bidirectional-distribution function for the diode surface. Value holds for $f > 200$ Hz; see LSC DRD for details.

LIGO DRAFT

location (4k, 2k)	*port*	*CW locked (W)*	*CW unlocked (W)*	*transient energy (J)*	*transient pk. power (W)*	*atten. factor*	*no. PD modules req'd*
IOT1, 7	MC	.1	10	0.3	40	.3	1
ISCT1, 7	R	.1	6	0.3	24	.5	1
ISCT3, 9	P	.1	.01	~	~	1	1
ISCT4, 10	A	1.2	<.01	3	300	1	8

Table 3: Locations and approximate operating powers for LSC RF photodetectors. Attenuation factor and number of modules required for each location are discussed below. A total of 11 modules are required per LIGO interferometer (33 overall).

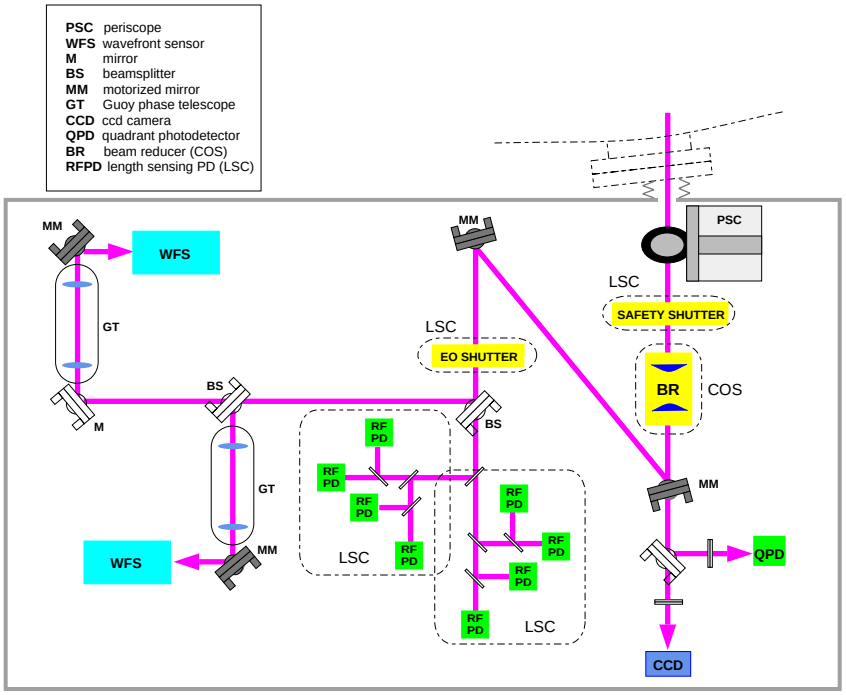

Figure 3: Schematic of ISC output table (dark port example shown) with approximate locations of LSC photodetectors, electrooptic and mechanical (safety) shutters, and beam division and relay optics.

LIGO-DRAFT

2.1.1. Photodiode Device Properties & Performance

The C30642G InGaAs PIN photodiode, manufactured by EG&G Canada Ltd., forms the basis of our photodetector module design. This device was selected through extensive survey and testing of electrical, optical and thermal properties of commercial photodiode devices (see LIGO-T980016-00-D, *LIGO Photodiode Selection* and VIRGO-PJT94-014, *Diodes selection, the first approach.*). It has a 2 mm diameter active photosensitive area and is packaged in a 3-lead TO-5

can with integral window. The window is removed to reduce losses and scattering (all optical properties cited below are measured without the window).

The following device parameters (Table 4) were obtained in laboratory measurements of sample diodes. Electrical and thermal properties are defined in the equivalent circuit models shown in Figure 4.

parameter	*symbol*	*value*	*units*	*notes*
1064 nm responsivity	***R***	0.71 ± .03	A/W	window removed
external quantum efficiency	η	83 ± 3	%	derived from ***R***
1064 nm surface reflectance	R	2	%	10° inc., P pol.
1064 nm backscatter	BRDF	$3.7 * 10^{-5}$	sr^{-1}	2.5° inc., 6.5° scat.
surface microroughness	σ_z	2.8	nm_{rms}	over 10 X 10 μm area
jct.-case thermal impedance	Θ_{jc}	17	°C/W	
jct. thermal time constant	τ_{jc}	0.16	s	
junction capacitance	C_d	70	pF	@ 10 VDC bias, 25°C
		85	pF	@ 5 VDC bias, 25°C
		140	pF	@ 1 VDC bias, 25°C
series resistance	R_d	9	Ω	(~bias-independent)
capacitance temp. coeff.	α_C	+0.04	pF/°C	avg., 20°C - 100°C

Table 4: Typical measured properties of sample EG&G C30642G 2mm InGaAs PIN diodes.

2.1.1.1 Electrical properties & minimum photocurrent per diode

We use a passive resonant LC transimpedance followed by a high-impedance, low noise voltage amplifier; because a large fraction of the average optical power can be contained in the $2f_R$ component, a notch filter at $2f_R$ is also included, prior to the amplifier, to avoid saturation (Figure 5). The diode capacitance C_d is resonated with an inductor L chosen to give the proper frequency $f_R = \omega_R/(2\pi)$. The output voltage corresponding to a given photocurrent modulation at f_R is proportional to the effective transimpedance $Z(f_R) \equiv Z_R$. This transimpedance also induces a thermal (Johnson) noise current density $e_{th} = \sqrt{4kTZ_R}$. The total electronic and thermal noise (assuming only the "front end" contributes) is then $e_\Sigma^2 = e_n^2 + i_n^2 Z_R^2 + 4kTZ_R$. We require that the

LIGO-DRAFT

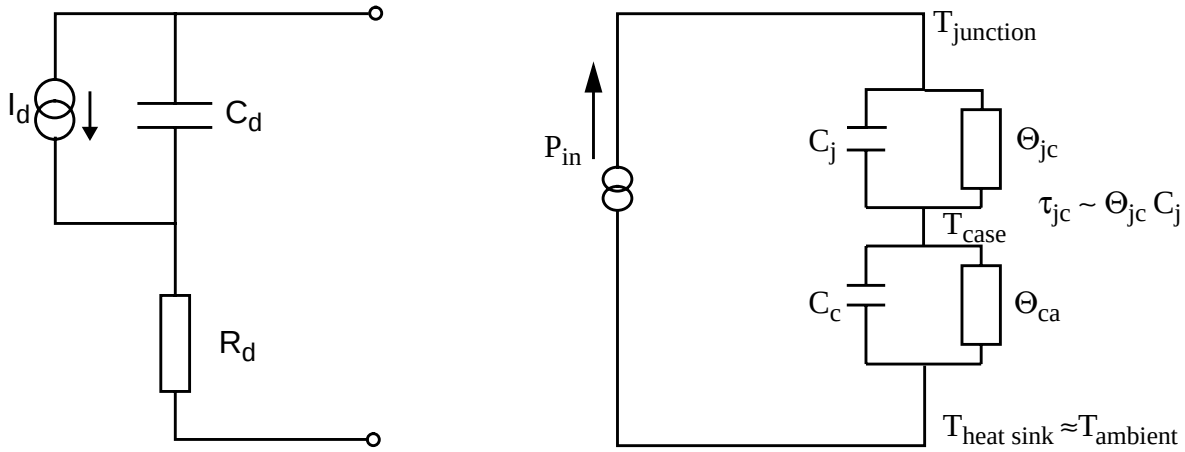

Figure 4: PD Equivalent circuit models for RF impedance (left) and thermal properties (right).

shot noise in the mean photocurrent per diode $\bar{I}$ must exceed this electronic noise by a factor of ten in amplitude, or $e_{shot}^2 = 2q\bar{I}Z_R^2 \geq 100\ e_\Sigma^2$ in power[1].

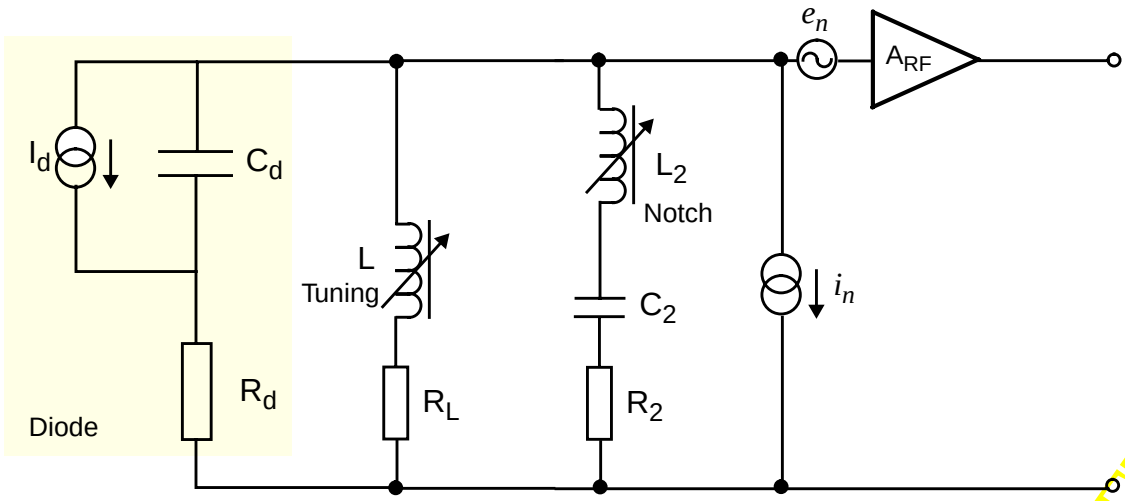

$$\frac{1}{Z(s)} = \frac{1}{R_d + \frac{1}{sC_d}} + \frac{1}{sL + R_L} + \frac{1}{R_2 + \frac{1}{sC_2} + sL_s}$$

Figure 5: Simplified photodiode-preamp equivalent RF circuit. The series L2-C2 notch is tuned for $2f_R$ and the inductor L is tuned to give a resonance at f_R; R_L and R_2 are included to account for losses in the inductors. The transimpedance of the circuit is Z as given in the above expression, where $s = 2\pi i f$. e_n and i_n are the amplifier equivalent voltage and current noise generators.

LIGO-DRAFT

The measured resonant impedance is typically $Z_R \approx 225\Omega$ for 7V bias and operating frequency f_R = 25 MHz . The Maxim 4107 "ultra-low-noise" 350 MHz operational amplifier offers e_n = 0.75 nV/$\sqrt{\text{Hz}}$ and i_n = 1.2 pA/$\sqrt{\text{Hz}}$ at this frequency (note that this component choice leaves the noise budget dominated by the thermal noise from Z_R). These numbers lead to a minimum of $\bar{I} > 26.5$ mA per device. For comparison, the 1.2W CW expected at the LIGO dark port (*W. Kells, private communication*) will induce a total photocurrent of 850 mA. Note, however, that we have assumed no noise is added downstream of the preamplifier, and that all electronic (and thermal) noise sources are independent like their corresponding shot noise currents. At the dark port we therefore choose to allocate at least $\bar{I} > 50$ mA per diode to insure adequate margin.

2.1.1.2 Linearity, damage threshold and number of discrete devices.

For economy, we of course prefer to use the minimum number of discrete photodiodes for each port. The maximum power per diode is influenced by linearity and device damage threshold. In principle, spatial distribution of power (power surface density) will also play a part in both linearity and damage. Tests on similar devices (see LIGO-T980016-00-D) suggest that, at least at power levels under 200 mW CW, RF and DC nonlinearity are only weakly related to beam diameter over the range between 0.3 and 2 mm, providing sufficient reverse bias is maintained at the active region. However, the contribution of backscattered light to interferometer phase noise is expected to be proportional to beam radius (for a given microroughness and reflectance). We also expect damage phenomena to have some inverse relation to beam size. As a result we choose the largest diode diameter (2 mm) consistent with adequate electrical impedance.

The expected amplitude modulation at frequency f_R in the LIGO dark port photocurrent is about 0.1% RMS. With comparable modulation imposed by an electrooptic modulator on a 1064 nm laser probe beam, the EG&G C30642G showed less than 5% deviation from linearity up to the maximum test power of 250 mW. We can actually attribute some of the small deviation seen at this power to reduction in the effective junction bias voltage (due to substrate series resistance) and increased junction temperature. Both of these effects are observed to reduce the readout gain by increasing the junction capacitance, thus detuning the resonant LC circuit (see below).

While this is encouraging, direct amplitude modulation tests are a crude probe of nonlinear diode behavior. Strong (nearly 100%) photocurrent modulation at $2f_R$ and significant low-frequency modulation of the envelope (dark fringe deviations arising from seismic noise) will also be present in the real antisymmetric-port signal. A diode was therefore tested under conditions closely simulating those in LIGO, using the LIGO Phase Noise Interferometer (PNI). An early prototype LIGO detector employing a single C30642G coupled to a Maxim 4107 preamplifier was used in this interferometer (*Brian Lantz Ph.D. thesis, in preparation; PNI IR paper, in preparation*). A shot-noise limited phase error spectrum was obtained between 200 and 2000 Hz (Figure 10), with an average photocurrent of 32 mA. While some excess low-frequency noise remains unexplained, this demonstration strongly constrains possible intermodulation, upconversion and downconversion noise processes under realistic LIGO conditions.

We thus feel confident we can allocate 150 mW CW per diode without degradation or excess noise. The detection system will optically divide the dark port power equally among 8 diodes such

1. the non-stationary nature of the shot noise actually increases the shot noise component (after demodulation) by 10-20%; we're neglecting this to arrive at a slightly conservative number for minimum *I*.

LIGO-DRAFT

that each detector operates at approximately 150 mW (or $I \approx 107$ mA). At 7 V bias the junction temperatures will equilibrate around 18C above ambient (assuming the case is externally heat-sinked at 3 C/W).

This temperature rise will cause about a 1% increase in junction capacitance (Figure 7). An additional increase of about 4% in capacitance is caused by reduction of the effective bias (Figure 6) due to the internal resistive drop $\bar{I}R_d \approx 1$ V between the junction and device leads. If uncompensated, these two effects will pull the resonant frequency of the LC transimpedance circuit down by 2.5%, causing a change in the relative phase of the RF transfer function of approximately 7 degrees. To compensate this change, we plan to use the following strategies:

- pre-tune the LC circuit to anticipate the shift (which is highly repeatable), and/or
- set the bias voltage regulator for each diode to slightly increase the bias with increasing current (rather than maintaining a fixed voltage). This will have a compensating effect on the capacitance, in principle nulling both the thermal and IR components of the shift.

The circuit design is compatible with both options.

LIGO-DRAFT

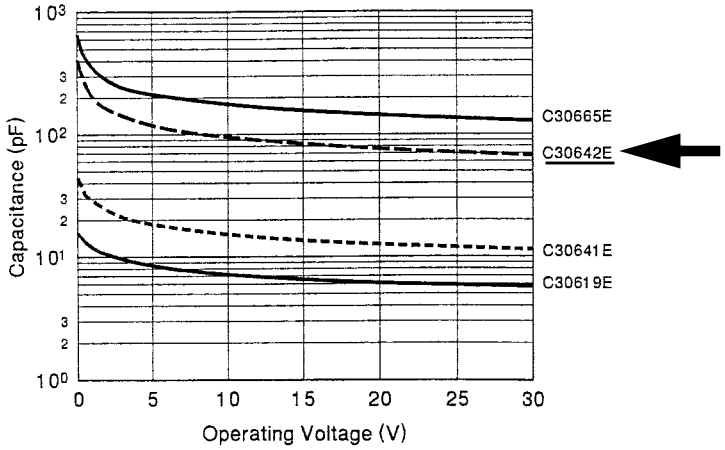

Figure 6: Typical junction capacitance variation of EG&G InGaAs PIN photodiodes as a function of reverse bias V_b (taken from EG&G data sheet). The 2 mm C30642 is second from the top.

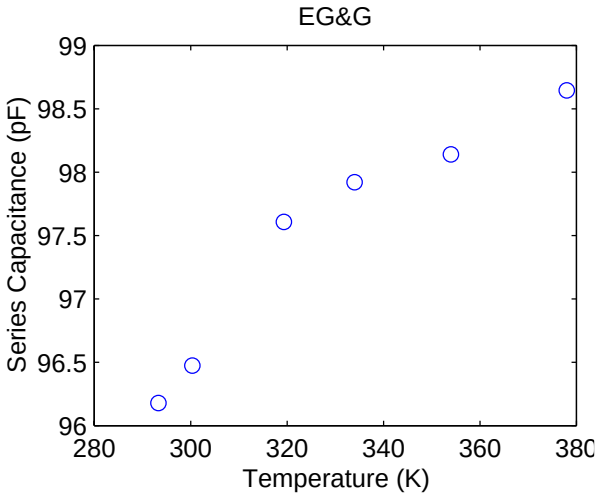

Figure 7: Measured temperature dependence of EG&G C30642G junction capacitance at 9V reverse bias. Stray capacitance of the test jig (estimated at about 10 pF) was not subtracted.

LIGO-DRAFT

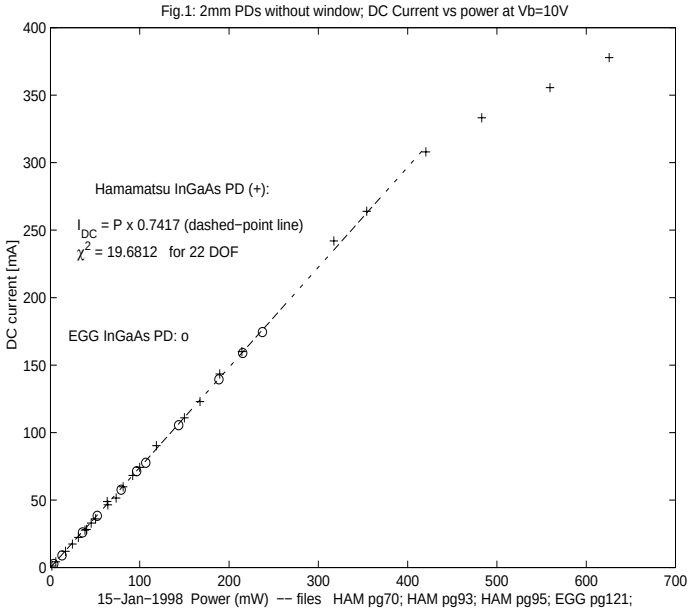

Figure 8: DC photocurrent response of EG&G C30642G photodiode vs. incident power at 1064 nm (o). Bias voltage is 10 V; spot diameter is approximately 0.7 mm. Performance of a Hamamatsu G5832-2 diode (tested to higher power) is also plotted for comparison (+).

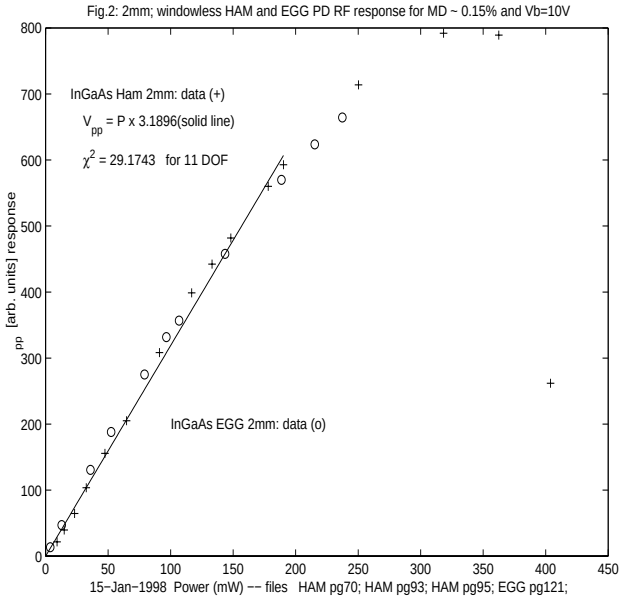

Figure 9: RF response of EG&G C30642G photodiode with 0.15% amplitude modulation at 25 MHz, using a readout circuit tuned at low power (o). Bias voltage across the device leads was held constant at 10V. No compensation for internal voltage drop or temperature rise were applied. Both effects detune the readout circuit at high current, causing apparent gain compression. Data for Hamamatsu G5832-2 are also plotted (+).

LIGO-DRAFT

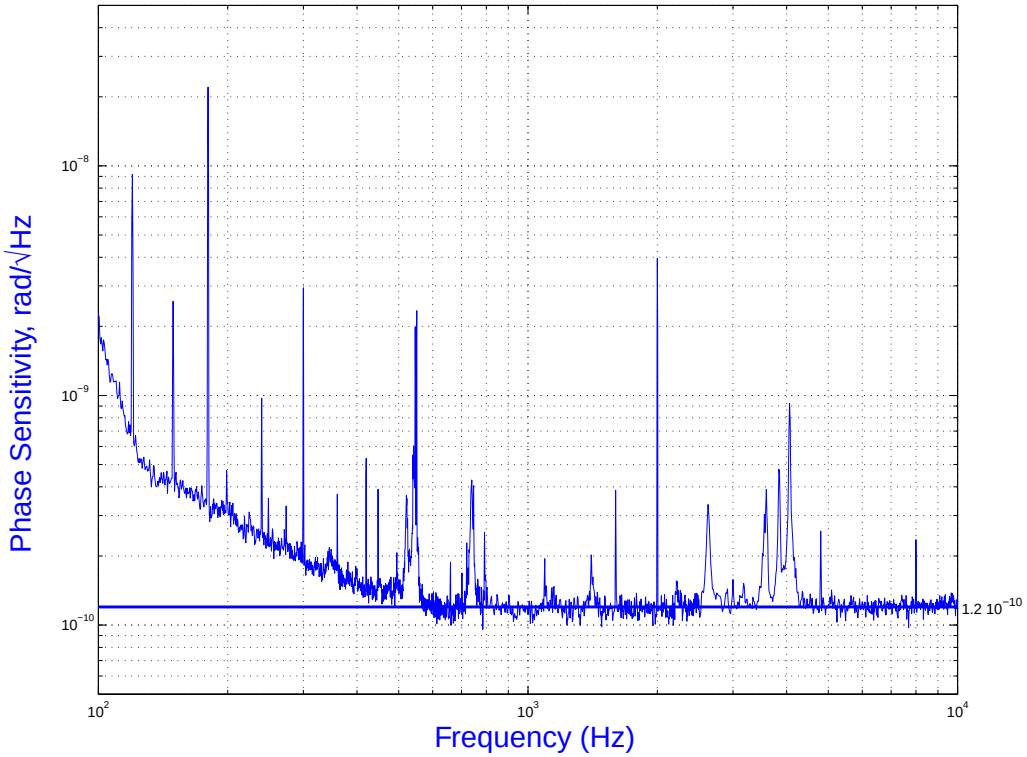

Figure 10: PNI phase noise spectrum obtained using EG&G C30642G photodiode at the dark port. Operating current was approximately 32 mA (compared with 106 mA expected in each LIGO diode). Approximately half the power is in the carrier, and half in the sidebands.

2.1.1.3 Transient power handling

On loss of lock, stored energy circulating in interferometer cavities is released to the output ports and may damage LSC and ASC sensors. Three important transient situations have been identified:

- **Loss of differential (Lm, lm) control.** Saturation or other disturbances causing a large differential phase excursion (of order π/2 or greater) will dump the circulating cavity energy out through the dark port. The timescale for onset of this transient is dependent on the nature of the disturbance; in the extreme limit of a stepwise differential phase shift of π/2, the instantaneous output power output can approach the circulating power in the recycling cavity, of order 300 W. The decay time is at least as long as energy storage time in the arm cavities, but may be longer. The total emitted energy is bounded by the stored energy in the interferometer, approximately 3 J.
- **Loss of Lp control.** The common-mode R output port will emit the full input power (~ 6W) continuously whenever the laser/mode cleaner is locked but the interferometer is not. This is the default condition during startup, alignment and many diagnostic conditions. In addition, a temporary excursion to approximately a factor of four greater power (~ 24 W) occurs when the common-mode loop unlocks, due to constructive interference of the incident and internally stored fields. This transient may have a risetime as short as a few microseconds. There

LIGO-DRAFT

will be an oscillatory fluctuation whose frequency depends on the rate of change of relative laser phase after the unlocking event. The falling envelope of this waveform corresponds to the amplitude storage time of the recycling cavity.

- **Loss of laser/mode cleaner control.** The reflected light from the mode cleaner acts similarly on loss of laser frequency lock.

These transients have detailed behaviors which depend on the nonlinear dynamics of the unlocking disturbance and on the control systems' detailed (and nonlinear) reactions to it. Some of this behavior has been investigated and was discussed in Appendix C of *Length Sensing and Control Preliminary Design*, LIGO-T979122-00-D.

For the purpose of determining the effect on LSC sensors, however, we can approximate the actual power transient as a simple square pulse, carrying the expected energy. Figure 11 shows the peak temperature of the junction as a function of the pulse duration over which this energy is distributed. The thermal time constants of the diodes are too long for conduction to the case and heatsink to remove significant heat during the expected transient durations (< .1 s). As a result the peak temperature is essentially determined by the deposited energy and the mass and specific heat, i.e. the "thermal capacitance" (Figure 4), of the InGaAs die. This thermal capacitance is given by $C_j = \tau_j / \Theta_j$.

Unfortunately, this quantity is relatively small for the chosen device. In the limit of very short pulses, the maximum temperature rise is given by $\Delta T_j(\tau_{pulse} \to 0) = E_{pulse} \cdot \Theta_j / \tau_j \approx E_{pulse} \cdot 106°\mathrm{C/J}$ for the measured EG&G diode parameters.

The deposited energy comprises two components, direct laser energy and Joule heat from the developed photocurrent. With fixed bias voltage V_b = 10 V and responsivity R = 0.71 A/W, the dissipated power in the die would be $P_j = P_l \cdot (1 + RV_b) \approx 8.1 P_l$, leveraging the incident power with significant electrical dissipation. This is mitigated by electronically clamping the developed photocurrent at a fixed value I_c somewhat above the quiescent photocurrent for normal operation, using a current sensing bias circuit. The instantaneous power dissipation is then reduced (assuming the critical power $P_c = I_c/R$ is exceeded) to $P_j = P_l + I_c^2 R_d \approx P_l + 0.36\,W$ for I_c = 200 mA and R_d = 9 Ω.

With this bias clamp in place, and 8 diodes sharing the total dark port power, a "worst case" dark-port unlocking event (dissipating 3 J in 10 milliseconds, about 300 W at peak) would still induce a temperature spike of approximately 40C above the quiescent level in each diode, thus reaching a peak junction temperature of 86C. We have not accumulated adequate destructive-testing experience to determine the diodes' precise thermal damage threshold, especially for repetitive exposures. Anecdotal evidence[1] suggests damage (in the form of a "soft" increase in leakage current) has occurred for continuous exposures at 100C. As a result, we will provide a fast shutter (response time < 1 ms) to protect the dark port detectors. After sufficient operating experience is

1. A. Marin, private communication.

LIGO-DRAFT

acquired, and unlocking transients have been better characterized, it may prove possible to eliminate this lossy element and obtain increased quantum efficiency.

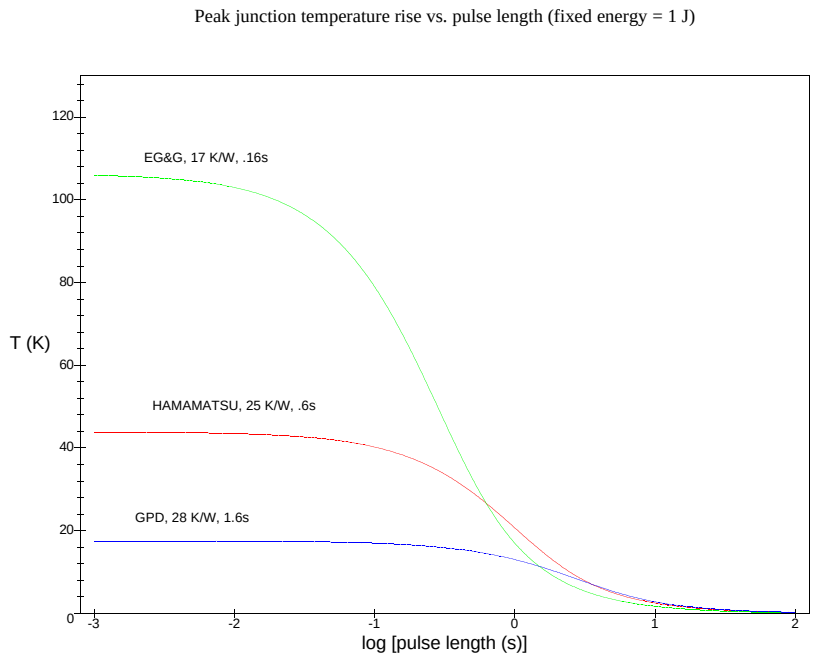

Figure 11: Calculated peak junction temperature rise above ambient vs. pulse length in EG&G C30642G, Hamamatsu G5832-2 and GPD GAP-2000 2 mm- diameter InGaAs photodiodes for 1 Joule (total dissipated) rectangular pulse. Based on measured Θ_{jc} and τ_{jc} (Table 4).

The reflected ports have somewhat different protection requirements. Although the pulse energies are smaller for the expected transients, the CW exposure when “unlocked” exceeds the normal operating power by orders of magnitude. To allow these detectors to operate during acquisition, and still accept the full available power in operation (required for shot noise SNR), it is necessary to keep the incident power within the range of linearity in both states. A shutter which can change its transmission over a wide dynamic range during a short transition time (of order .1 ms or less) is required.

It turns out both applications for shuttering are satisfied by an electrooptic shutter (Section 2.1.3.).

2.1.1.4 Optical backscattering & reflectance

Backscattering of light from vibrating extra-vacuo components has been identified as a potential noise source in LIGO (see *Core Optics Support Preliminary Design*, T980010-01-D and the LSC DRD, T960058-03-D). The photodiode itself is of particular concern for two reasons; its surface roughness is neither especially good nor readily controllable, and the beam diameter is smallest where it encounters the diode. The scattering was measured at 1064 nm wavelength, with an inci-

LIGO DRAFT

dence angle of 2.5 degrees. Although it isn't the lowest backscatter of the three devices tested, the EG&G diode meets our requirement (Table 2).

Diode	***BSDF (BRDF) at 6.5°*** (10^{-4}***/ster)***
Hamamatsu (G5832-2)	1.1
EG&G (C30642G)	0.37
GPD (GAP2000)	0.11

Table 5: 2mm Diode Backscatter

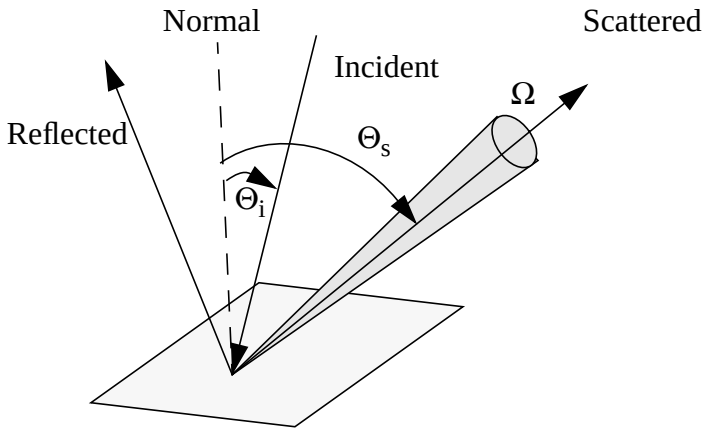

Figure 12: Definition of BSDF angles used in this document.

In principle backscatter is determined by the surface roughness, which can be measured separately. At this point we do not have good quantitative agreement between the predicted BRDF from microroughness measurements (made with an atomic force microscope) and the measured optical BRDF. However, the ranking of the three tested devices according to submicron-scale microroughness does at least agree qualitatively with the ranking deduced from the measured BRDF's.

The total backscatter budget must include not only the primary scatter from the diode surface, but any secondary scatter from specular reflections. Figure 13 shows the measured reflectance coefficient vs. angle of incidence for a sample EG&G diode, using both S and P polarization. Just over 2% of the incident power is specularly reflected near normal incidence. A high-quality beam dump will absorb this reflection to prevent multipath contamination of the detector signal.

LIGO-DRAFT

The 2% reflection coefficient could be improved; for comparison, in Figure 14 we show the corresponding reflectance trace for the Hamamatsu G5832-2, which has a much better AR coating (but poorer electrical properties and, surprisingly, about the same external quantum efficiency).

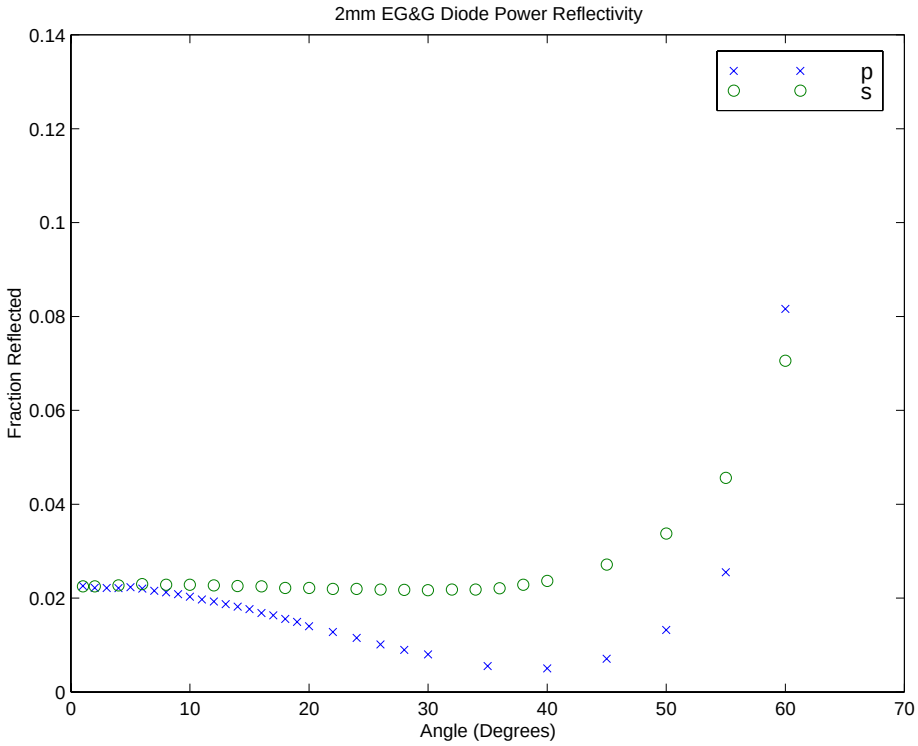

Figure 13: EG&G Diode Reflectivity

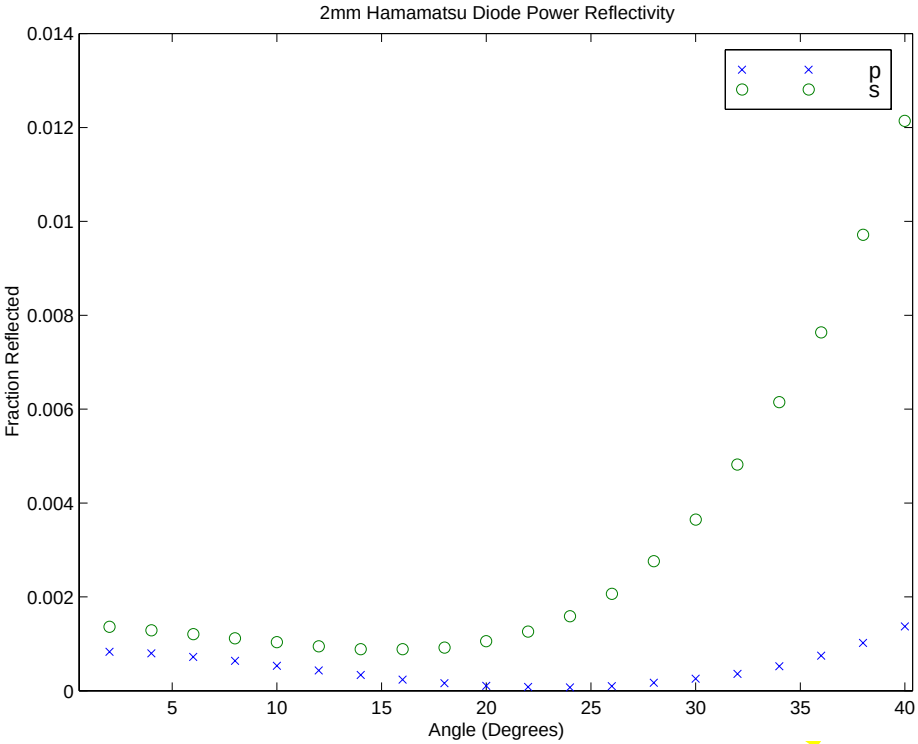

Figure 14: Hamamatsu Diode Reflectivity.

We now estimate the backscattered light phase noise contribution and compare with the requirements (Table 2). The motion of the diode surface x_{sc} is the least well-known quantity, but we estimate that a conservative level is $10^{-11}\,\mathrm{m}/\sqrt{\mathrm{Hz}}$ for f > 200 Hz. At these frequencies acoustical noise will be the driving force, and we plan on enclosing the ISC tables with an acoustical enclosure. One example under consideration is the Environmental Isolation Enclosure from Data Optics (`www.dataoptics.com/enclosures.htm`).

We choose a beam radius at the photodiode surface of 0.35 mm, so that m = 100. Then $x_{sc} \cdot m \cdot \sqrt{\mathrm{BRDF}} \cong 6\times10^{-12}\,\mathrm{m\text{-}str^{-1/2}}/\sqrt{\mathrm{Hz}}$, which is a factor of 4 below the requirement.

2.1.2. Photodetector Design

Each individual photodiode will be individually packaged in an RF-tight enclosure. The diode case is thermally bonded to an air-cooled heat sink which also forms part of the RF boundary. The enclosure (Figure 15) is electrically isolated from the ISC optical table by use of insulating spacers and screw bushings.

The dark port system, which uses 8 modules, employs 7 low-loss beamsplitters to divide the beam in 8 equal parts. Each diode is located at the same focal distance from the common input to simplify beam shaping and to minimize possible optical backscatter interference effects.

The beam diameter on each diode will be between 0.7 mm, to reduce backscattering from the die edges and contact region. Each diode will be angled 5-10 degrees away from normal about a vertical axis to direct the 2% specular reflection onto a low-scatter beam dump.

It turns out it is not practical or cost-effective to introduce an incoherent (light bulb) calibration source into the diode package (200W or larger lamps are needed to attain photocurrents comparable to operating levels). This function will be assumed by a separate off-line test rig. Initial setup, tuning and gain factors will be established and subsequently verified *in situ* by electrical (test input) transfer function measurements and, where necessary, scans using a calibrated 980 nm modulated laser diode. These methods proved adequate and reasonably efficient during the PNI experiment.

Each photodetector includes a DC readout, with a bandwidth of DC to >100 kHz. This output provides the interferometer diagnostic functions of DC monitoring of power levels, as well as monitoring of laser power fluctuations in the GW-band (at the anti-symmetric, recycling cavity, and reflected ports; the ETM transmission ports are monitored by ASC detectors). The DC readout has sufficient sensitivity to to measure shot-noise of a DC photocurrent of 100 ma, with a signal-to-noise ratio of ~2 (a ~15 ohm load is used, so that shot-noise from I_{dc} = 100ma produces roughly 2.7 nV/√Hz; an ultra-low noise op-amp is used as a preamp).

LIGO-DRAFT

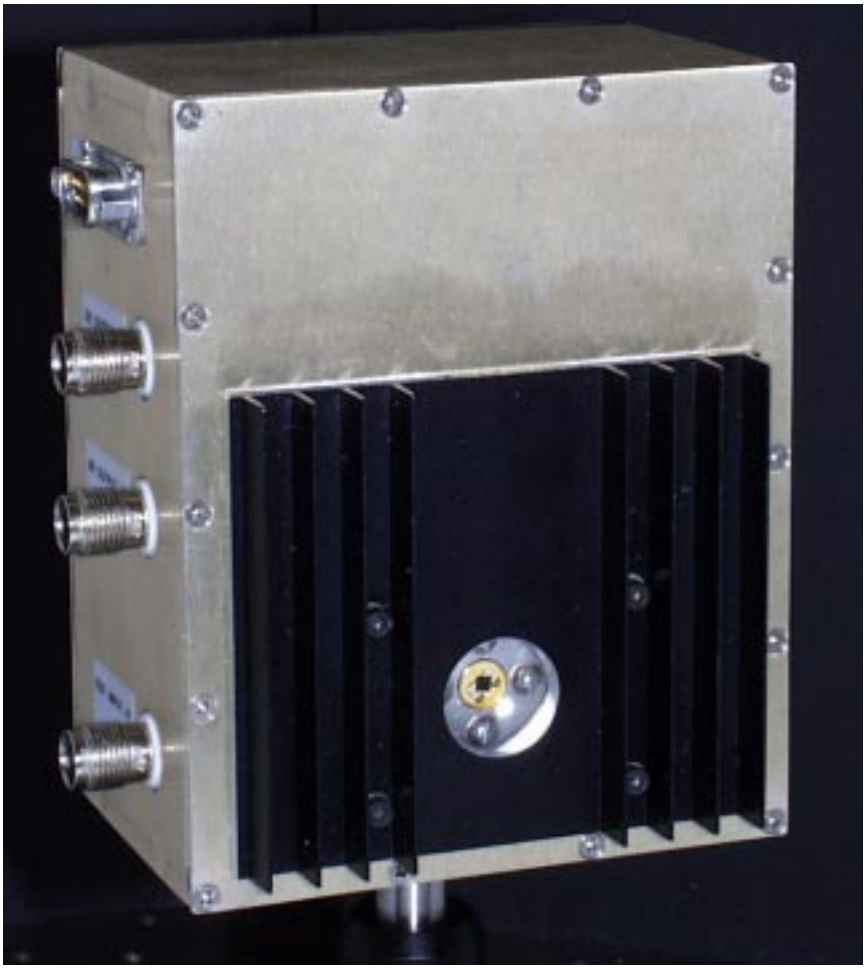

Figure 15: LIGO RF photodetector head. Overall dimensions are 125 mm (5”) H X 100 mm (4”) W x 67 mm (2.5”)D, excluding the face-mounted heat sink and side connector projections. The laser aperture is centered 25.4 mm (1”) above the lower mounting plane. Coaxial connectors are provided for RF and DC photocurrent output signals and for RF test input; a multipin connector (top) is used for power, control and remote monitoring of a heatsink-mounted thermistor. (Courtesy of LIGO CDS group.)

2.1.3. Electro-optic Shutter Design

We have chosen to implement an electro-optic shutter for two main reasons:

- speed of response compared to a mechanical shutter (a piezo-actuated beam deflector may be fast enough, but it doesn’t have the second advantage ...)
- controllable attenuation; an E-O shutter is really a controllable attenuator – this feature is needed prior to lock acquisition for the mode cleaner and IFO reflected photodetectors

LIGO-DRAFT

The components of the E-O shutter are shown in Figure 16. A small fraction of the beam is

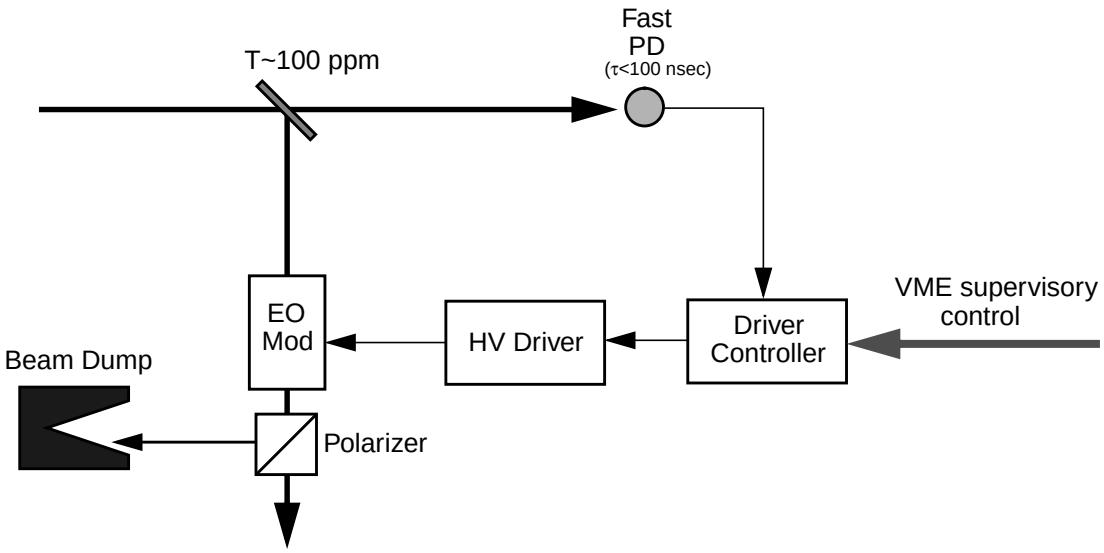

Figure 16: Schematic of the EO shutter, auxiliary optics, and drive electronics.

directed to a (modestly) fast photodetector, the output of which is used to trigger the shutter. The main beam travels through the EO modulator and a polarizer (the input beam is polarized, so an input polarizer is not needed). When the shutter is fully open the polarization is such that the beam is passed by the polarizer, and when fully closed the beam is ejected by the polarizer to a beam dump.

The EO modulator is a model 3904 Q-switch from Fast Pulse Technology, LaserMetrics Div., having the following properties (at 1064 nm):

- Material: lithium niobate, operated in transverse field mode
- Aperture: 8 mm diameter
- Capacitance: < 25 pF
- Transmission: 98% with windows (meas'd); >99% w/o windows (spec)
- Half-wave voltage: 3.4 kV (meas'd)
- Extinction: 500:1 (meas'd); >100:1 (spec)

The main reason for selecting this modulator was its large diameter.

To maximize optical transmission and eliminate any back-reflections, the output polarizer for the shutter will be a Brewster angle calcite polarizer (manf'd by K Lambrecht). The trigger photodetector is a Thorlabs model PDA255 (50 MHz BW), or equivalent.

A block diagram of the shutter controls is depicted in Figure 17. The commercial DEI pulse generator is basically a fast HV switch, design to drive capacitive loads; the rise/fall time spec of <45 nsec is much shorter than we actually need. The driver controller supplies HV to the pulse

LIGO-DRAFT

generator, and produces the gate that switches the DEI unit. The supervisory control will be used to control the following features:

- Closed shutter transmission level: the optical transmission when the shutter is in its ‘closed’ state will be variable from zero (minimum) to ~10%.
- Open shutter transmission level: the optical transmission when the shutter is in its ‘open’ state will be variable from 100% (minimum) to ~50%.
- Trigger level: the photodetector output level which triggers the gate can be controlled
- Automatic open: the controller will be able to automatically open the shutter when the photodetector transitions in the appropriate way – for example upon lock of the interferometer; this automatic open feature can be enabled or disabled (so that a manual open is require).

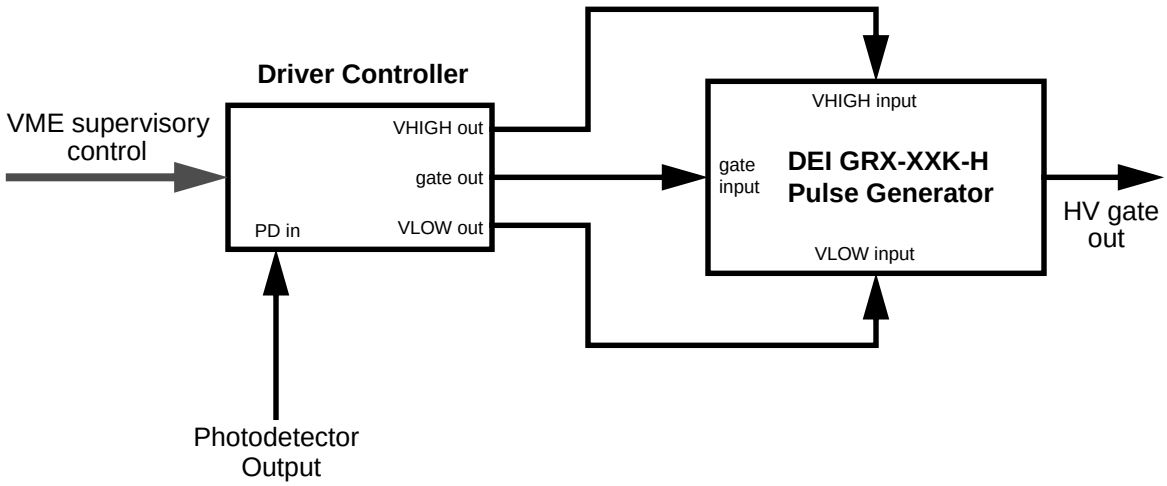

Figure 17: Block diagram of shutter control electronics.

The shutters are implemented at the mode cleaner reflected port, the interferometer reflected port, and the anti-symmetric port, as indicated in Section 2.1.1.3. Initial testing of the E-O modulator with the DEI driver has raised the following issues:

- while the HV switches very quickly, some optical switch ‘bounce’ is seen: the optical power rings down with spikes repeating every ~1 μsec, lasting ~10 μsec; this is probably due to a resonance(s) in the EO crystal. We will attempt to slow down the HV pulse, to a fall time of ~1 μsec, to avoid these ‘bounces.’
- the half-wave voltage of 3.4 kV is roughly 20% higher than the manufacturer’s spec; we have traced this to the fact that the electro-optic coefficient of $LiNbO_3$ is ~20% lower at 1064 nm than at 633 nm, the wavelength at which the manufacturer tests the crystals. At worst, this means we need to use a DEI driver with a higher rating (6kV vs 3kV).

LIGO-DRAFT

The optical quality appears to be adequate based on the 500:1 extinction (corresponds to ~λ/140 distortion). Further testing will be done to measure the transmission of the EO cell without windows (easily removable), and to eliminate the 'bounce' problem.

2.1.4. Quantum Efficiency Budget

We have estimated the optical losses expected in the ISC optics chain leading to the dark-port photodiodes. Combining these individual component transmission estimates with the measured quantum efficiency of the bare diode gives us an estimated net quantum efficiency slightly shy of the requirement (Table 6). It should be noted here that the diode quantum efficiency is only known to a precision of ±3% (certified accuracy of our optical power meter), and optical coating specifications are also typically somewhat uncertain (most often optimistic). As relay and protection components are procured and evaluated, we will attempt to optimize transmission by selection during the fabrication process. However at this time it is not feasible to guarantee 80% net quantum efficiency without severely compromising other required functions. It should again be emphasized that losses in COS relay and beam reduction optics are not included here, and will probably be comparable in magnitude.

item	*est. loss (dB)*	*comments*
periscope	–.01	REO hi-R
relay mirrors	–.01	REO hi-R
lenses	–.02	REO AR V-coat
EO shutter Xtal	–.044	LaserMetrics, no windows
polarizer	–.022	Lambrecht Brewster-cut
ASC WFS pickoff	–.044	1% total for WFS, QPD & video
beamsplitter chain	–.05	REO 50% T / AR V-coat
photodiode	–.81	83% ± 3% measured
TOTAL	–1.01	= 79.3%

Table 6: Quantum efficiency budget for the AS port beam.

2.2. RF Modulation & Demodulation

2.2.1. Phase Modulator Requirements

The electro-optic modulator will be a New Focus resonant phase modulator, model 4001 ($MgO:LiNbO_3$) or 4003 ($LiNbO_3$). The modulation sensitivity for these devices is specified to be 0.1–0.3 rad/V (into 50 ohm). The nominal modulation depth for optimal shot-noise sensitivity is $\Gamma \approx 0.5$, and we require that the modulator driver can attain a depth of at least $\Gamma \approx 0.7$. Thus in the worst case (assuming a sensitivity of 0.1 rad/V), the RF power required is

LIGO-DRAFT

$P_{max} = (5\ V_{rms})^2/50\Omega = 0.5\ W = 27\ dBm$. More typically, the drive level to the modulator will be 65 mW (18 dBm). We require that the modulation level can be controlled in steps no coarser than 0.01 radian.

2.2.2. LO Distribution

Figure 18 shows the distribution scheme for the main modulation frequency LO & RF signals (for 4km interferometer). The RF source is located in rack 1X8 or 1X9, and is split between the modulator driver input and the LSC & ASC demodulation LO distribution modules.

2.2.3. Modulation Source

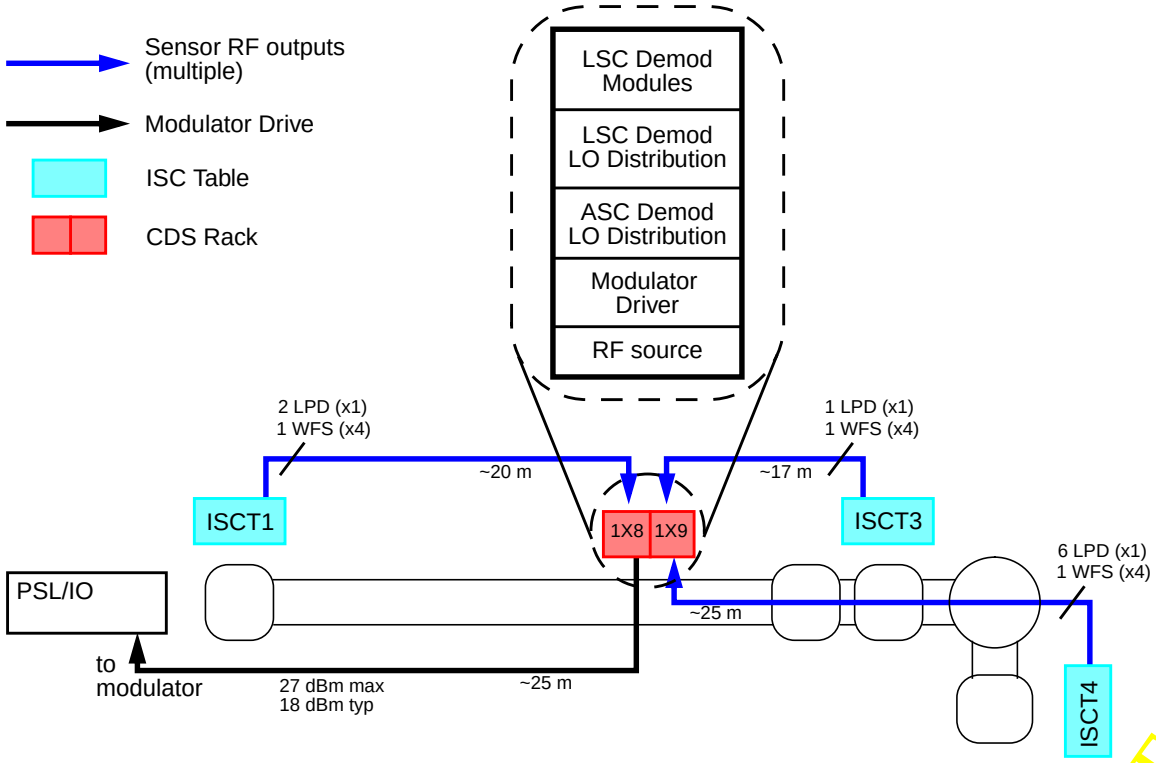

Figure 18: Distribution scheme for the main modulation frequency LO & RF signals. All detector RF signals are brought to racks 1X8 & 1X9 as shown. The routing paths are only schematic; the cables will be routed along established cable paths. The lengths are approximate total cable lengths from connector-connector for the indicated signal(s). The wire counts indicate that there are 4 RF cables per WFS head, and one per length photodetector (LPD).

The modulation source will be a commercial RF signal generator. At least for the initial setup, we require the tunability of a signal generator to obtain the frequency that is matched to the mode cleaner free-spectral-range. In addition, the phase- and amplitude-modulation capabilities of such a source are convenient for diagnostic tests. The disadvantage of a signal generator is larger phase noise compared to a crystal oscillator made at the required frequency. However we have determined that commercial signal generators with adequate phase noise performance are available

LIGO-DRAFT

(see next section). If improved phase noise performance is eventually required, a crystal oscillator can be made at the determined frequency.

2.2.3.1 Phase Noise

We measured the phase noise of several RF signal generators as part of selecting a modulation source. This was done by mixing the signal generator under test with a crystal oscillator, f = 25.23 MHz; a slow feedback to the generator was used to keep the two oscillators phase locked. The spectrum of the IF output of the mixer was measured and ascribed to the generator under test; the IF was calibrated using the peak-to-peak swing of the IF when the two oscillators were not locked. The results of measurements on several generators are shown in Figure 19. As a result, we have chosen the Marconi 2023 signal generator, a relatively low-cost unit (~$7k). Some relevant features of this generator are:

- Frequency Range: 9kHz – 1.2 GHz
- Frequency Resolution: 1 Hz
- Supplied with the OCXO (oven-controlled-crystal-oscillator) option
- Amplitude & Phase modulation capability: external or internal (one or two tones up to 20 kHz)
- RS232 and GPIB control

LIGO-DRAFT

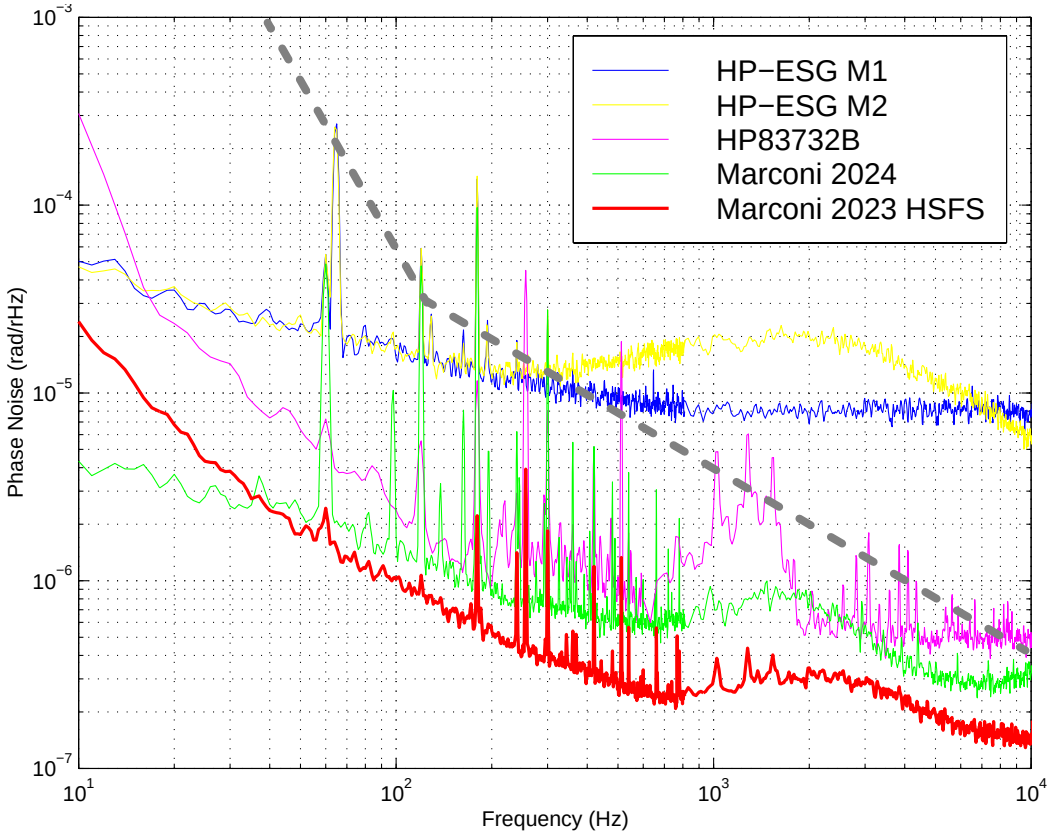

Figure 19: Phase noise vs. offset from carrier frequency for several commercial RF signal generators; the carrier frequency is ~25 MHz. The phase noise requirement is given by the dashed line (and is a factor of 2 below the requirement given in the LSC DRD).

2.2.3.2 Modulation Driver – Amplitude Noise & Control

The amplitude noise requirement on the oscillator (relative fluctuation of $\leq 5\times10^{-8}$ at $f > 200$ Hz offset from carrier; detailed in the LSC DRD) is relevant only for the drive on the phase modulator. We also measured the free-running amplitude noise of the signal generators noted in the previous section; all showed amplitude noise above our requirement. To meet the AM requirement, we measure the amplitude of the modulator drive using a diode detector and use a feedback loop to

LIGO-DRAFT

suppress it. This technique has been tested, using one diode detector for the stabilization, and another outside of the loop to measure the residual amplitude noise, as shown in Figure 20.

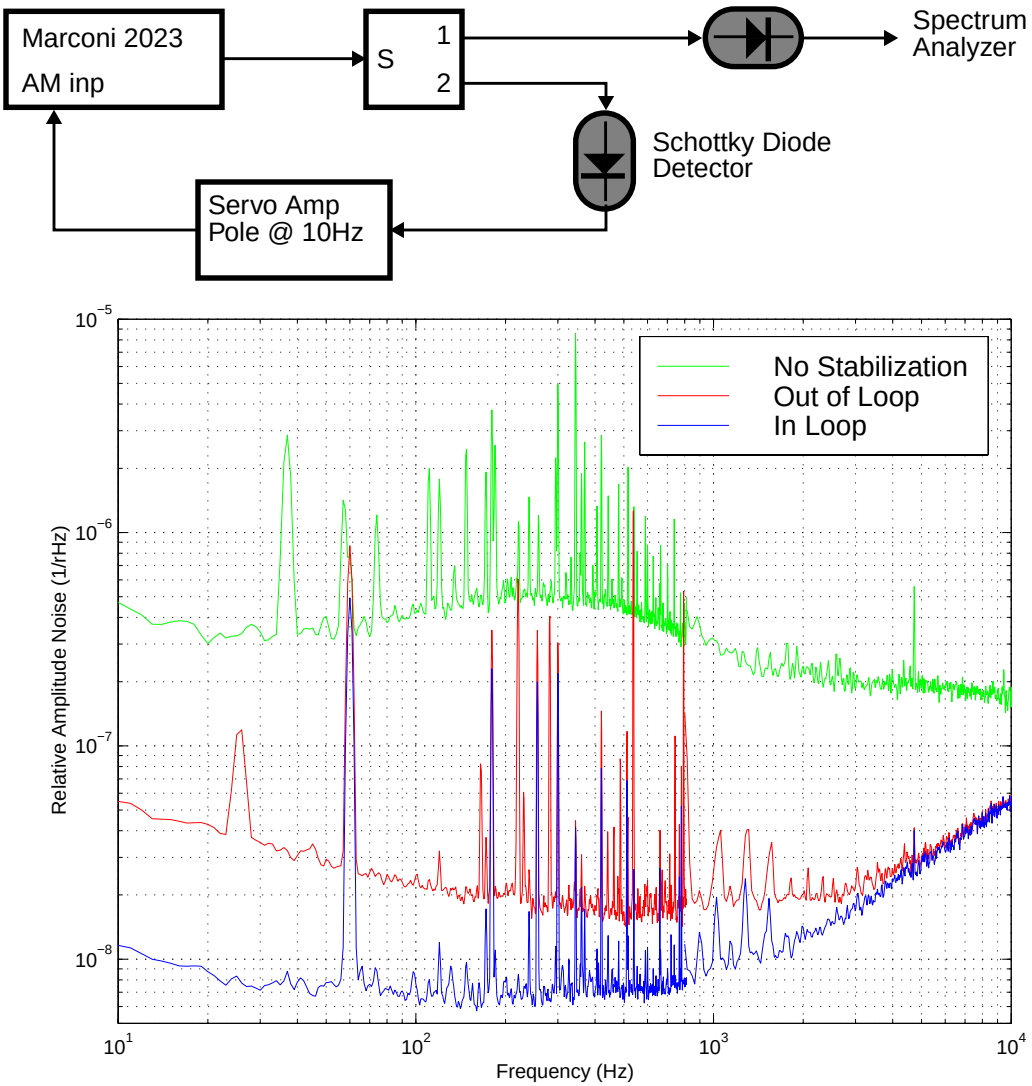

Figure 20: Setup for stabilizing and measuring the amplitude noise of the RF signal generator. The servo bandwidth is approximately 10 kHz. The plot shows the amplitude noise, as measured by the out-of-loop detector, before stabilization (top) and after stabilization (middle); the bottom curve is the spectrum of the in-loop detector. The amplitude noise requirement is given by the dashed line.

The modulator driver, shown in Figure 21, will consist of a ~1W amplifier followed by a level detector (directional coupler/power splitter + diode detector); this arrangement is used to obtain a good measurement of the drive applied to the modulator (the detector may be located at the modulator end of the driving cable). The feedback control signal may be applied to an electronic attenuator prior to the amplifier (as shown), with a DC offset input on the servo amplifier used to control the modulation level. Alternatively, the external AM input on the signal generator may be used for stabilization. Which method is used will be determined as part of the LSC CDS final design.

LIGO DRAFT

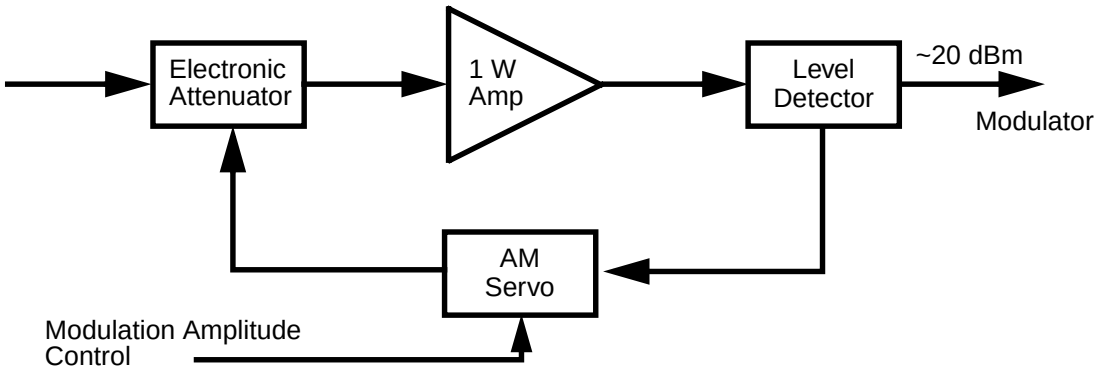

Figure 21: Block diagram of the modulator driver. A servo loop is used to stabilize the amplitude of the drive voltage to the required level. The Level Detector consists of a directional coupler and a diode detector, and may be located right at the modulator if noise pick-up in the drive cable is an issue.

2.2.4. Demodulation

The system for demodulating the RF outputs of the photodetectors will include the following features:

- the signal at each port will be demodulated in both RF phases (each photodetector RF output will be split in two, and demodulated with I & Q LO phases)
- in order to match the linear range of the photodetector amplifier (~3 V_{pk}) to the mixer range (after 50Ω loading and splitting), the mixer should allow for at least 13dBm of RF power in linear range (e.g., a level 17 double balanced diode bridge mixer that allows 14 dBm of RF would be sufficient)
- the common LO demodulation phase for each photodetector will be adjustable in increments of 0.5° or finer, and over a range of at least 180°; the I & Q demodulation phases will be orthogonal to within 0.5°.

LIGO-DRAFT

3 LOCK ACQUISITION

Please see LIGO-T980069-00-D, Lock Acquisition Final Design, which is supplied as a separate document. We apologize for the inconvenience.

LIGO-DRAFT

4 DETECTION MODE CONTROLS

In this section we present a design for control of the interferometer lengths and the laser frequency. The Matlab/Simulink models used in the development of this design incorporate "realistic" noise inputs — the ground noise spectrum was measured at the sites while the shot noise is calculated from the interferometer parameters and the thermal noise due to pendulum and violin modes is simulated based on suspension parameters. The suspended mirrors are modeled as simple pendula with their suspension points attached rigidly to the top of seismic isolation stacks. Ground noise is propagated through the stacks, which act as a sharp filter at frequencies above about 5 Hz. A Simulink model [1] is used to infer stack transmissibilities along five axes. The motions of the mirror suspension points are correlated to each other with the same correlation model used in the SLAC study [2]. The optical plant is calculated using the results of recent FFT simulations which include [13]

- "pseudo-Calflat" surface maps for the mirror substrates: these are the original Calflat phase maps scaled to give $\lambda/600$ rms;
- mirror coating maps inferred from the pathfinder coated optic[1];
- thermal lenses on the BS, ITMs and ETMs and a recycling mirror curvature of 12.95 km to compensate the thermal lensing.

The photodetection scheme is described in the previous sections and the test masses actuation includes recent changes in the suspension controller design.

4.1. Design Considerations

4.1.1. Residual Deviations

The residual deviations in the controlled degrees of freedom set the servo gain requirements. Table 7 summarizes the allowed rms deviations which are given in [4]. The largest mechanical

Degree of freedom	*Residual deviation*	*Units*	*Coupling mechanism*
$\delta Lm + (\pi/(2F))\delta lm$	1×10^{-13}	m_{rms}	Amplitude noise coupling
$\delta lm + (\pi/(2F))\delta Lm$	1×10^{-9}	m_{rms}	Amplitude noise coupling
$\delta(k_l \cdot Lp)$	9×10^{-6}	rad_{rms}	Arm cavity power reduction
$\delta(k_l \cdot lp)$	7×10^{-4}	rad_{rms}	Arm cavity power reduction

Table 7: Allowed residual deviations for each of the degrees of freedom controlled.

1. This coating had a six-fold symmetry (spokes at 60°) which is thought to be caused by the motion of the planetary in the coating chamber. It was not present in subsequent coatings. We mention this here because this six-fold symmetry gave an unusually high (factor of 6) contrast defect when the coating maps were rotated for some optics in the FFT simulation.

LIGO-DRAFT

excitations occur at low frequencies, typically 2 μm_{rms} at the micro-seismic peak (0.16 Hz) and about 0.1 μm_{rms} at the stack resonances (2 to 5 Hz). The gain at these frequencies must be high enough to suppress ground noise excitations to the required levels, as much as 140 dB at the micro-seismic peak for the *Lm* degree of freedom.

4.1.2. Frequency Stability

The requirement on the gravitational-wave-band frequency fluctuations of the light incident on the interferometer is shown in Figure 22(a) (lower curve). This level of frequency noise would produce a noise level in the gravitational wave readout that is 10% in amplitude of the noise corresponding to the initial LIGO SRD sensitivity [5], in the presence of a difference in the arm cavity resonant-reflectivities of 0.5% (corresponding to a round-trip loss difference of 75 ppm). Dividing this frequency noise by the level of frequency noise expected from the IOO subsystem (upper curve in Figure 22(a)) leads to the minimum gain required in the LSC frequency servo to achieve adequate frequency stability (Figure 22(b)).

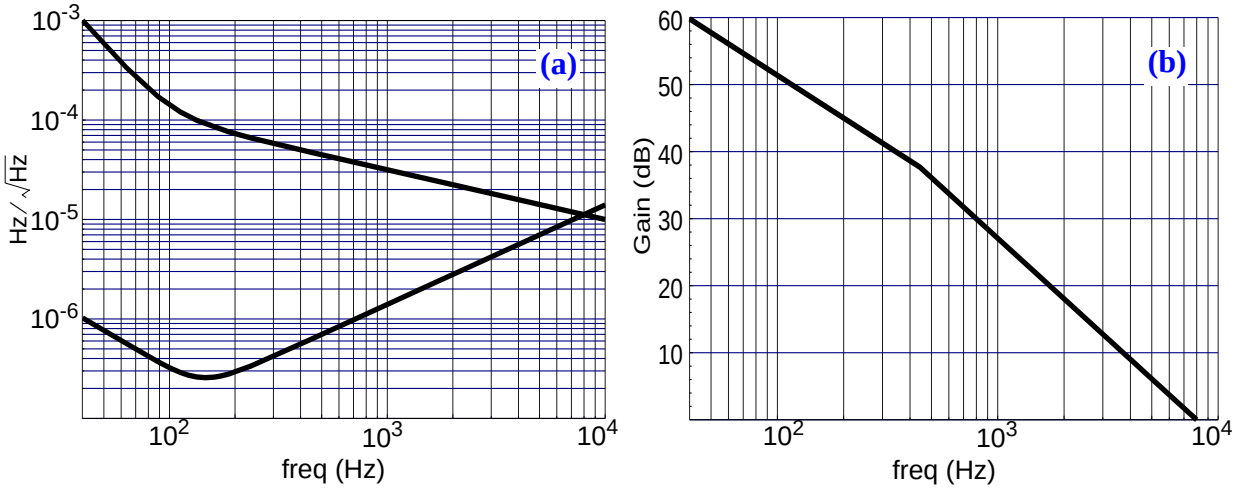

Figure 22: (a) Frequency fluctuation requirements for the IOO (top curve) and interferometer (bottom curve) subsystems. The frequency noise requirement on the light incident on the recycling mirror is derived assuming a 0.5% difference in the resonant-reflectivities of the two arm cavities. (b) Minimum frequency suppression factor (in dB) of the interferometer needed to suppress the mode cleaner frequency noise to the required LSC level

4.1.3. Suspension Vertical Mode

We consider two mechanisms by which excitation of the vertical motion can couple to longitudinal displacement: curvature of the earth's surface along the 4 km baseline gives rise to a 3×10^{-4} coupling coefficient; and the core optics COC wedged surfaces (along the vertical axis) give rise to a 2×10^{-2} vertical-to-horizontal coupling coefficient. This is particularly important for the vertical or "bounce" mode of the suspension at 13 Hz (19 Hz for the beamsplitter). The optical path displacement due to the bounce mode of an optic can be estimated by:

LIGO-DRAFT

$$s_V = \xi \cdot \tilde{z}_g(f_V) \cdot T_{zz} \cdot \sqrt{Q_V \cdot f_V} \quad (1)$$

where ξ is the vertical-to-horizontal coupling coefficient, $\tilde{z}_g(f_V)$ is the spectral density of the ground noise at the vertical mode frequency, f_V; T_{zz} is the vertical-to-vertical stack transmissibility at f_V; and Q_v is the quality factor of the resonance. The coupling coefficient ξ is given in general by $\xi = (n-1)\alpha + \beta$, where n is the refractive index of the optic, α is the wedge angle of the optic, and β is the angle of the reflecting surface from the local vertical (for a beam not passing through a substrate, take $\alpha = 0$); the angles α and β are given in [6]. Assuming $\tilde{z}_g(13\text{ Hz}) = 10^{-9}\text{ m}/\sqrt{\text{Hz}}$, $Q_V = 2000$ and $T_{zz} \approx 0.5$, the length fluctuations due to the vertical resonance for each d.o.f. are given in Table 8.

Degree of freedom	*Length displacement (m_{rms})*	*Coupling coefficient (ξ)*	*Coupling due to*
Lm	6×10^{-11} a	7×10^{-4}	Earth's curvature
lm	1×10^{-9} b	1×10^{-2}	20 mrad wedge angle (ITM)
Lp	6×10^{-11} a	7×10^{-4}	Earth's curvature
lp	2×10^{-9} c	1×10^{-2} 2×10^{-2}	20 mrad wedge angle (ITM), & 20 mrad surface angle (RM)

Table 8: Estimated mirror motion due to vertical resonance of the suspensions.

a. $\sqrt{4} \times S_V$ to account for uncorrelated motion of four test masses, each moving with S_V.

b. $\sqrt{2} \times S_V$ for uncorrelated motions of two ITMs. Contribution from the BS vertical mode at 19 Hz is negligible.

c. $\sqrt{(\sqrt{2} \times S_V^{ITM})^2 + (S_V^{RM})^2}$ for uncorrelated motions of two ITMs and RM.

The length fluctuations due to the vertical mode are relatively large, and can be difficult to stabilize because the vertical mode frequency is much closer to the unity gain frequencies of the servos than the micro-seismic peak and the stack modes, which are the other dominant sources of fluctuations. In the loop designs presented below, we have included resonant gain sections in all but the *Lp* (laser) loop, that provide a gain increase of 26 dB over a ~0.1 Hz bandwidth, centered at 13 Hz. Without this gain stage, the residual length deviations either exceed or are right at their requirements, and in all cases are dominated by fluctuation at 13 Hz

4.1.4. COC Internal Resonances

The internal resonances of the test masses occur at a few to tens of kilohertz and are, in principle, outside the bandwidth of the servos. However, any unintentional drive current at the internal resonance frequencies will be greatly amplified by the high *Q* of these resonances and can lead to servo instability. The displacement of the mirror surface in response to a force applied at the magnet positions — or transmissibility — for the first several modes was calculated using a finite element/I-DEAS model [7], [8] and the results for the modes most relevant to the length servo design are summarized in Table 9. The modal frequencies in the analysis are somewhat different

LIGO-DRAFT

from those measured in the Pathfinder optic [9]; this discrepancy can be ascribed partly to a difference in the wedge angle. For the LSC design, we use the measured frequencies.

	Mode description	*Resonant frequency (Hz)*	*Transmissibility (m/N)*[a]	*Maximum servo gain*[b]
Test Masses & RM	Non-axisymmetric, astigmatic mode	6595	2×10^{-10}	-6 dB
	First symmetric (drum head) mode[c]	9206 (calc.) 9476 (meas.)	2×10^{-4}	-131 dB
	Second symmetric mode	14475	3×10^{-6}	-103 dB
Beamsplitter	Non-axisymmetric, astigmatic mode	3785	3×10^{-8}	-30 dB
	Symmetric (drum head) mode	5578	1.6×10^{-3}	-133 dB
	Second symmetric mode	14630	9×10^{-7}	-85 dB

Table 9: Mirror internal mode transmissibilities.

a. Gaussian-weighted displacement per unit force applied at *each* of the four magnets. A quality factor of $Q = 1.3 \times 10^6$ is assumed for all modes.
b. Not including the resonant response factor; these gain limits are set so that the complete open loop servo gain does not exceed -10 dB at any resonance to ensure servo stability.
c. Note that the transmissibility for this mode is nearly equal to the displacement/force of a free point mass, multiplied by the Q: $(4Q)/(m\omega^2) = 1.5\times10^{-4}$ m/N .

The servo gain requirement given in the table is the maximum loop gain for any servo path incorporating the given optic, measured open loop but not including the resonant response factor. This is a convenient way of expressing the requirement because the servo models include only the response of a suspended point mass, and thus do not include the internal modes. The servo gain requirement follows from the transmissibility as follows:

$$G(\omega) \le \left(\frac{1}{2}\right) \cdot \frac{4}{M\omega^2 T(\omega)} \qquad (2)$$

where M = 10.7 kg, T is the transmissibility, and the (1/2) is the safety factor of ensure that the magnitude of the total open loop gain is less than one.

The required attenuation will be achieved with a combination of the low-pass anti-aliasing filters (between the demodulation and the ADC inputs) and bandstop filters centered at the drum-head modes. The fact that the frequency of the test mass drum head mode is above the Nyquist

LIGO-DRAFT

frequency (for a 16384 Hz sampling rate) does not help; the mode frequency is aliased down to 16384 – 9400 = 6984 Hz upon sampling, but at the DAC output this frequency is imaged back up to 9400 Hz so that a coherent feedback path at this frequency exists. The bandstop filters could be realized in the analog or digital domain:

- *Analog.* The bandstop filters would be located at the DAC outputs. This is preferred to putting them before the ADCs because there are much fewer DAC channels, and each output would need only one bandstop filter (with center frequency appropriate to the mass being driven). A filter design that looks promising is an 8th-order elliptic, with a stopband attenuation of 80 dB and a width of 1 kHz. This is the filter implemented in the Matlab servo models.
- *Digital.* If processing time allows for it, implementing these filters digitally may be preferred (the 8th-order elliptic would require 8 second order sections, e.g.).

4.1.5. Seismic excitation model

The seismic excitation model used for the LSC design is similar to the model developed for the ASC system [10] and is summarized in Appendix 1. In Table 10 we state the resulting estimates for motion of the mirror suspension points.

Degree of freedom	*root-mean-square*	*peak-to-peak*	*ratio*
Horizontal east-west ground trace	1.9 µm	12.4 µm	6.5
At RM pendulum suspension point	2.0 µm	12.8 µm	6.4
At *Lm* pendulum suspension point	3.0 µm	19.0 µm	6.3
At *Lp* pendulum suspension point	3.3 µm	20.0 µm	6.0
At *lm* pendulum suspension point	9 nm	63.0 nm	7.0
At *lp* pendulum suspension point	20 nm	163 nm	8.1

Table 10: The rms and peak-peak excursions in the models used for suspensions point excitation.

4.1.6. Shot noise

As shown in Figure 50, shot noise is added to each sensor as a voltage noise density prior to the controller matrices. These noise levels are derived from the FFT simulation of the interferometer: the simulation provides us with the optical power at each port (decomposed into carrier and sidebands); the power levels determine the shot noise current, and the transimpedance gain of the

LIGO-DRAFT

photodetector-demodulation set the voltage noise [11]. The shot noise levels used in the modeling are shown in Table 11.

Port/Sensor	*Power (Carrier + SB = Total)*	*Shot noise current A/√Hz*	*Equivalent Length Noise (DC)*
Antisymmetric/S_{AQ}	0.30 + 0.86 = 1.16 W	4.19×10^{-10}	$\delta\tilde{L}_m = 4.3\times10^{-20}$ m/$\sqrt{\text{Hz}}$
RC pickoff/S_{PI}	65 + 6 = 71 mW	9.05×10^{-11}	$\delta\tilde{l}_p = 5.6\times10^{-17}$ m/$\sqrt{\text{Hz}}$
RC pickoff/S_{PQ}		8.67×10^{-11}	$\delta\tilde{l}_m = 1.7\times10^{-16}$ m/$\sqrt{\text{Hz}}$
Reflected/S_{RI}	0.13 + 0.16 = 0.29 W	2.04×10^{-10}	$\delta\tilde{L}_p = 9.1\times10^{-21}$ m/$\sqrt{\text{Hz}}$
Reflected/S_{RQ}		1.53×10^{-10}	$\delta\tilde{l}_m = 2.1\times10^{-17}$ m/$\sqrt{\text{Hz}}$

Table 11: Power levels and shot noise photocurrents at the interferometer ports. Also given is the equivalent DC length sensitivity for the length degree-of-freedom controlled by each sensor.

4.1.7. Delays & Phase Margins

The servo loops are designed with the goal that the phase margin should be at least 50°. This keeps the loop amplification around unity gain frequencies low; the peak amplification is $M = (2\sin(PM/2))^{-1} = 1.18$ for a phase margin of $PM = 50°$.

The MATLAB models of the servo systems do not include time delays due to propagation delays and latencies in the signal processing. The effect of delays will be most severe on the L_m (GW) loop, since it has the largest bandwidth of the digital loops and actuates on the end test masses.

LIGO-DRAFT

We estimate the delays in the system, as shown in Table 12, and require that the 50° phase margin hold in the presence of the time delay phase lags.

Source of delay	*Delay*	*Loops affected*	
		L_m	l_m, l_p
Propagation up & down arms	2 x 13 μs	✓	
Sampling: half the sampling period	30 μs	✓	✓
Processing: ~ sampling period	60 μs	✓	✓
DAC delay: 1.5 x output period	11 μs	✓	✓
Total delay		127 μs	101 μs
Unity-gain frequency		330 Hz	43, 130 Hz
Phase lag at u.g.f.		15°	1.6°, 5°

Table 12: System delays.

4.1.8. Actuator dynamic range

The interferometer lengths are actuated via the LSC inputs on the suspension controllers, which have range of ±20 μm peak-to-peak for frequencies below 0.7 Hz. Since there are two suspensions associated with each length degree of freedom, the total range of the suspension actuators at low frequencies is 40 μm. The frequency correction signals are fed back to both the mode cleaner length and to an additive input which offsets the mode cleaner frequency error signal. The wideband actuator (voltage-controlled oscillator) in the pre-stabilized laser system must, in turn, follow the mode cleaner frequency. The SOS suspension controller for the mode cleaner length actuation has a ±27 μm peak-to-peak range which corresponds to 640 MHz but the full range is not useful for frequency actuation since the VCO is expected to have a ±5 MHz range. The additive offset input at the mode cleaner error signal has a dynamic range of less than 100 Hz.

4.1.9. Electronics Noise

The LSC electronics noise in the GW (readout) channel must be at least 10× smaller than the signal level determined by the SRD sensitivity curve, throughout the band of 40 – 7000 Hz. There are three significant sources of electronics noise in this channel: photodetector front end noise; ADC input voltage noise; DAC output voltage noise. Their relative importance depends on the frequency – the DAC noise is most significant from 40–100 Hz, and the ADC and photodetector noise are most significant above 100 Hz. As a rough guide, the amplitude spectral density of each noise source must be at least 15× lower than the SRD curve at the frequency where that noise source is most significant.

LIGO-DRAFT

4.2. Differential Modes

4.2.1. Servo Design

A block diagram of the differential-mode servo is shown in Figure 51 in Appendix 2. The servo model includes coupling of input noise to both sensors via off-diagonal plant elements. The control system shown in this figure was implemented in a Matlab® model to develop and test the servo design. A detailed representation of the L_m servo blocks is shown in Figure 23. The plant block, *PLm*, comprises the optical plant pole at 91 Hz, the DC plant response (in A/m, assuming 0.7 A/W photodiode responsivity), and the photodetector-demodulation gain in volts/amp. The controller block, *CLm*, consists of a low pass/anti-aliasing filter, a bunch of gain, some real zeros and poles for the servo compensation, a deep (80dB) stopband filter to achieve sufficient attenuation at the test mass resonance and a resonant gain stage tuned to the suspension vertical mode frequency at 13 Hz. The transfer function for the resonant gain stage is given by

$$T(s) = 1 + C\frac{2\pi f_r s}{s^2 + \frac{2\pi f_r}{Q}s + (2\pi f_r)^2} \tag{3}$$

where f_r is the resonant frequency, Q is the quality factor and C is a constant offset. The pendulum block is made up of the suspension controller transfer function (1 Hz/40 Hz pole/zero pair), the DC coil driver sensitivity in volts per meter and the pendulum transfer function with resonant frequency at 0.74 Hz. Similarly, the servo blocks for the *lm* controls are shown in Figure 24.

An important feature of the differential-mode control system is the need for a non-zero off-diagonal element in the control matrix, $\hat{C}$, of Figure 50 to reduce coupling of shot noise in the detection of *lm* from coupling to *Lm* via the non-diagonal element of the optical plant matrix, P_{lm2AQ}. This is discussed in Appendix 2.

LIGO-DRAFT

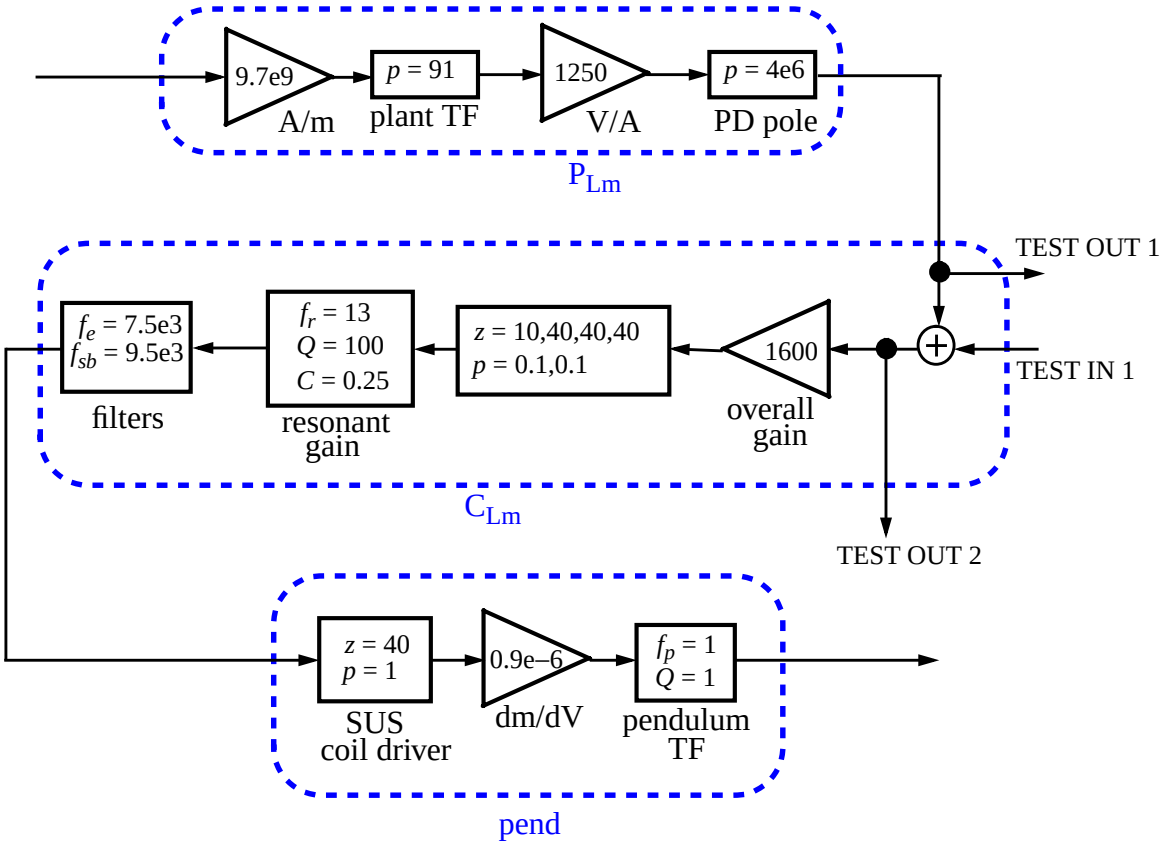

Figure 23: Control system blocks for the *Lm* loop. *z* refers to frequencies of zeros; *p* to pole frequencies; G to gain; f_p is the pendulum resonant frequency; f_r is the frequency of a resonant gain stage to suppress noise due to the vertical mode coupling (see eqn. (3)); the "filters" block contains a 6th order, 60 dB elliptic filter with cutoff frequency f_e for anti-aliasing and an elliptic stopband filter at f_{sb} which together give an attenuation of −135 dB at 9.48 kHz (the test mass internal resonance). All frequencies are in Hz and gains are dimensionless, unless otherwise specified.

LIGO-DRAFT

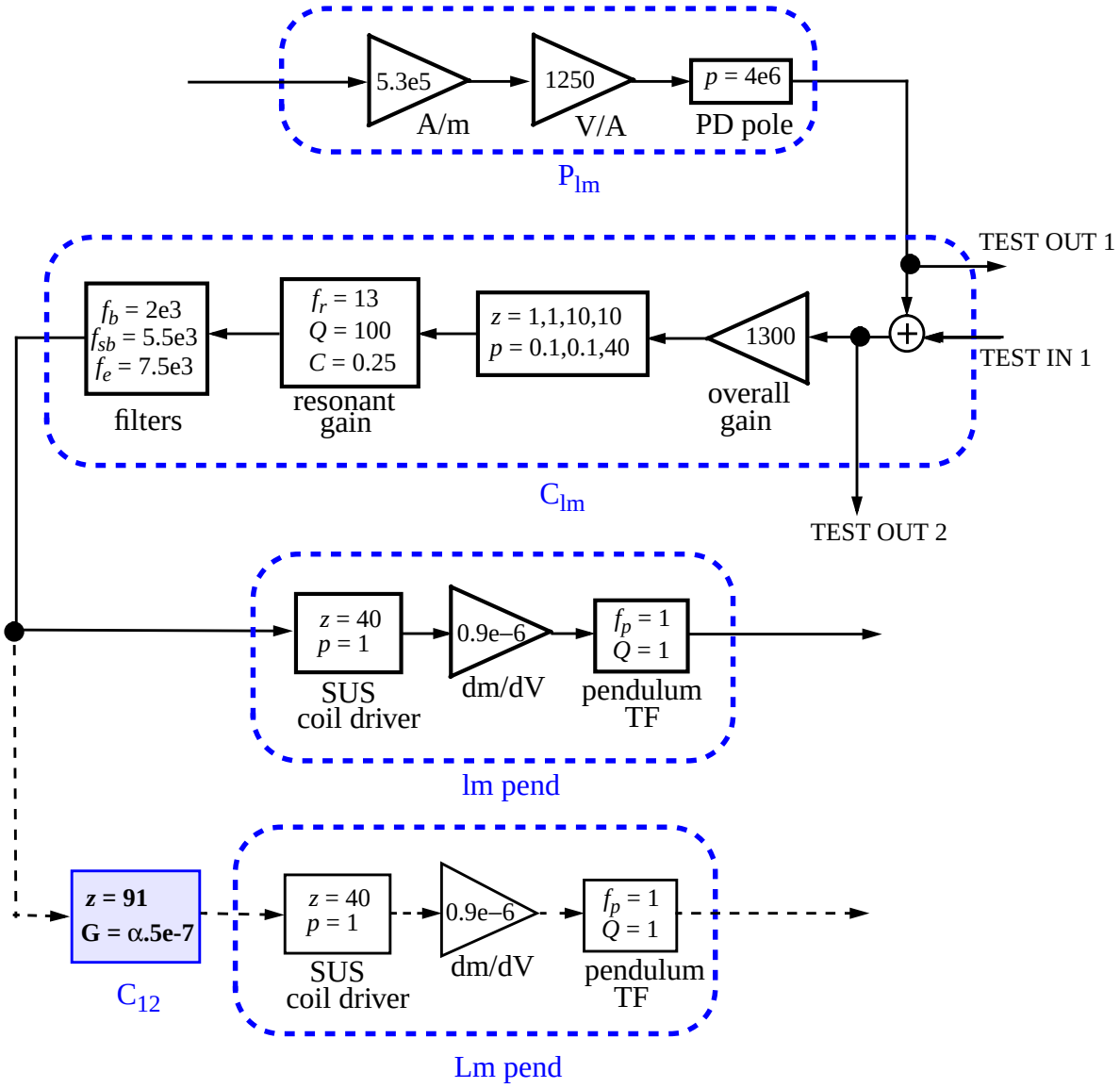

Figure 24: Control system blocks for the *lm* loop. *z* refers to zero frequencies; *p* to pole frequencies; G to gain; f_p is the pendulum resonant frequency; f_r is the frequency of a resonant gain stage to suppress noise due to the vertical mode coupling (see eqn. (3)); the "filters" block contains a 2-pole Butterworth filter at f_b and an elliptic stopband filter at f_{sb} which together give an attenuation of −130 dB at 5.58 kHz (the beamsplitter internal resonance), and a 6th order, 60 dB elliptic filter with cutoff frequency f_e for anti-aliasing. The shaded block, C_{12}, is the off-diagonal control path to reduce coupling of shot noise at the pick-off port to the gravitational wave signal. All frequencies are in Hz and gains are dimensionless, unless otherwise specified.

LIGO-DRAFT

4.2.2. Control System Performance

In this section we present the performance of the control system vis-a-vis the requirements using the controllers of Figures 23 and 24. Figure 25 and Figure 26 show the open loop gain for the L_m

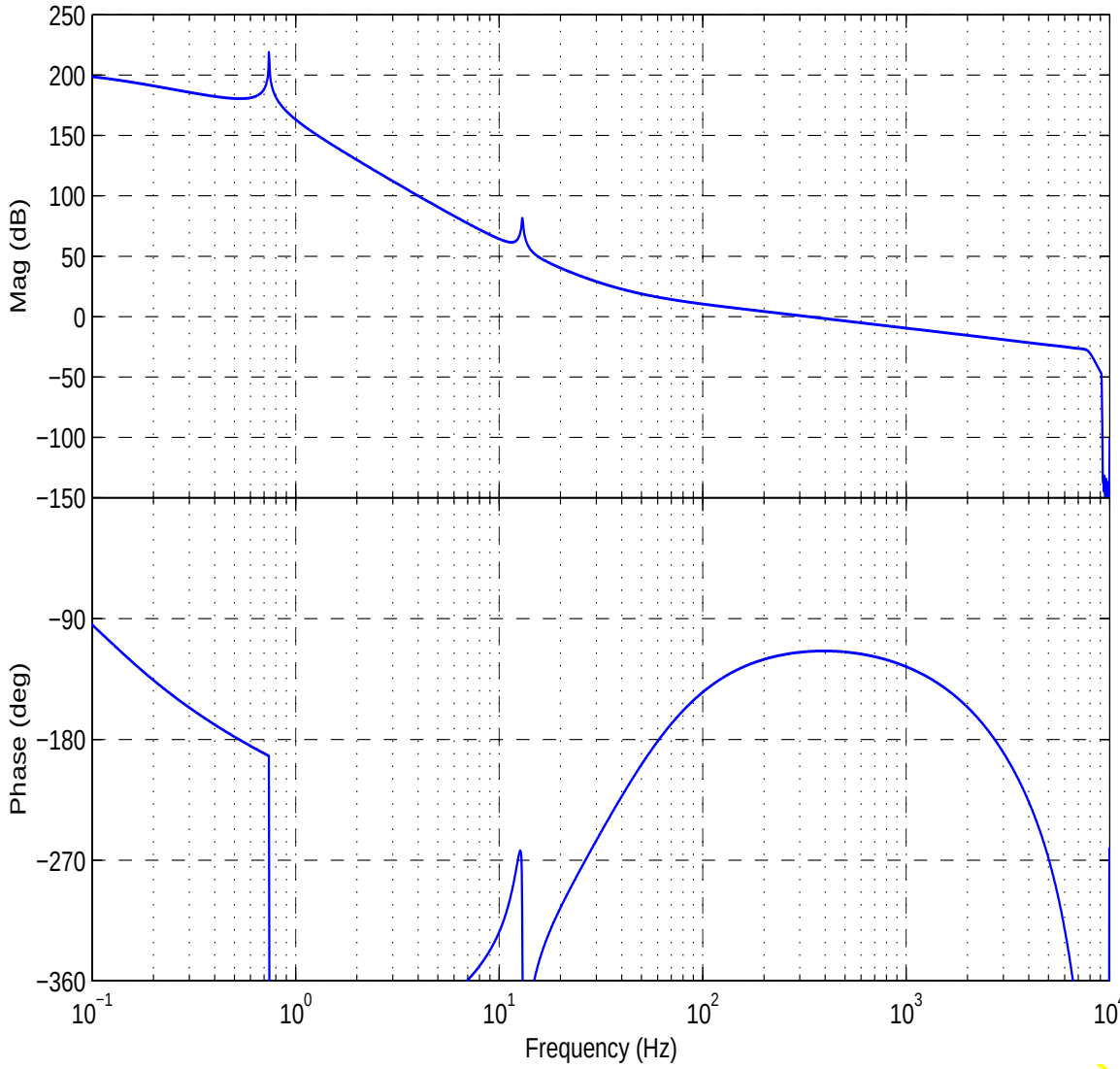

Figure 25: Open loop gain for the L_m servo. Loop parameters are given in Table 13.

and l_m servos, respectively. A summary of the loop performance data for differential degrees of freedom is given in Table 13. The residual length deviations from resonance are shown in Figure 27, and in Figure 28 we show the contributions from the differential sensing and control system to the interferometer strain sensitivity.

LIGO-DRAFT

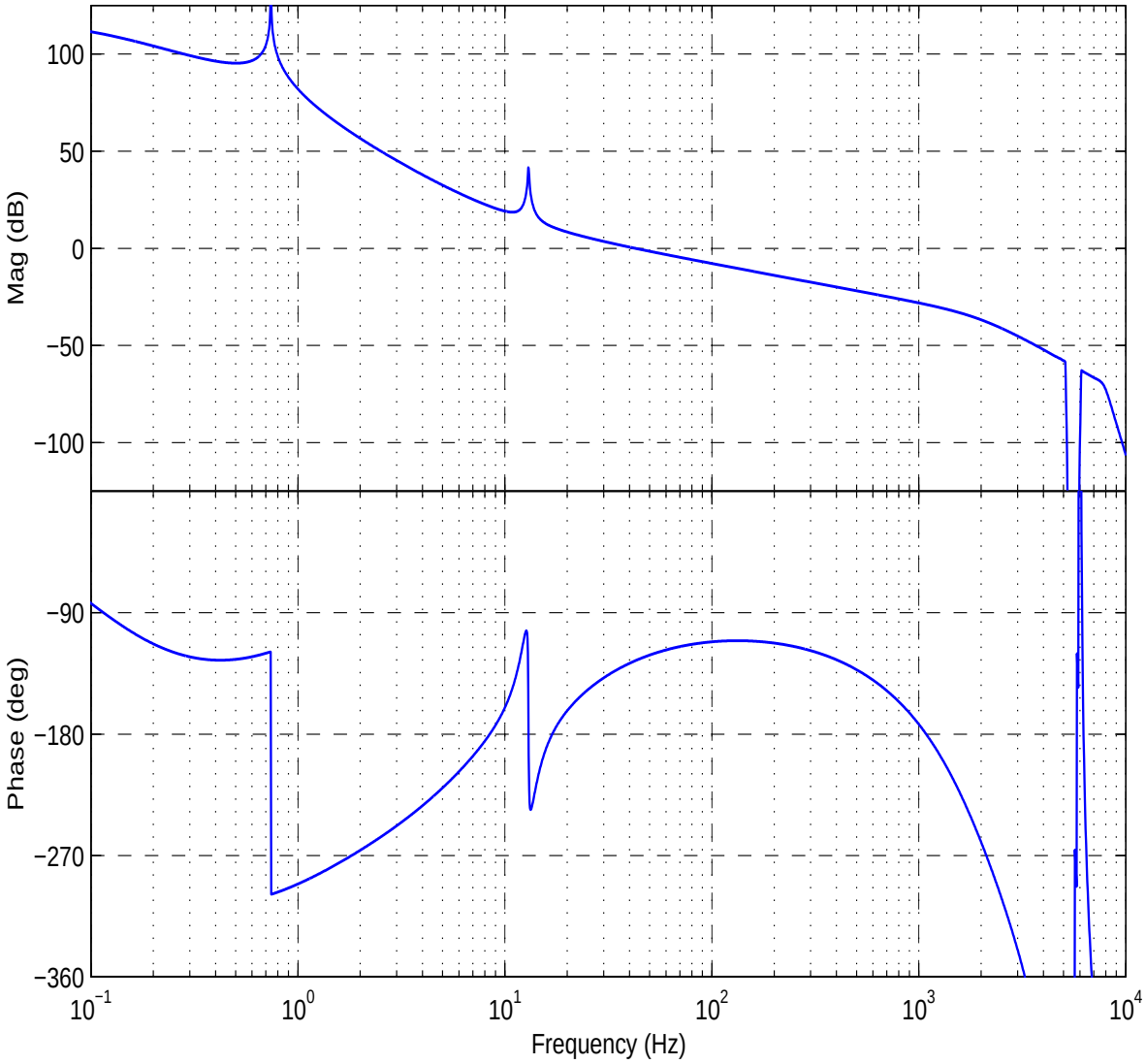

Figure 26: Open loop gain for the *lm* servo.

LIGO-DRAFT

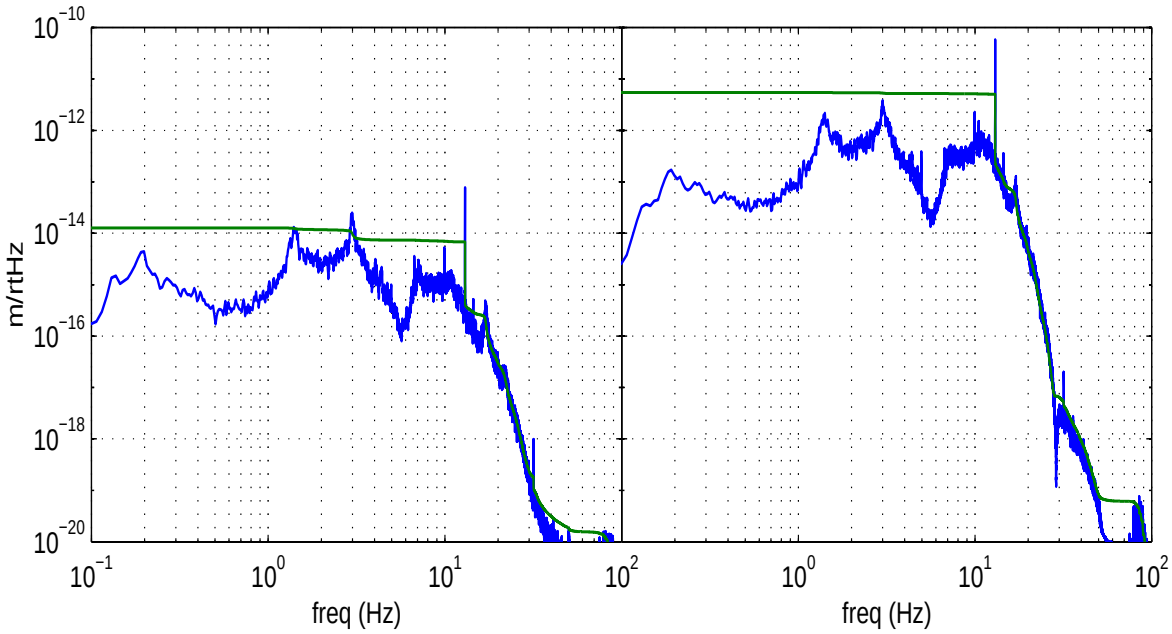

Figure 27: Residual length deviations for L_m (left) and l_m (right), shown as an amplitude spectral density and an integrated rms vs. frequency (vertical scales apply to both types of curve). The rms residual L_m deviation is 10^{-14} m, and is dominated by motion at the first two stack resonances. The rms residual l_m deviation is about 10^{-11} m, and is dominated by motion at the 13 Hz vertical mode of the ITMs.

Performance Data	***Lm***	***lm***	***Units***
Gain at DC	205	110	dB
Unity gain bandwidth	330	43	Hz
Phase margin	66	55	degrees
Gain at 9.48 kHz (5.58 kHz)	–140	(–141)	dB
Residual length deviation	10^{-14}	5×10^{-12}	m_{rms}
Control signal at coil driver	3.1	0.13	μm_{rms}

Table 13: Control system characteristics and performance data for the differential degrees of freedom.

LIGO-DRAFT

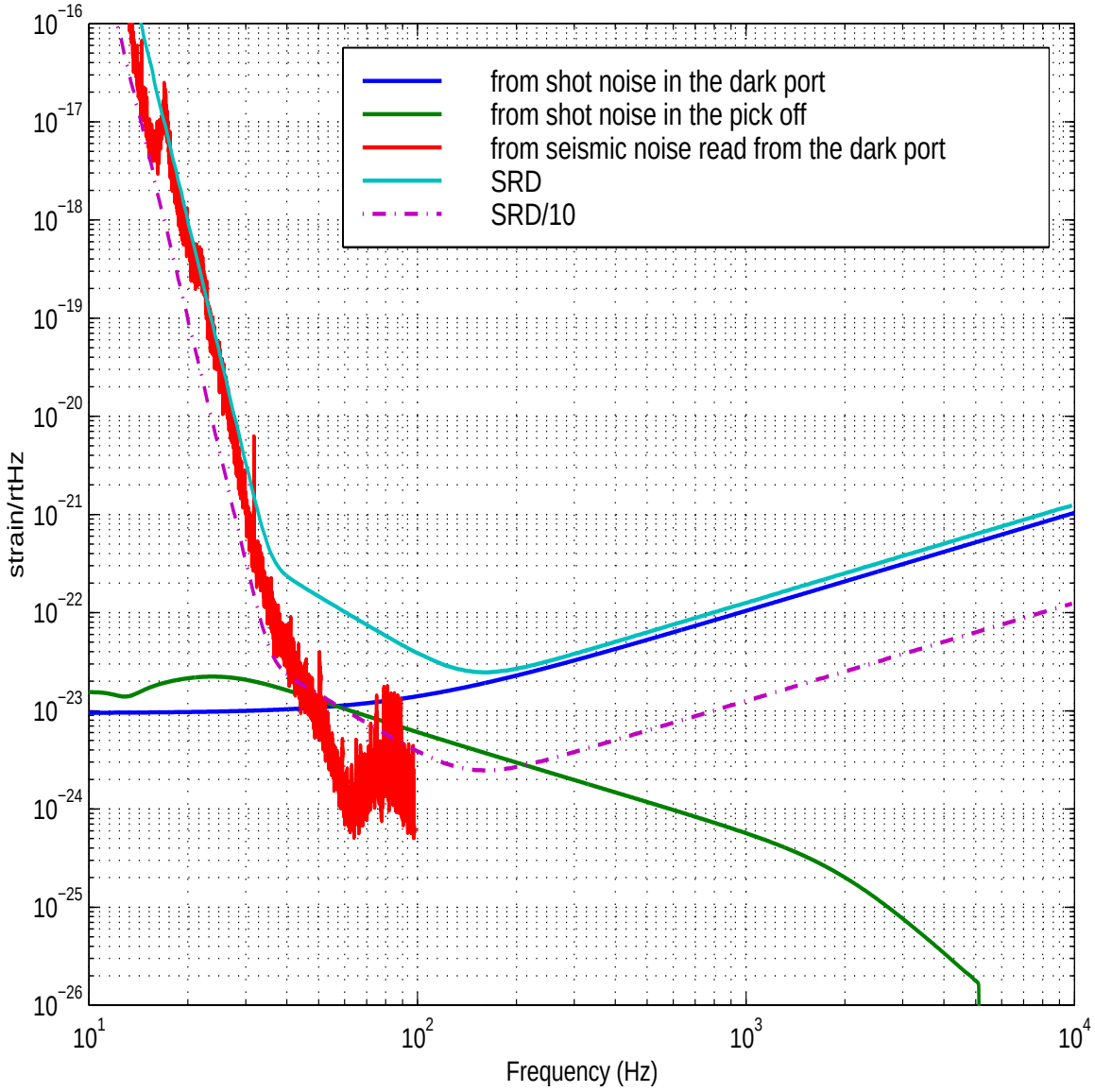

Figure 28: Contributions of the differential modes sensing and control system to the interferometer strain sensitivity (not including electronics noise). Also shown in the seismic noise as predicted by the model described in the text.

As Figure 28 shows, the feedthrough of shot noise from the Michelson sensor to the GW signal exceeds slightly (by up to a factor of roughly 1.5) the SRD/10 requirement. There are several possibilities for improving this:

- we've assumed the Michelson sensing noise can be subtracted from the GW signal up to 5% (noise reduction factor of 20); it may turn out to be possible to do a better job of subtracting this out (this is discussed in Appendix 4).
- the gain/bandwidth of the Michelson servo could be reduced by a factor of 2-3 to reduce the coupling; our model predicts that this could be done without exceeding the residual deviation requirement for the Michelson d.o.f. (we prefer to keep the bandwidth high in

LIGO-DRAFT

the design to accommodate larger than predicted seismic excitation of this d.o.f.).

- it may turn out that the quad-phase signal in reflection has a better shot noise sensitivity for the Michelson detection, and is stable over time, in which case we would use this sensor; in fact, the output of the FFT model predicts that the sensitivity of the reflection signal is roughly 8× more sensitive than the pick-off signal (the danger is that the reflection signal could be much worse, and could go through zero sensitivity, since it is proportional to the reflected carrier field).

4.3. Common Modes

4.3.1. Servo Design

The overall common-mode servo loop model schematically represented in Figure 52 in Appendix 2 was implemented in a Simulink® model. A detailed representation of the *Lp* servo blocks is shown in Figure 29. The plant block, *PLp*, comprises the optical plant pole at 91 Hz, the DC plant response in amperes per meter and the photodetection gain in volts per ampere. The controller block, *CLp*, consists of a gain stage, some real zeros and poles for the servo compensation, a combination of a 4th-order, 1 dB ripple, 40 dB attenuation elliptic bandstop filter (stop band 30 to 150 Hz) and a 4th-order, 1 dB ripple Chebyshev filter with cut-off frequency at 30 Hz to steeply roll off the gain to achieve the required 60 dB frequency noise suppression at 40 Hz and a multi-pole low-pass filter to achieve sufficient attenuation at the test mass resonance at 9.48 kHz. The pendulum block is made up of the suspension controller transfer function (1 Hz/40 Hz pole/zero pair), the coil driver sensitivity in volts per meter and the pendulum transfer function with resonant frequency at 0.74 Hz. Similarly, the servo blocks for the frequency controls are shown in Figure 30. The optical plant block, which is the same as for the *Lp* loop, is followed by two compensation paths, one to the mode cleaner length and the other to offset the error point of the mode cleaner servo.

Considerable care was exercised in designing the cross-overs between the Lp, the MC length and the MC additive offset actuation paths. The overall strategy was as follows:

- The Lp path has high gain below the pendulum resonance and then falls off as $1/f^3$.
- The MC length path is AC-coupled below the pendulum resonance and falls off as $1/f^2$ above it. The MC length path crosses over the *Lp* path at 3.5 Hz.
- A combination of a 4th-order, 1 dB ripple, 40 dB attenuation elliptic bandstop filter (stop band 30 to 150 Hz) and a 4th-order, 1 dB ripple, Chebyshev filter with cut-off frequency at 30 Hz in the Lp controller sufficiently attenuates the Lp gain so that it is at least 60 dB below the MC length gain (necessary to get the required 60 dB frequency suppression factor).
- In addition to the frequency noise suppression at 40 Hz, another important consideration that dictated the necessity for the bandstop filter between 30 and 150 Hz is the coupling of *Lp* to the gravitational-wave signal via the test mass drives (typically 5% in the suspensions). This coupling arises as follows: above ~40 Hz, the control signals derived from S_{RI} are correcting for the frequency noise at the output of the mode cleaner; a small fraction of the control signal propagates in the *Lp* path, and a small fraction of this signal couples into

LIGO-DRAFT

Lm, via imbalance in the suspensions. Thus the noise coupled in the GW signal through this path is:

$$\beta \cdot \left(\frac{G_{Lp}}{G}\right) \cdot L_0 \cdot \left(\frac{\delta\nu}{\nu}\right)_{\mathrm{mc}}$$

where β is the coupling of *Lp* drive to *Lm*, G_{Lp} is the open-loop gain in the L_p path, G is the overall open-loop gain for the S_{RI} loop, L_0 is the arm length, and $(\delta\nu/\nu)_{\mathrm{mc}}$ is the fractional frequency stability from the mode cleaner. For example, at ~100 Hz $L_0 \cdot (\delta\nu/\nu)_{\mathrm{mc}} = 1.5\times10^{-15}\,\mathrm{m}/\sqrt{\mathrm{Hz}}$. If we assume $\beta = 5\%$, then we require $(G_{Lp}/G) < -80$ dB to not exceed the SRD/10 level.

- In principle, the Lp and MC length paths should cross over with a relative phase of 90°, but these filters contribute significant phase lag at 3.5 Hz (30°) and the cross-over is not as stable as we would like. Moving the cross-over to lower frequencies is not feasible because the phase is not well-behaved around 2 Hz due to the dynamics of the mode cleaner length/frequency control system. More likely, the elliptic filter cut-off may be moved to higher frequencies at the cost of increased frequency noise above 40 Hz.
- The loop gain in the MC additive offset path is AC-coupled at frequencies below 100 Hz and has a $1/f$ slope at frequencies above 600 Hz. This affords a comfortable 90° relative phase between the MC length and MC additive offset at the 700 Hz cross-over, gives the required 30 dB of gain at 700 Hz and 90° phase margin at the unity gain frequency of 20 kHz.

Finally, the *lp* controls are shown in Figure 31. The *lp* controller *Clp* contains a resonant gain stage to suppress noise at the suspension vertical mode.

LIGO-DRAFT

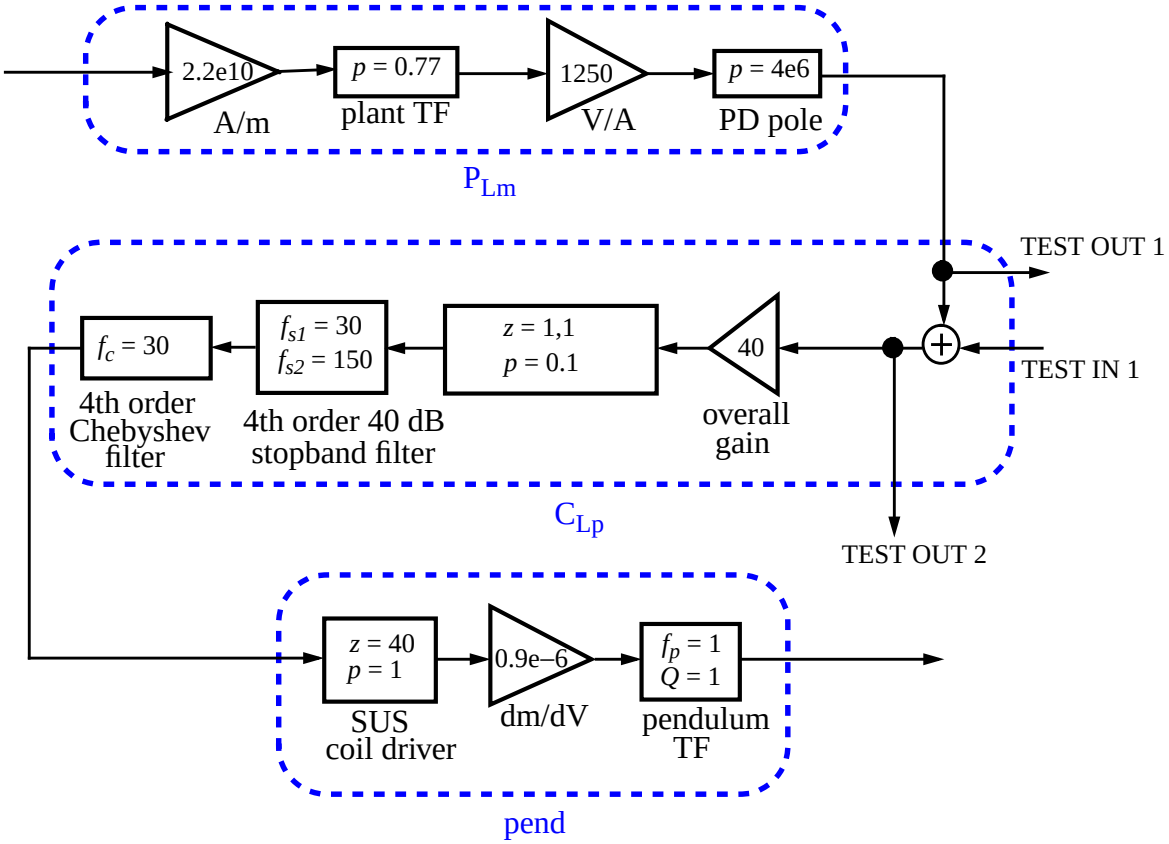

Figure 29: Control system blocks for the *Lp* loop. *z* refers to zero frequencies; *p* to pole frequencies; G to gain; f_p is the pendulum resonant frequency; f_{s1} and f_{s2} are the elliptic bandstop filter start and stop frequencies, respectively; f_c is the Chebyshev filter frequency. All frequencies are in Hz and gains are dimensionless, unless otherwise specified.

LIGO-DRAFT

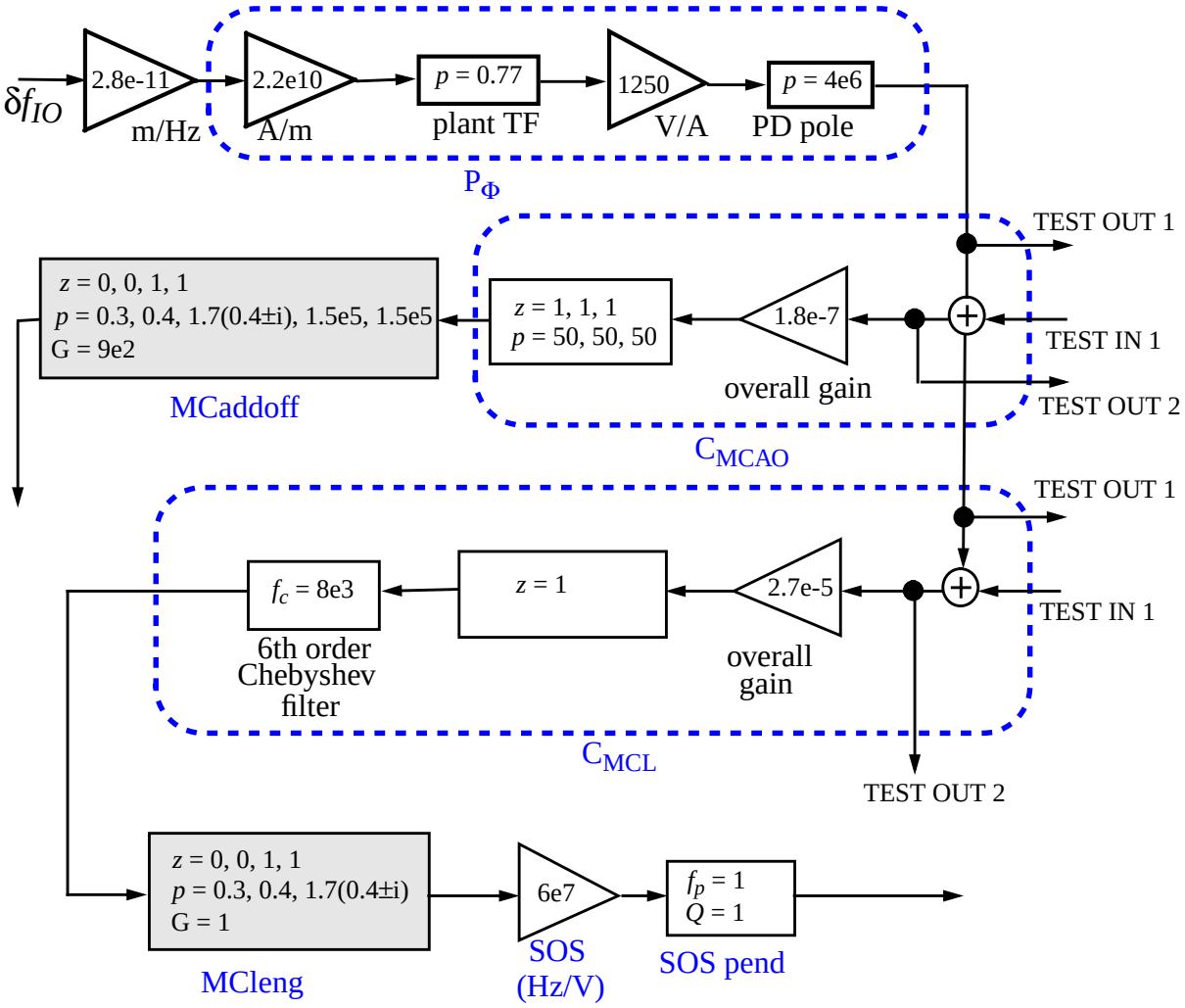

Figure 30: Control system blocks for the frequency loop. *z* refers to frequencies of zeros; *p* to pole frequencies; G to gain; f_p is the pendulum resonant frequency; f_c is the cutoff frequency for the Chebyshev filter to give −130 dB of attenuation at 25 kHz (internal resonance of the small optics. The poles, zeros and gains shown in the MCleng and MCaddoff blocks are fits to the closed-loop responses computed using a Simulink model of the mode cleaner servo. The fits are not very accurate in phase, even though the magnitudes correspond well. All frequencies are in Hz and gains are dimensionless, unless otherwise specified.

LIGO-DRAFT

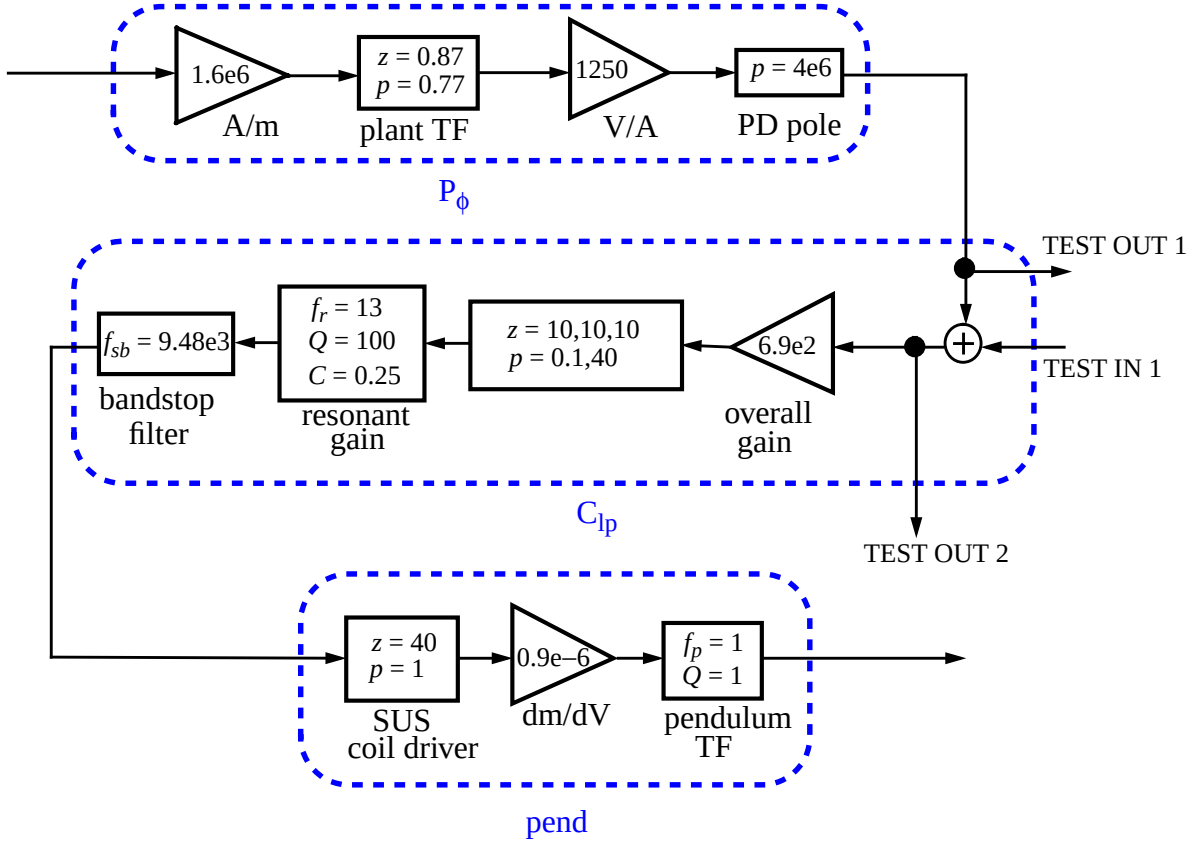

Figure 31: Control system blocks for the *lp* loop. *z* refers to frequencies of zeros; *p* to pole frequencies; G to gain; f_p is the pendulum resonant frequency; f_r is the frequency of a resonant gain stage to suppress noise due to the vertical mode coupling (see eqn. (3)); f_{sb} is the center frequency of a bandstop filter for attenuation of the test mass resonance. All frequencies are in Hz and gains are dimensionless, unless otherwise specified.

4.3.2. Control System Performance

The control blocks of Figures 29, 30 and 31 were implemented in the common-mode controls model shown in Figure 52; the servo design was tested in Simulink®. The open loop gains and the residual phase and frequency noise spectra are shown below.

LIGO-DRAFT

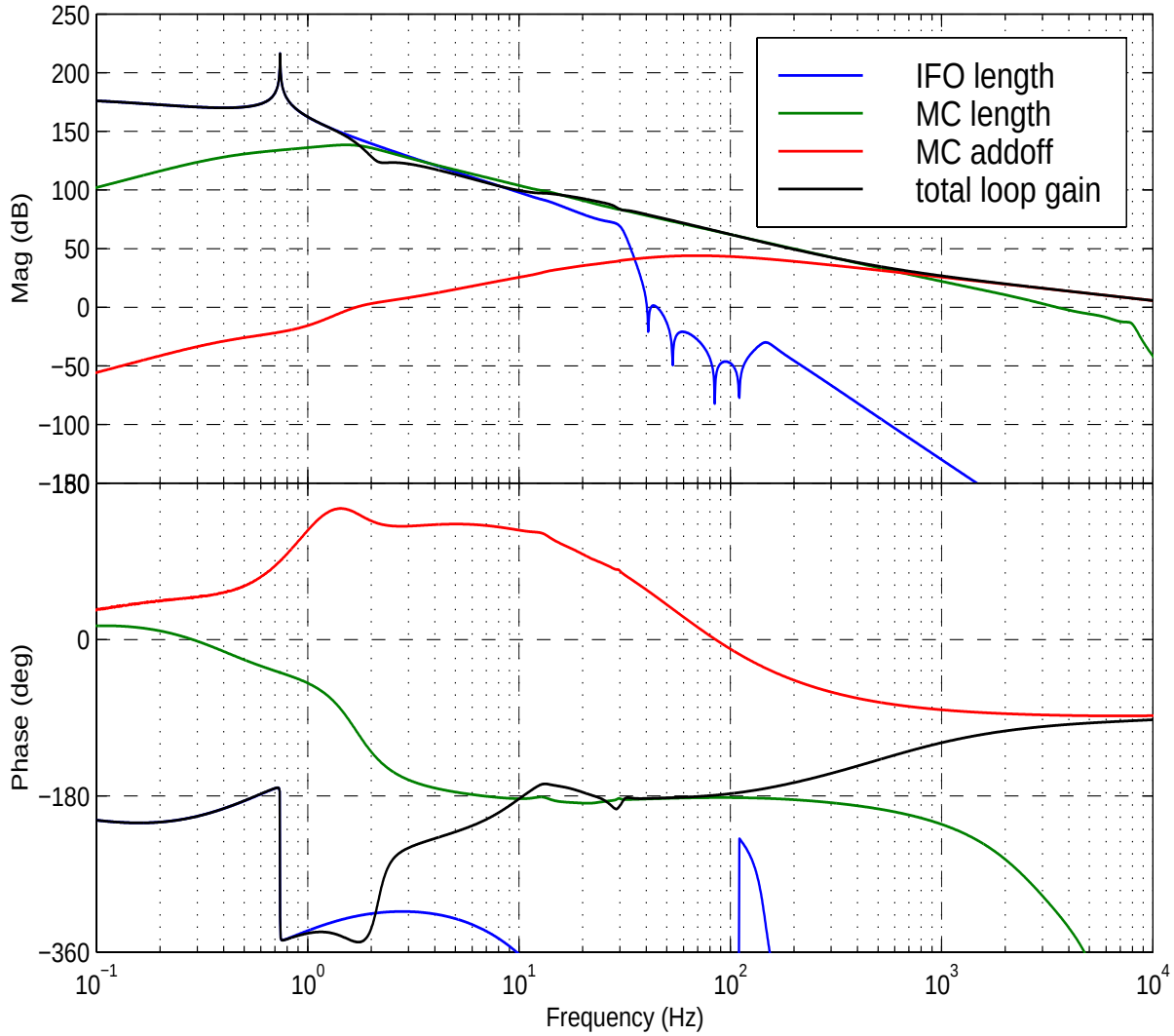

Figure 32: Open loop gains for the Lp/frequency controls. The Lp/MC length cross-over occurs at 3.4 Hz and the MC length/ MC additive offset cross-over occurs at 800 Hz.

LIGO-DRAFT

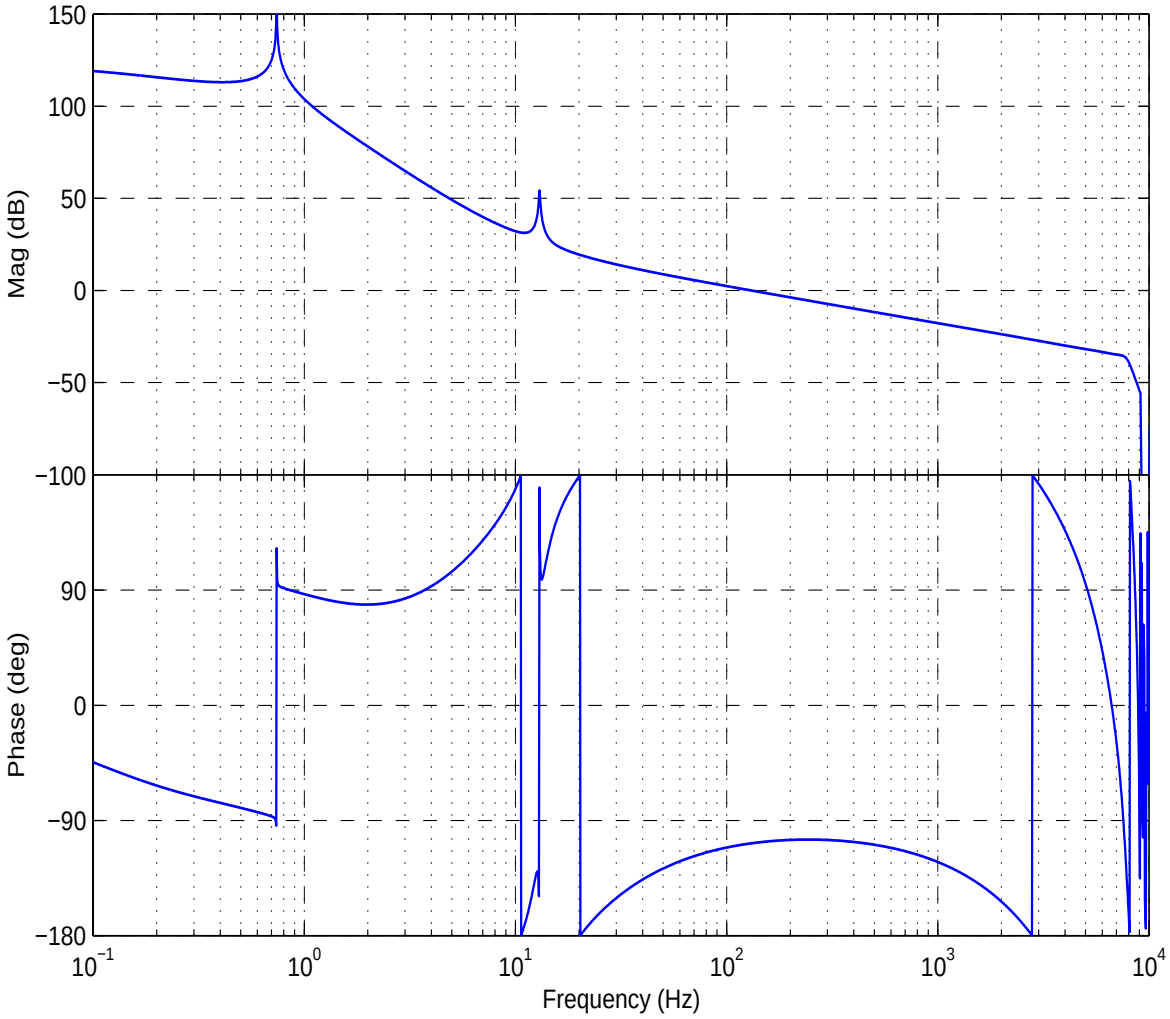

Figure 33: Open loop gain for the lp loop.

LIGO-DRAFT

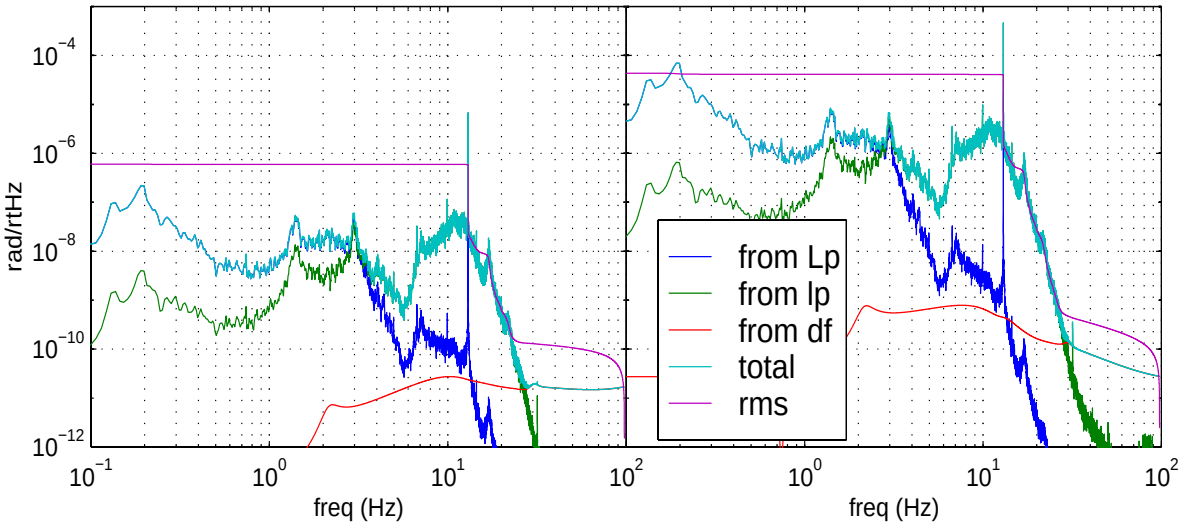

Figure 34: Residual phase deviations for Φ (left) and ϕ (right), shown as an amplitude spectral density and an integrated rms vs. frequency (vertical scales are the same for both curves). The rms residual Φ deviation is 6×10^{-7} rad and the rms residual ϕ deviation is 4×10^{-5} rad. Both are dominated by motion at the 13 Hz vertical mode of the RM and ITMs, i.e. *lp* motion.

LIGO-DRAFT

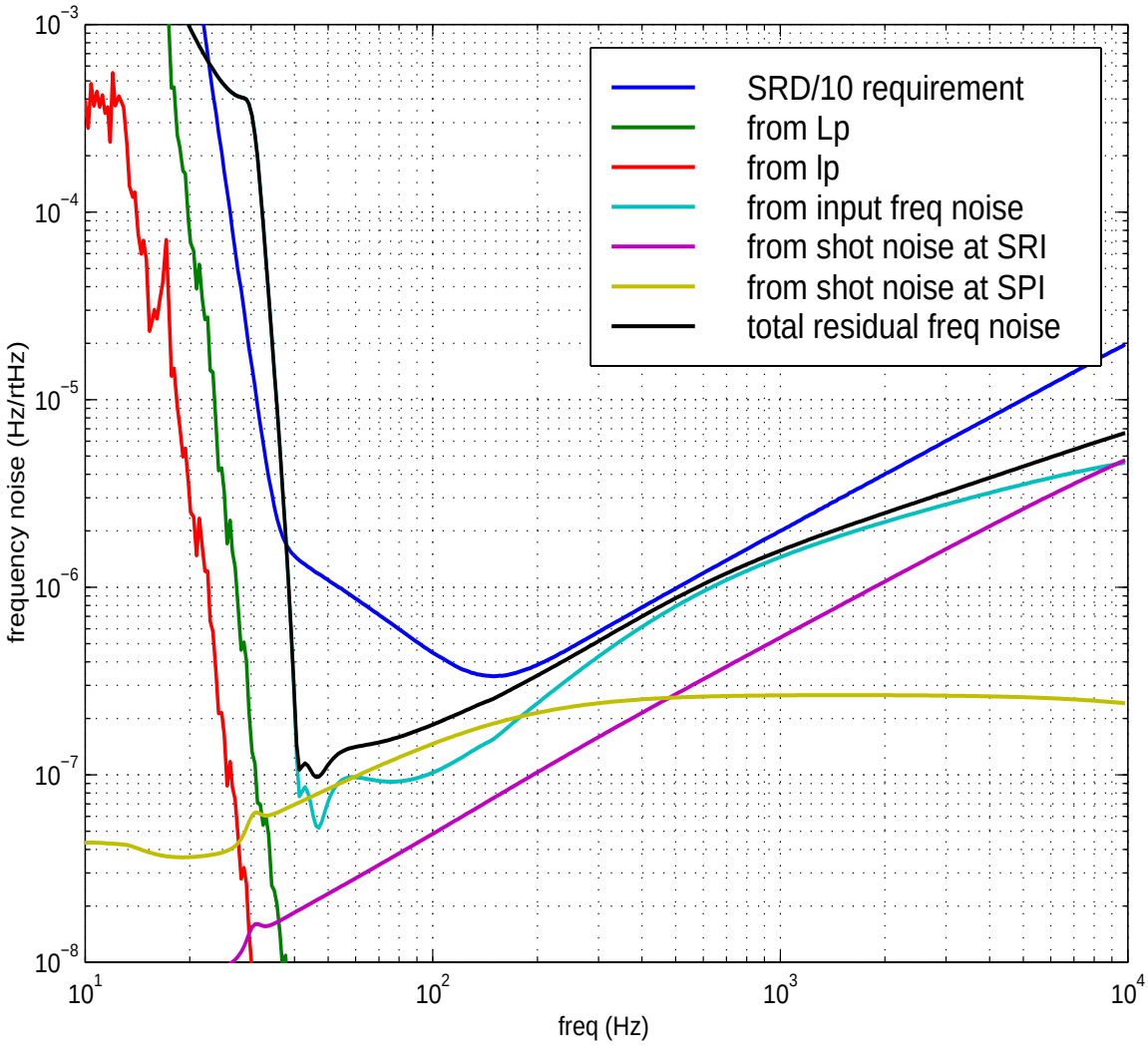

Figure 35: Residual frequency noise. The dominant contribution above 10 Hz is the incoming frequency noise from the IO mode cleaner with some added contribution from the shot noise in the pick-off port sensor. The shot noise at the S_{RI} sensor has an f dependence due to the plant pole at 0.77 Hz, while the shot noise at S_{PI} has no frequency dependence since the optical plant has a closely spaced pole and zero. While no requirement for frequency noise is specified below 40 Hz, it should be noted that the elliptic filter at 20 Hz just barely attenuates the frequency noise to the SRD/10 level in the 10 to 40 Hz band.

A summary of the loop performance data for common-mode degrees of freedom is given in Table 14.

4.4. Test Mass Damping Paths

In Detection Mode, the local damping for the axial pendulum mode is active only for the beamsplitter and recycling mirror; the four test masses are instead damped using the four interferometric error signals. For the *Lm* and *Lp* d.o.f. this damping has been included in the

LIGO-DRAFT

Performance Data	***Lp/df***	***lp***	***Units***
Gain at DC	180	120	dB
Unity gain bandwidth	21000	130	Hz
Phase margin	94	70	degrees
Lp/MC length crossover frequency	3.7		Hz
MC length/additive offset crossover freq.	650		Hz
Gain at 9.48 kHz	–200	–160	dB
Residual phase deviations	6×10^{-7}	4×10^{-5}	$\text{radian}_{\text{rms}}$
Error signals	0.2	0.03	V_{rms}
Drive signals	Lp: 3.1 MC leng: 1200 MC addoff: 2.3	lp: 1.1	μm_{rms} Hz_{rms} mHz_{rms}

Table 14: Control system characteristics and performance data for common-mode degrees of freedom.

previous servo designs, since these control signals are sent to the end test masses at the pendulum frequency. For the *lm* and *lp* d.o.f., however, the control signals are sent to the beamsplitter and

LIGO-DRAFT

recycling mirror, respectively. As shown in Figure 36, an additional feedback path to the test masses is included in these loops for damping.

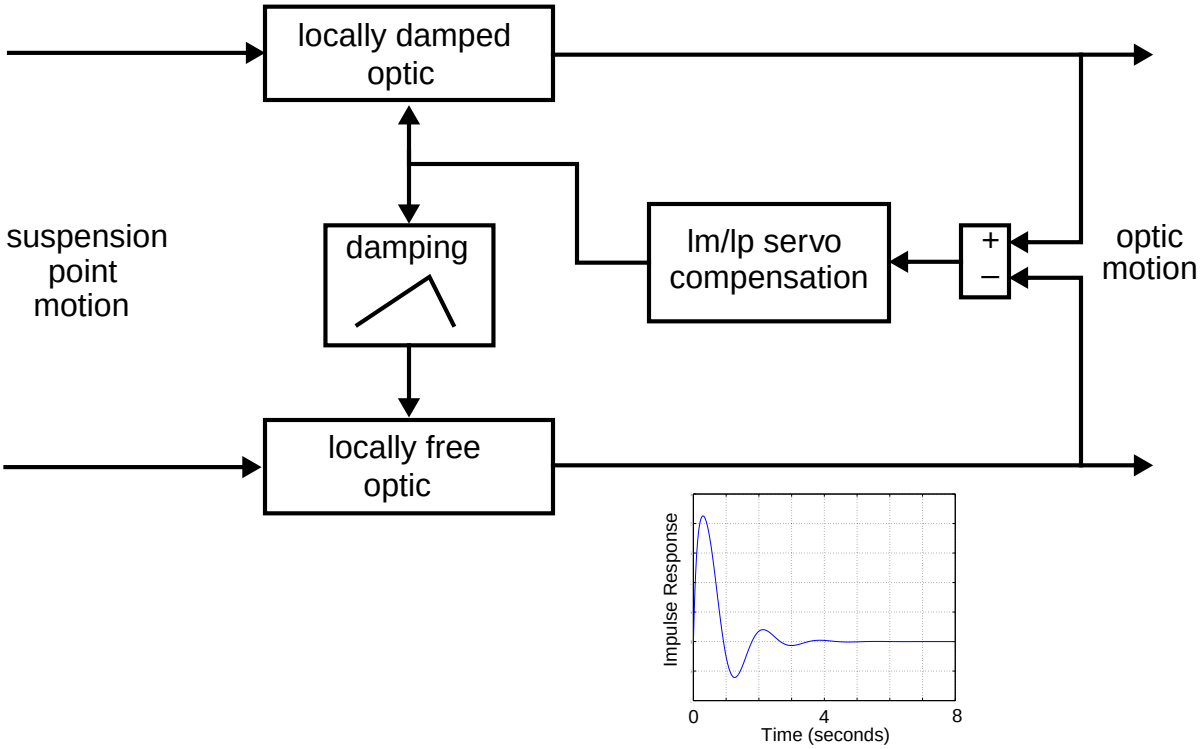

Figure 36: Block diagram indicating the test mass damping path for the Michelson and recycling cavity servos. The 'locally damped optic' indicates the beamsplitter or recycling mirror, and the 'locally free optic' indicates the (input) test masses. The damping path consists of a zero at DC, and a Chebyshev low-pass filter at 1 Hz (more low-pass filtering is added for the Michelson case). The graph shows the impulse response from suspension point to optic motion for the 'locally free' optic, for the damping loops detailed below; the response corresponds to a *Q* of 1.3.

Since the end test masses are damped by the *Lm* and *Lp* loops, the *lm* and *lp* damping paths can be sent to the input test masses only. As with the *Lp* path, care must be taken to adequately filter

LIGO-DRAFT

these paths so that the sensing noise does not feed into the GW channel. The filtering requirements and designs for the damping paths are given in Table 15.

Loop	***Sensitivity @40 Hz, m/√Hz***	***GW channel coupling***	***Damping path gain req. @40Hz***	***Damping servo***
Recycling cavity	6×10^{-17}	5%	–35 dB	Zero @DC 2nd order Chebyshev @1Hz (+pole@20Hz for stability)
Michelson	1.5×10^{-16}	100%	–65 dB	Zero @DC 2nd order Chebyshev @1Hz 4th ord. elliptic @20Hz, 30dB stop

Table 15: Requirements and parameters for the *lm* and *lp* test mass damping paths. For each loop the sensitivity is limited by shot noise. The gain requirement (4th column) refers to the ratio between the damping path gain and the overall loop gain for that d.o.f.

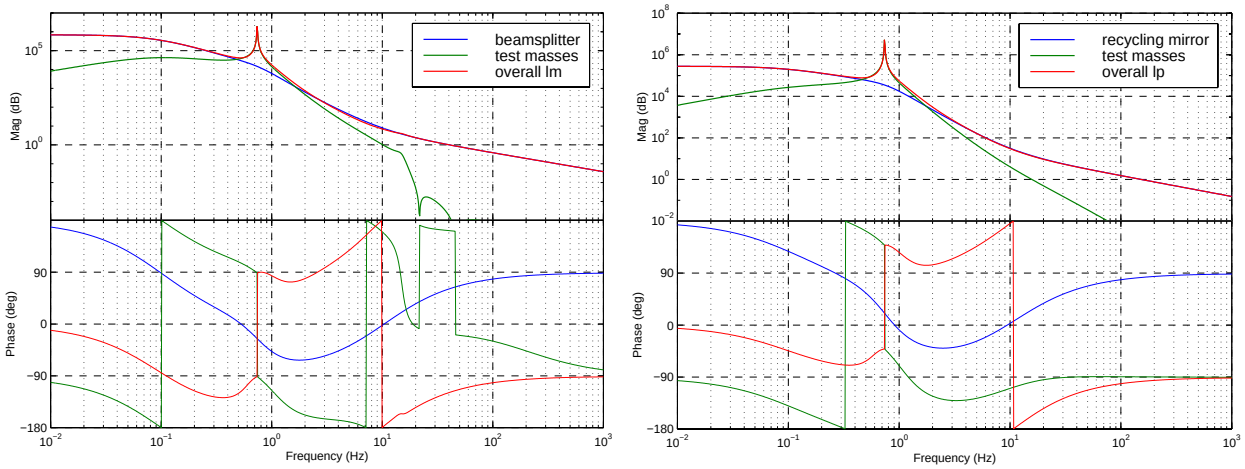

Figure 37: Open loop responses for the Michelson (left) and recycling cavity (right) loops, showing the test mass damping paths.

LIGO-DRAFT

5 SIGNAL CONDITIONING

5.1. ADC & DAC Noise

Tests performed by CDS on VMEbus analog I/O boards from various vendors have identified the Pentek 6102 8 channel A/D & D/A converter as best suited to our application. Several measurements of the A/D & D/A noise have been performed; the results are shown in Figure 38.

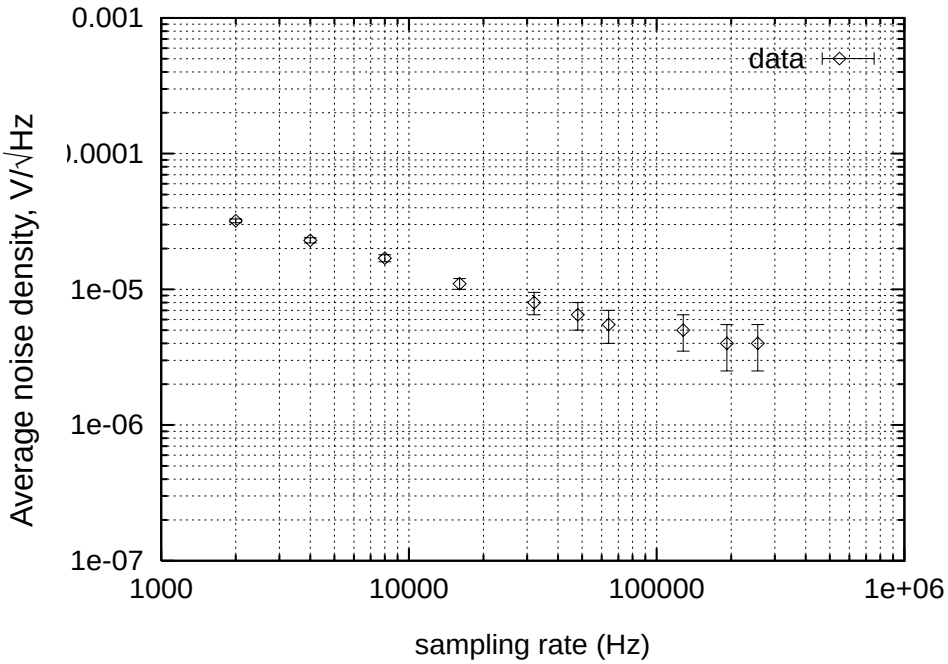

Figure 38: Input noise of the Pentek 6102 ADC, measured with a 1 kHz near full-scale sine wave. Data points represent the average noise density around 3 kHz. The measurement was also made using a random noise input signal, whose spectrum approximates that of the estimated AS port error signal, with a notch at 200 Hz to uncover the ADC noise; the results for the ADC noise were the same as shown above.

5.2. Pre-ADC Conditioning

5.2.1. Anti-Aliasing Filter

An anti-alias filter must be provided to prevent the shot noise above the Nyquist frequency of 8192 Hz from being aliased into the GW band. The current design for the AA filter is a 6th-order elliptic low-pass, with a cut-off of 7500 Hz, a stopband attenuation of 60 dB, and 0.1 dB of pass-band ripple. The order and attenuation of the AA filter are constrained by the requirement that the filter produce little phase lag at the servo unity gain frequencies; this design produces ~8 deg of phase lag at 300 Hz. The attenuation of this filter is -23 dB at 9.4 kHz, thus the shot noise that is aliased down to the upper GW band frequency of 7 kHz is less than 1/10 the amplitude of (non-aliased) 7 kHz shot noise.

LIGO DRAFT

5.2.2. Whitening Filter

The function of the pre-ADC signal conditioning is to match the excursions of the demodulator outputs to the input range of the ADC (with some safety factor), and to ‘whiten’ the demodulator outputs so that the voltage noise due to shot and thermal noise is at least a factor of 10 above the system’s electronics noise. We use the term ‘whiten’ to refer to a filtering function that increases the high frequency components of a signal, relative to the low frequency components.

There are some constraints in choosing the amount of whitening to be applied. A potential limit comes from the wire resonances, which produce the largest signals in the spectral region dominated by shot noise. It is not feasible to filter the wire resonances prior to sampling, and so the gain boost provided by the whitening filter must not be so large that the ADCs saturate on the wire resonance signals. This is not a very restrictive limit in practice – the ratio between the wire resonance rms signal and the shot noise is ~150 $Hz^{1/2}$, whereas the ratio of the ADC peak range to the ADC noise is ~10^6 $Hz^{1/2}$. A more relevant reason to limit the whitening to the amount needed is to provide as much headroom as possible for excitation signals applied at high frequencies.

The pre-ADC signal conditioning is most crucial for the anti-symmetric port signal. Here the dynamic range of the signal is the largest, and the electronics noise requirement is the most severe. We thus restrict the discussion here to the filter design for the AS port signal; the signals from the other ports can use the same or lower-order filter designs. As discussed in Section 2.1., we estimate 8 photodetectors will be used at the AS port. There are two basic approaches to combining the signals from the detectors:

- maintain individual channels for each photodetector up through sampling at the ADCs, and sum the digitized samples in software
- sum the (analog) channels together prior to sampling, most likely after demodulation

Of course, some combination of the above could be performed, summing subsets of analog channels before sampling, but this approach doesn’t seem to hold any particular advantages. The choice of which approach to take will be made as part of the LSC CDS final design. Here we present a filter design for the second approach (analog sum). For demonstrating design feasibility, this is more meaningful since higher demands are made on the whitening filter in this case.

LIGO-DRAFT

The signal chain between length deviations and the ADC input for the AS port is shown in Figure 39. Because there are significant L_m signals in the 0–10 Hz band, the rise in the whitening

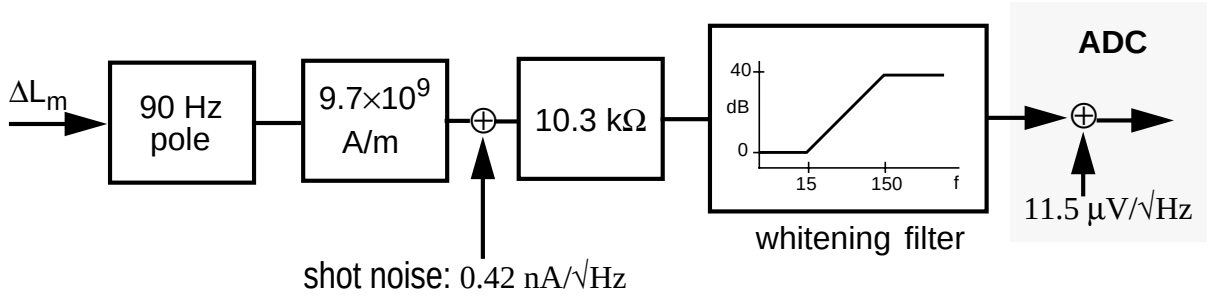

Figure 39: Signal chain between L_m residual length and ADC input, representing the sum of all channels at the AS port. Anti-aliasing filters not included. The demodulation gain and pre-ADC DC gain are represented by the '10.3 kΩ' block. This gain value is chosen so that the rms signal level at the ADC input is 1 V-rms (ADC input range is ±10 V). The whitening filter consists of 2 zeros (at 15 Hz) and 2 poles (at 110 Hz).

filter should not begin below ~10 Hz. We find that 2 zero-pole pairs (at 15 & 150 Hz, respectively) are required to lift the $f > 100$ Hz portion of the GW channel spectrum 10-15× above the ADC noise. The spectrum of the whitened AS port signal is shown in Figure 40.

LIGO-DRAFT

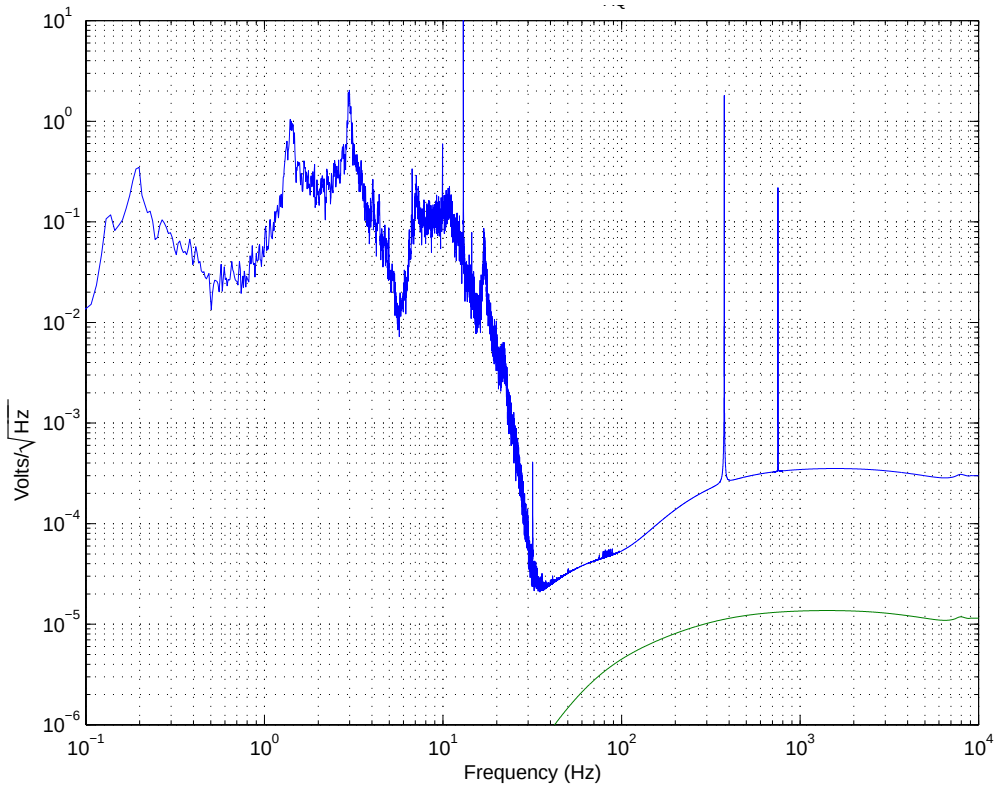

Figure 40: Spectrum of the whitened antisymmetric port error signal (upper curve); this signal is sent to the anti-aliasing filter, then to the ADC. The lower curve is the ADC voltage noise, multiplied by the closed loop gain of the L_m servo; the ADC noise is seen to be at least 10× below the signal. The integrate rms level of the signal over the bandwidth is 1 V-rms.

For the remaining digitized signals, S_{PQ}, S_{PI} and S_{PQ}, one 15/150 Hz filter section is required. A summary of the whitening filtering for all channels is given in Table 16.

Channel	***No. of 15/150 Hz whitening stages***	***Post demod. DC gain***	***Shot noise signal at ADC input***
S_{AQ}	2		300 µV/√Hz
S_{PQ}	1		250 µV/√Hz
S_{PI}	1	0.0265	80 µV/√Hz
S_{RI}	1	0.226	60 µV/√Hz

Table 16: Characteristics of the pre-ADC whitening filters for the demodulator signals to be digitized. The spectra of the whitened signal are shown in Figures 40 and 44.

LIGO DRAFT

5.2.3. ADC headroom

We have adopted a headroom factor of 20 for the ratio between the ADC peak-to-peak range and the predicted rms signal level at the ADC input. We predict this is sufficient headroom to avoid saturating the ADC for the following reasons:

- the suspension point excitation data (which derive from measured ground noise) show a ratio of only 6:1 for the peak excursion to rms fluctuation ratio.
- at the first two stack resonant frequencies, which contribute significantly to the residual L_m, the ground noise spectrum we use for the simulations (from seismometer measurements in LA) is higher than the canonical 10^{-9} m/√Hz that is, on average, characteristic of both sites; in particular, our model spectrum is 10× above this level at 1.5 Hz and 3× above at 3 Hz – thus we believe we are designing to a worst (worse) case.

For a closer examination of the spectral content of the residual error signal, we show in Figure 41 a 1/3-octave analysis of the whitened error signal.

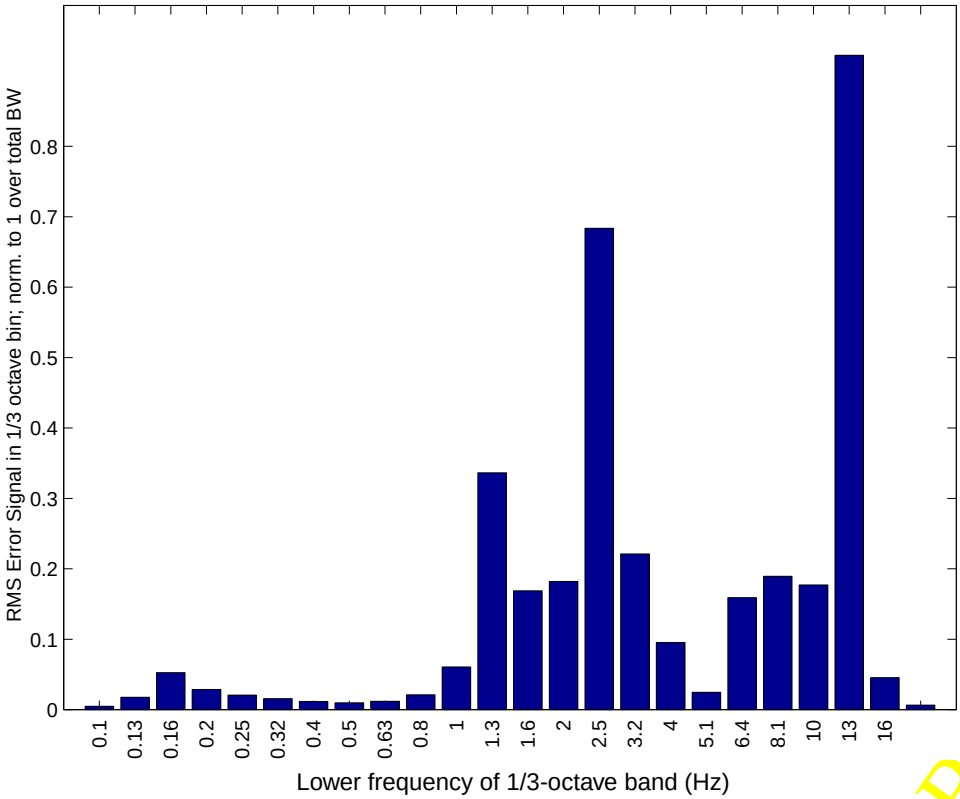

Figure 41: Decomposition of the L_m whitened error signal into 1/3-octave bands. The largest contributors to the signal are the two lowest stack modes (at 1.5 and 3 Hz) and the vertical mode of the suspension (at 13 Hz).

LIGO-DRAFT

5.3. Post-DAC Conditioning

The presence of DAC output noise requires the use of an analog 'dewhitening' filter at the DAC output. As with the whitening filter, the dewhitening filter basically makes up for the mismatch between the dynamic range of the interferometer signal and the dynamic range of the DAC (ADC). It is not surprising that the mismatch is even larger at the output than at the input, since the error signal is suppressed by the loop gain, but the control signal contains the full amplitude necessary to correct for ground motion. The problem is illustrated by Figure 42, which shows the spectrum (and integrated rms) of the signal at the input to the suspension controller, for the L_m loop (i.e., the input of one of the ETM controllers). The rms voltage is 2 V-rms (going into a ±10 V SUS controller range), but the lowest signal level is ~30 nV/√Hz, which is nearly 400× smaller than the DAC voltage noise. However at the high frequency end of the GW band, shot noise produces a significant signal level, ~15 mV_{rms}; thus if everything above f ~ 40 Hz were boosted by a gain of a few thousand, the shot noise would saturate the output. So prior to the DAC output, we need a digital filter which provides gain for frequencies from ~30 – few hundred Hz to lift the signal above the DAC noise; the analog dewhitening filter is then the inverse of this digital filter.

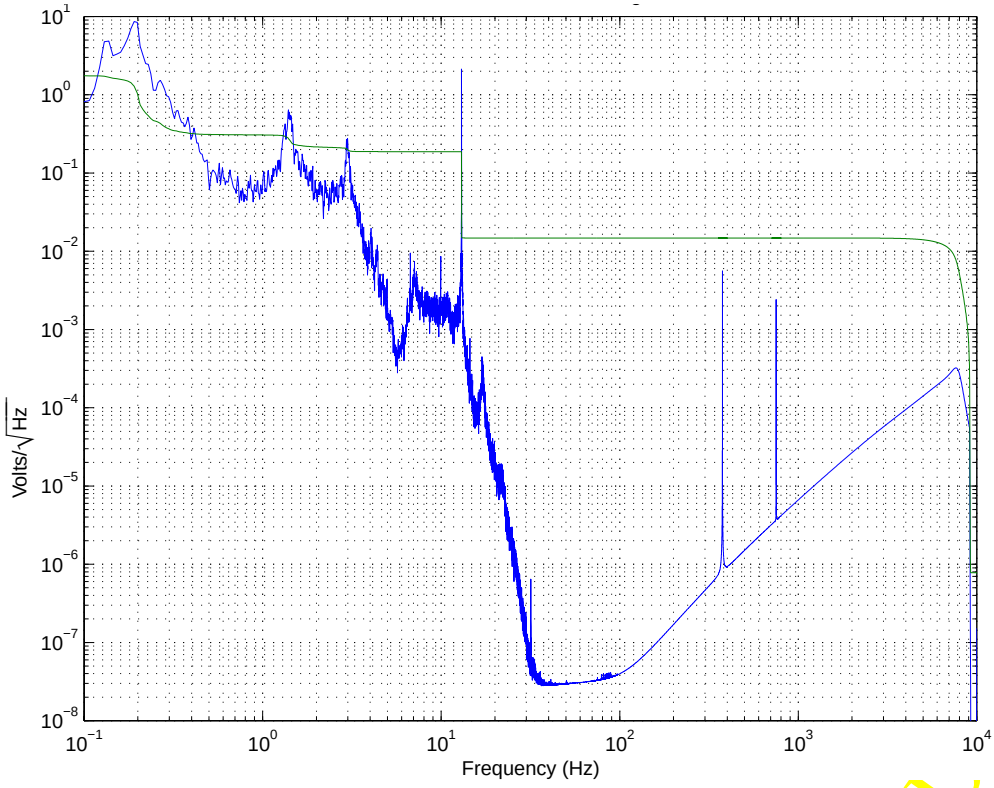

Figure 42: Spectrum and integrated rms of the L_m control signal at the input to one of the ETM suspension controllers.

LIGO-DRAFT

The following dewhitening filter was designed to perform this task:

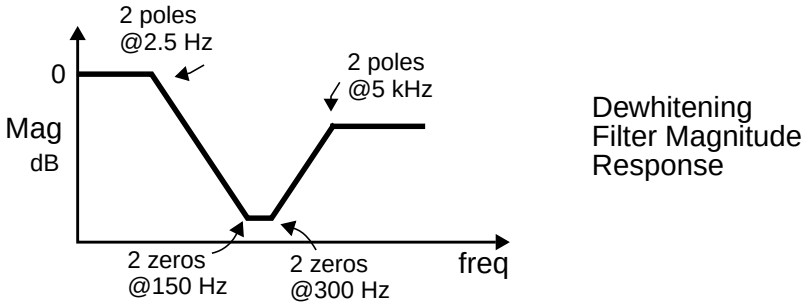

When the inverse of this dewhitening filter is moved into the digital domain, the spectrum of the DAC output becomes as shown in Figure 43. Also shown in the DAC noise level (multiplied by the closed loop gain of the L_m servo); the interferometer signal is at least 10× above the DAC noise at all frequencies.

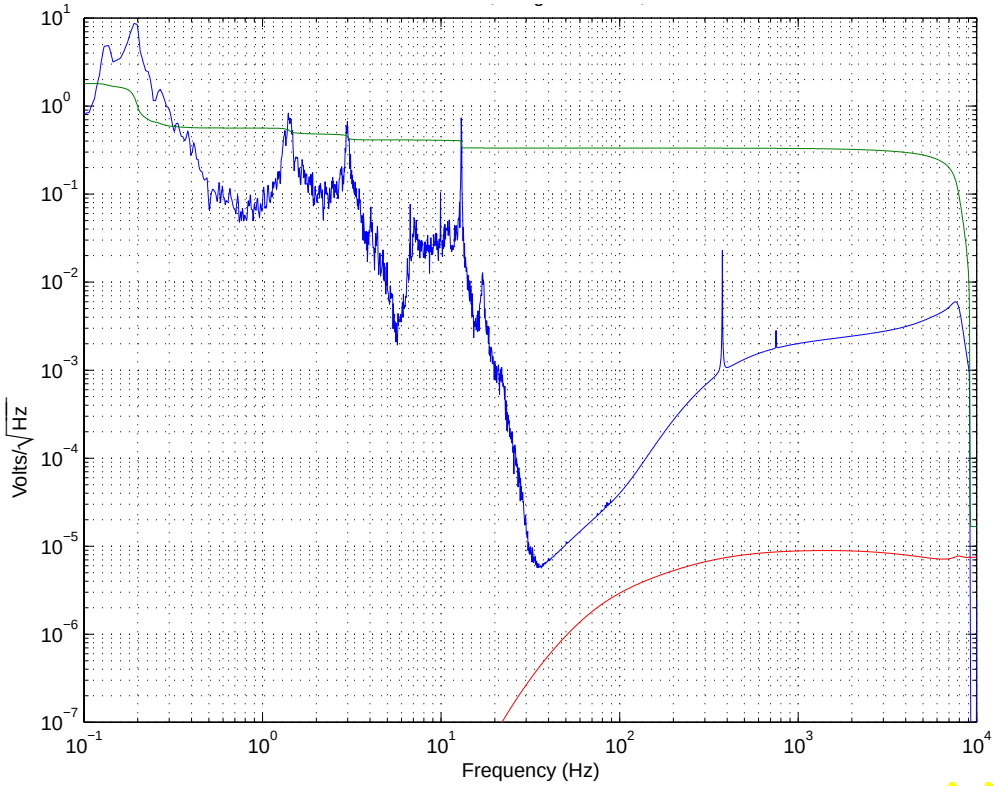

Figure 43: Spectrum and integrated rms of the L_m control signal at one of the DAC outputs (i.e., same signal as in Figure 42, prior to de-whitening); also shown (lower, red curve) is the DAC voltage noise density, multiplied by the closed loop gain of the L_m loop.

The dewhitening filters for all control signals are summarized in Table 17 and the spectra for the remaining DAC outputs are shown in Figure 44.

LIGO-DRAFT

Channel	*Filter poles and zeroes*
Lm	poles: 2.5, 2.5, 5000, 5000 zeroes: 150, 150, 300, 300
lm	poles: zeroes:
Lp	poles: 2.5, 2.5, 5000, 5000 zeroes: 150, 150, 300, 300
lp	poles:20 zeroes:50

Table 17: Poles and zeroes of the post-DAC dewhitening filters for the control signals for all degrees of freedom. All pole and zero frequencies are given in Hertz. The spectra of the DAC outputs before dewhitening are shown in Figures 40 and 44.

LIGO-DRAFT

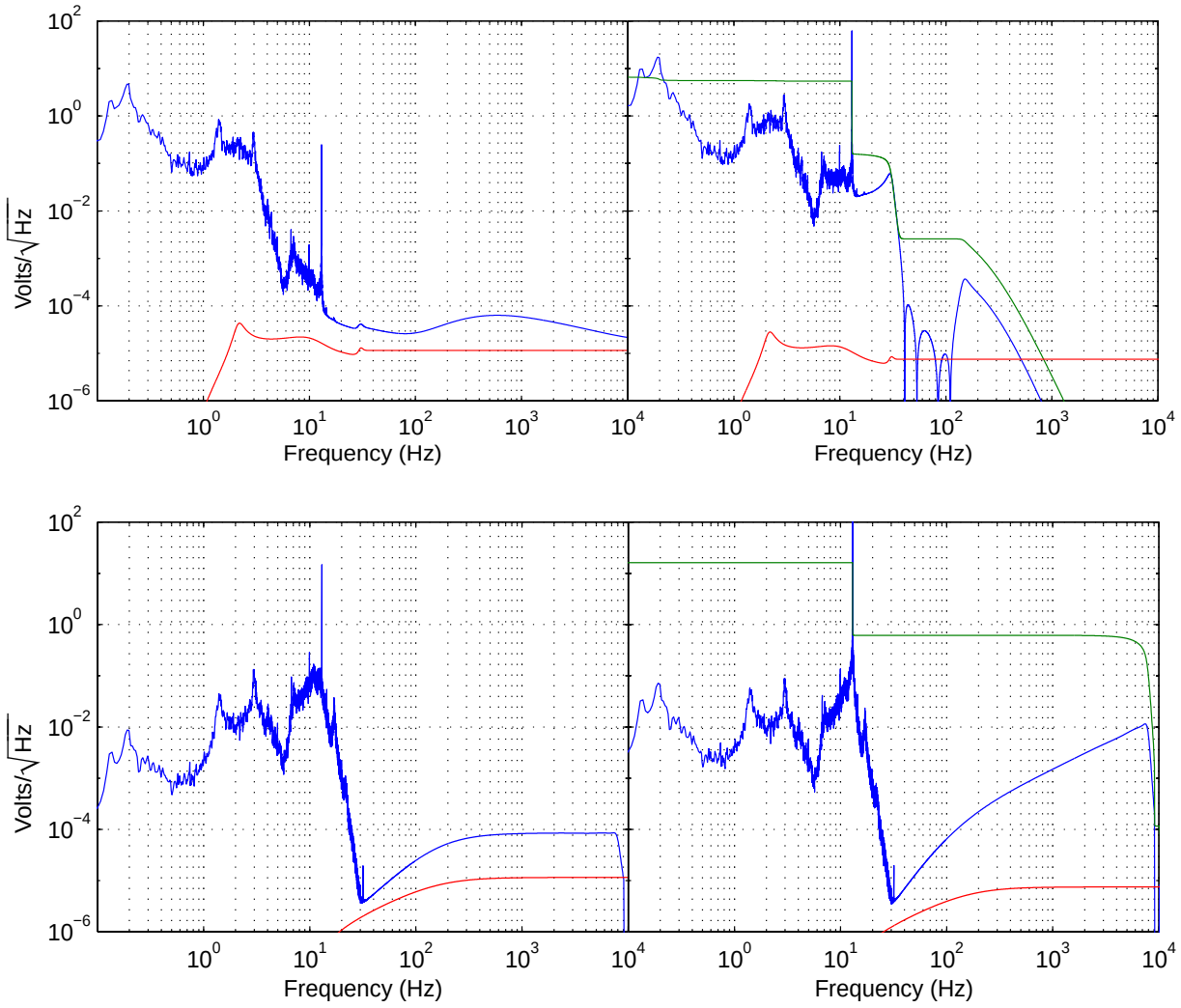

Figure 44: Whitened inputs to the ADCs for the error signals, S_{RI} (top left) and S_{PI} (bottom left) and the pre-dewhitened ADC outputs for the control signals Lp (top right) and lp (bottom right). The red curves are the ADC noise (left plots) and the DAC noise (right plots). The green curves on the right are the integrated rms of the DAC outputs on the same plot.

LIGO-DRAFT

5.4. Digital domain

The transfer function of the digital filter is found by taking the complete transfer function of the electronics (minus the AA filter and any notch filters), and multiplying it by the inverse of the whitening and dewhitening filters, as shown below:

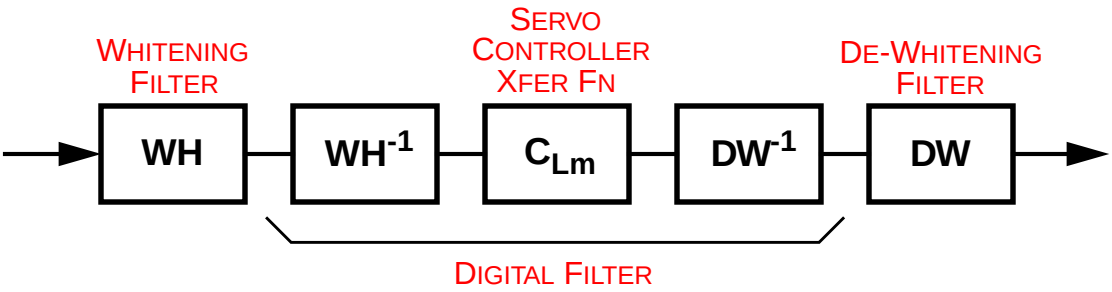

For the L_m loop, this gives the transfer function (magnitude only) shown in Figure 45.

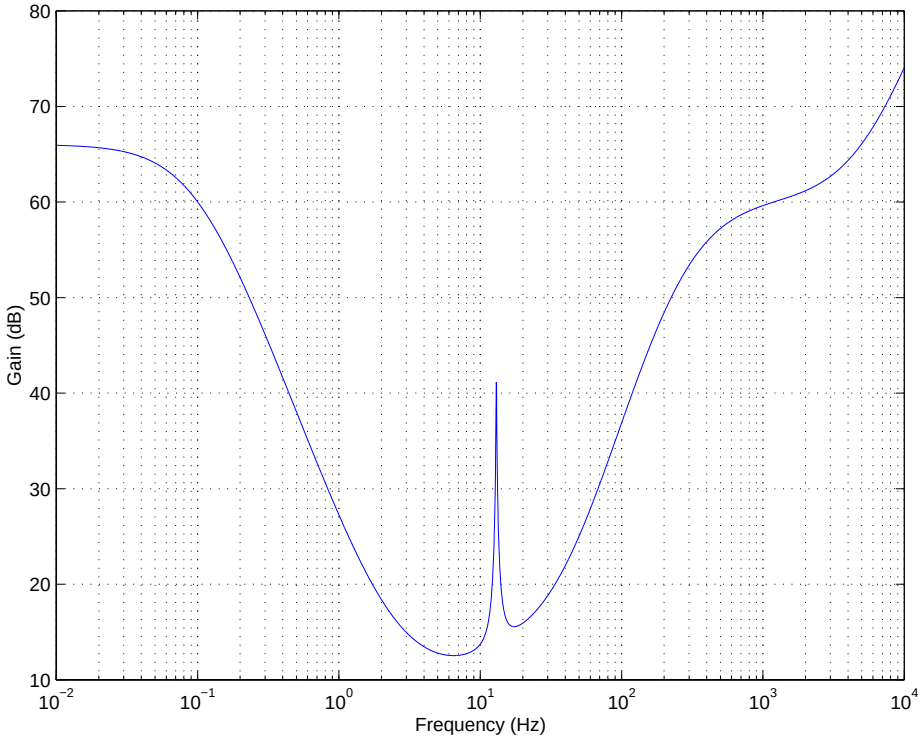

Figure 45: Magnitude response of the analog prototype of the digital filter for the L_m loop. The true response of the digital filter would of course deviate from this near the Nyquist frequency of 8.2 kHz.

LIGO-DRAFT

6 CALIBRATION & DIAGNOSTICS

LSC carries responsibility for calibration of the recorded interferometer strain signal. The task involves two steps; to determine the ratio between the recorded signal S_{AQ} (or one derived from it) and an independent physical measurement of differential mirror motion, and then to maintain or update this ratio throughout interferometer operation as operating conditions vary. An absolute accuracy corresponding to $\pm 5\%$ in strain amplitude over the band spanning $40\ \text{Hz} < f < 10\ \text{kHz}$ and $\pm 50\mu\text{s}$ in arrival time (or equivalent waveform phase) must be maintained, without encroaching on the interferometer's scientific availability.

The primary chain of reference for calibrating the interferometer readout will be based on the 1.06 μm wavelength of the Nd:YAG laser, through a procedure described in 6.2. This procedure is used in the suspended LIGO prototypes and has been found to be highly reliable, but nonetheless relies on stability of parameters measured "off-line" (for example, the coil/magnet force per unit current), requires high linearity to extrapolate signal levels over several decades, and shares signal paths and equipment with the operational control system. Due to the fundamental importance of the calibration function to LIGO's scientific mission, even where these potential sources of systematic error can be rigorously evaluated there remains strong motivation to provide an independent and redundant means of verification. Insofar as possible, such a "secondary" calibration standard should be based on a physically distinct mechanism and chain of reference. As a result, we propose to include a redundant, independent force calibrator based on photon recoil pressure, which we describe in 6.2.

Stability of the readout over time will be ensured by:

- choosing readout signals with minimal sensitivity to variable parameters
- periodic high-accuracy transfer function characterization using injected stimuli, and
- model-based reconstruction of the transfer function based on the response to continuous low-level stimuli embedded in the data stream.

The calibration system will also permit injection of arbitrary test waveforms, which may be used to simulate possible gravitational signals or to diagnostically excite specific response features found in the interferometer. These functions will be provided as a subset of the generic stimulus-response test capabilities provided for LSC and interferometer-wide diagnostics.

6.1. Primary Calibration

The primary calibration is based on the Nd:YAG laser wavelength, as follows:

- First, with the recycling mirror and ETM's deliberately misaligned, the single-bounce Michelson interferometer is driven through at least one full order using the suspension force actuators on each ITM at low frequencies (10 to 50 Hz; in acquisition mode, the coil driver is capable of moving a ITM by 1 μm p-p at 60 Hz). The AS port demodulator signal and the drive current corresponding to a full order are recorded (at various drive frequencies). The demodulator signal is a sine wave as a function of the Michelson phase; the peak-peak value of this signal is all that is needed for the second step.
- Second, the short, unrecycled Michelson is locked at low gain and the demodulator signal is

LIGO DRAFT

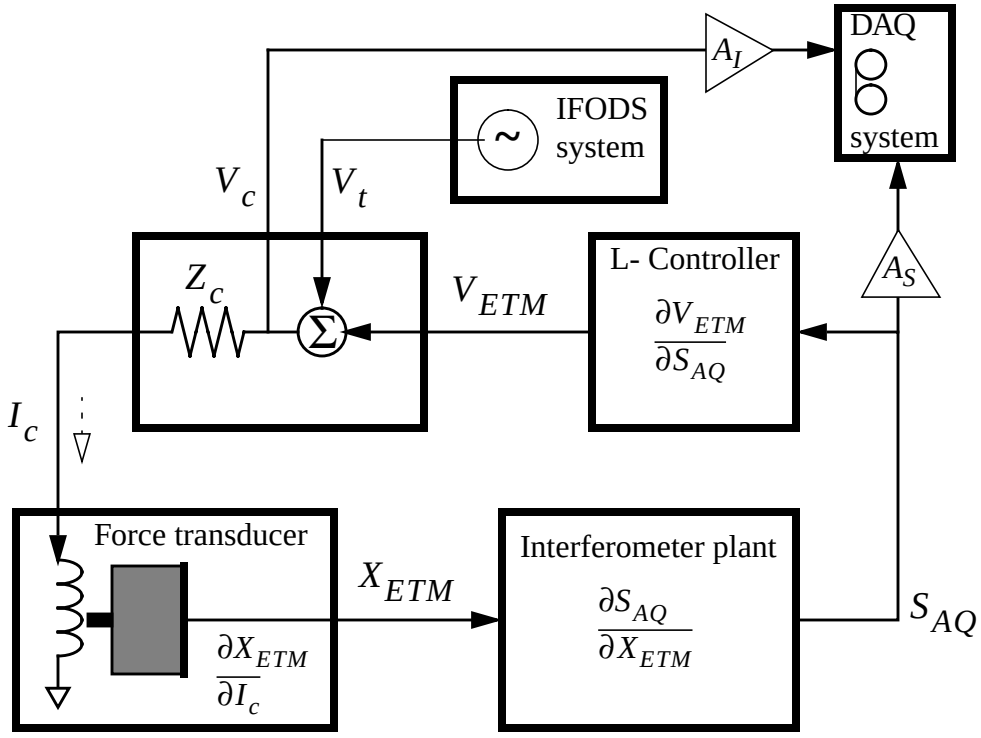

Figure 46: Simplified schematic of primary calibration in operation mode, showing the multiplicative factors subject to initial error or drift.

monitored as smaller and smaller currents are injected to determine the linearity of the response (which must be corrected for the loop gain of the Michelson control, measured separately). The frequency response of drive current to demodulator voltage is also measured. This step will be performed for each ITM and the beamsplitter.

- With the recycling mirror and end test masses realigned, the interferometer is locked and the coil current calibration is transferred to the ETM coil drivers as well, noting the drive current which gives an equivalent readout signal. At this point a detailed transfer function may be taken between the ETM coil drive current readout and the strain signal recorded by DAQ over the observation frequency band.

Analysis of potential errors in this procedure will depend to some degree on details of the electronics implementation, but we can anticipate several contributions which are likely to dominate.

6.1.1. Initialization Errors

The primary measurement relies on accurately determining the pk-pk demodulator output over a full order of motion. We anticipate errors of order ±0.5% in this step (this measurement is dependent on the laser power, but it can be measured and normalized out if it is not stable enough). In addition, the calibration must be extrapolated in both frequency (from 10 to as high as 10,000 Hz) and in amplitude (from .01 N at 10 Hz for a full order of motion to 4×10^{-11} N for a 0.01 fm test signal at 100 Hz). We anticipate additional errors of order ±0.5% in transferring the calibration coefficient to the operating frequencies and amplitude.

LIGO DRAFT

6.1.2. Errors due to temporal variation and drift

Once measured and extrapolated to operating conditions, the primary calibration is subject to additional errors due to drift in several multiplicative factors, some of which are shown in Figure 46. Arguably the most variable factor depicted here is $\partial S_{AQ}/\partial X_{ETM}$, the interferometer plant transfer function, which depends on such variables as laser power, alignment, mode matching, detector quantum efficiency, RF tuning and local oscillator phase, and so on. By embedding continuous test signals it is possible to normalize out these variations 'on the fly' (along with variations in A_S, the strain readout conversion gain, and $\partial V_{ETM}/\partial S_{AQ}$, the loop controller compensation). Continuous measurement at two or three discrete frequencies (below, near and above the servo unity-gain point) should be adequate to normalize out fluctuations of these quantities in post-processing.

The transimpedance Z_c of the suspension coil driver current sensing output (including coil and line impedance, if they are not separately normalized) can fluctuate with temperature or component age, as can the conversion gain A_I of the readout, ADC and whitening filter. In principle each of these is externally accessible and might be separately tested, although if done often (more than once per 40 hours) the interruption could impact interferometer availability.

The coil/magnet force coefficient $\partial X_{ETM}/\partial I_c$ is difficult to monitor or track without returning to the invasive fringe-interpolation procedure outlined above. Errors in this quantity translate directly into misinterpretation of the amount of calibration force applied to the mirror. Three possible sources of variation in this coefficient are under consideration:

- Temperature or aging variation in the magnetization of the permanent magnet
- Temperature or aging variation in the geometry of the coil
- Spatial variation of the position of the magnet within the coil field

While averaging results of calibrations using the four test mass suspensions may help in reducing errors, it is worth noting that (at least in some scenarios) these systematic effects may be correlated between the different mirrors in an interferometer.

Preliminary estimates for some of the calibration error sources presented above are summarized in Table 18.

Table 18: Primary calibration error estimates.

Description	variable	init. error	est. drift (1 hr)	est. drift (40 hr)
Coil current readout impedance	Z_c	.05%	.1%	.5%
Coil readout conversion gain	A_I	.05%	.1%	.5%
ETM mass	M	.1%	N/A	N/A
Coil/magnet force coefficient	$\frac{\partial X_{ETM}}{\partial I_c}$	1%	.5%	2%

LIGO-DRAFT

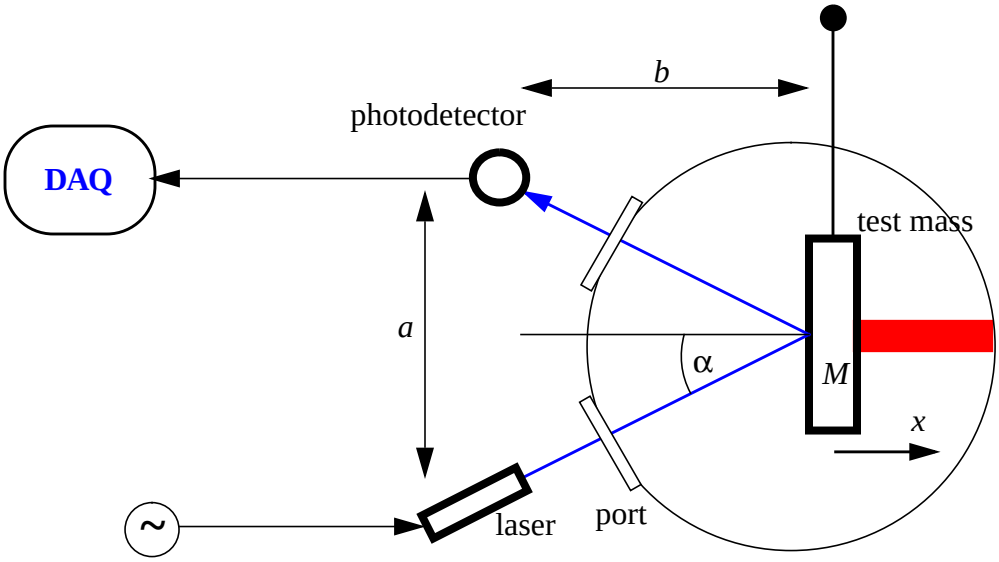

Figure 47: Schematic of a photon-recoil based calibration actuator.

6.2. Secondary calibration

The secondary calibration system will be based on photon recoil, as shown in Figure 47. The beam from a solid state laser will be directed through a BSC viewport onto the on-line ETM front surface. This laser will be chosen for high power (approximately 1W), high reflectivity on the ETM coating at the design angle of incidence, power stability, and capability for modulation; spatial and temporal mode quality are not significant factors except insofar as they affect power stability. A multimode fiber-coupled diode laser module has undergone some testing for this application; the immediately apparent problem is that the beam quality is very poor – too poor to be propagated ~20 m from the source to the test mass and back to the detector. We will be investigating using instead a diode-pumped Nd laser (YAG, or other host).

The laser power is modulated by a user-specified waveform. The incident power (and/or reflected power, if collected) will be monitored by an independent photodetector, whose output is initially (and at intervals) compared with the direct optical power reflected by the ETM. This calibration will normalize factors like the transmission of the vacuum viewport, reflectivity of the ETM, and beam sampler and attenuator transmissions. In this way the photodetector output voltage will be referenced to a calibrated optical power meter, which (in turn) will have NIST-traceable certification at the design wavelength. The error of this power meter's calibration and the stability of the photodetector's quantum efficiency over time are likely to be the dominant factors in the overall error budget.

LIGO-DRAFT

The recoil of the photons bounced off the mirror surface imparts momentum. If the incident angle is α the applied force is

$$F = 2\cos\alpha\frac{h\nu}{c}\dot{N}_\gamma \tag{4}$$

where $\dot{N}_\gamma$ is the number of photons hitting the mirror per time. Expressing the photon rate in units of the light power P yields

$$\dot{N}_\gamma = \frac{P}{h\nu} \quad \Rightarrow \quad F = 2\cos\alpha\frac{P}{c} \tag{5}$$

Treating the test mass as a simple pendulum and writing the light power as

$$P(t) = P_0 + P\cos\omega_c t \tag{6}$$

the displacement amplitude of test mass can be written as

$$x_c(\omega_c) = 2\cos\alpha\,\frac{P}{cM}\,\frac{1}{\omega_p^2 - \omega_c^2 + i\omega_p\omega_c/Q} \approx -2\frac{\cos\alpha\,P}{cM\omega_c^2} \text{ for } \quad \omega_c \gg \omega_p \tag{7}$$

where ω_p and Q are the angular frequency and Q of the pendulum. As an example we take a laser with power $P \approx 100\,\text{mW}$, an incident angle close to normal and a test mass of $M \approx 10\,\text{kg}$; the displacement amplitude at 100 Hz is then $x_c \approx 1.7\times10^{-16}\,\text{m}$.

The uncertainties of a photon actuator can be directly derived from eqn. (7); an estimate is presented in Table 19. The largest uncertainty will be in the measurement of the absolute laser power.

Table 19: Photon recoil calibrator error estimates.

Description	variable	nom. value	est. error + drift	unit
Laser power	P	1 – 100	2%	mW
Laser wavelength	λ	980	0.5%	nm
ETM mass	M	10.70	0.1%[a]	kg
Incident angle cosine	$\cos\alpha$	.7	0.1%	~
Vacuum viewport transmission	T	.99	0.2%	
Monitor photodiode responsivity	R	100	0.2%	V/W

a. Air buoyancy correction is of order 8 g.

This expected error is dominated by the specified accuracy of commercially available power meters used to calibrate the monitor photodetector, and may be improved substantially by use of more specialized detectors (for example, photodiodes exceeding 99% quantum efficiency are available for some laser wavelengths).

LIGO-DRAFT

6.3. CW sine calibration 'tracer'

During operation, the frequency response of the interferometer and its readout system is measured periodically by exciting either the photon recoil calibrator or ETM suspension test inputs with a swept sine, broadband pseudorandom sequence, or other waveform[1]. The transfer functions between injected suspension coil current, or modulated laser sample power, and readout signals are measured and converted into units of equivalent displacement using the previously measured calibration factor. This transfer function is stored with the interferometer data and used in data analysis to deconvolve the response function, converting the recorded signal time series into a representation of astrophysical strain (or other convenient basis).

However, comprehensive transfer function measurements will be invasive and detract from interferometer availability, so it is desirable to minimize the frequency and duration. It is also necessary to balance dynamic range against accuracy and dwell time per test. For example, in a standard "swept sine" frequency response test, the fractional precision in the transfer function $K(f)$ in a given frequency bin f_0 is limited by the random interferometer noise background with power spectral density $S_v(f_0)$ to

$$\frac{\delta K}{K_0}(f_0) \geq \frac{1}{V_t(f_0)}\sqrt{\frac{S_v(f_0)}{\tau}}$$

where $V_t(f_0)$ is the readout voltage resulting from the test signal and τ is the measurement dwell time. To achieve 1% fractional accuracy with a dwell time of 1 second per bin (17 minutes for a 1024-point sweep) requires an injected signal amplitude which exceeds the local background noise in a 1 Hz bandwidth by a factor of 100 (10^4 in power). Even if the dynamic reserve of the data acquisition (DAQ) system is deemed adequate, it is possible for this signal size to exceed the dynamic reserve limits of the LSC detection mode controls themselves at certain frequencies. Using a pseudorandom excitation to address multiple bins simultaneously will correspondingly increase the total energy added by the excitation, or take the same time for a fixed total added energy, to achieve a given total accuracy. As a result, it is desirable to minimize the frequency of detailed all-frequency transfer-function measurements.

As a result we propose to maintain three continuous sinusoidal test signals at different frequencies throughout operation. The frequencies will be chosen below, near and above the unity-gain frequency of the L_- control loop (approximately 50 Hz, 300 Hz and 800 Hz), and simultaneously monitor the coil current at each frequency along with the response in the strain signal. Post-recording (or on-line) data processing will include a procedure to evaluate the transfer function between coil current monitor and strain readout S_{AQ} at each probe frequency, and use the result to update the form of the most recent swept-sine transfer function measurement according to the parametric formulation discussed above.

The amplitudes of these CW calibration tones will add insignificant signal power compared to, for example, thermally driven suspension wire resonances. As an illustrative example, coherent integration of a test probe signal whose power just equals the broadband interferometer background

1. For example, a test waveform tailored to the measured spectral density of the interferometer noise will permit higher overall measurement accuracy with less injected energy and/or less downtime per measurement.

LIGO-DRAFT

noise power integrated over the adjacent 100 Hz bandwidth will yield a 1% measurement of the transfer function in 100 seconds, which we expect to be much shorter than the time over which readout parameters vary significantly. The actual level, and thus convergence time to the specified accuracy, will be adjusted to accommodate the observed rate and magnitude of change in the interferometer transfer function.

LIGO-DRAFT

APPENDIX 1 SEISMIC EXCITATION MODEL

In Figure 48 we show a block diagram of the ground noise propagation model. The inputs to the model are horizontal and vertical displacements of the ground measured at the LIGO sites. The following inputs are added together in the ground noise model to determine motion of the pendulum suspension point:

- measured ground displacement noise, propagated through displacement-to-displacement transfer functions of the seismic isolation stacks
- estimates for stack drifts based on upper limits of drifts measured in the 40 m prototype
- tilts of the building foundation due to vacuum loading, propagated through tilt-to-displacement transfer functions of the stacks
- tilts due to thermal deformation of the foundation, propagated through tilt-to-displacement transfer functions of the stacks
- measured ground tilt noise, propagated through tilt-to-displacement transfer functions of the seismic isolation stacks

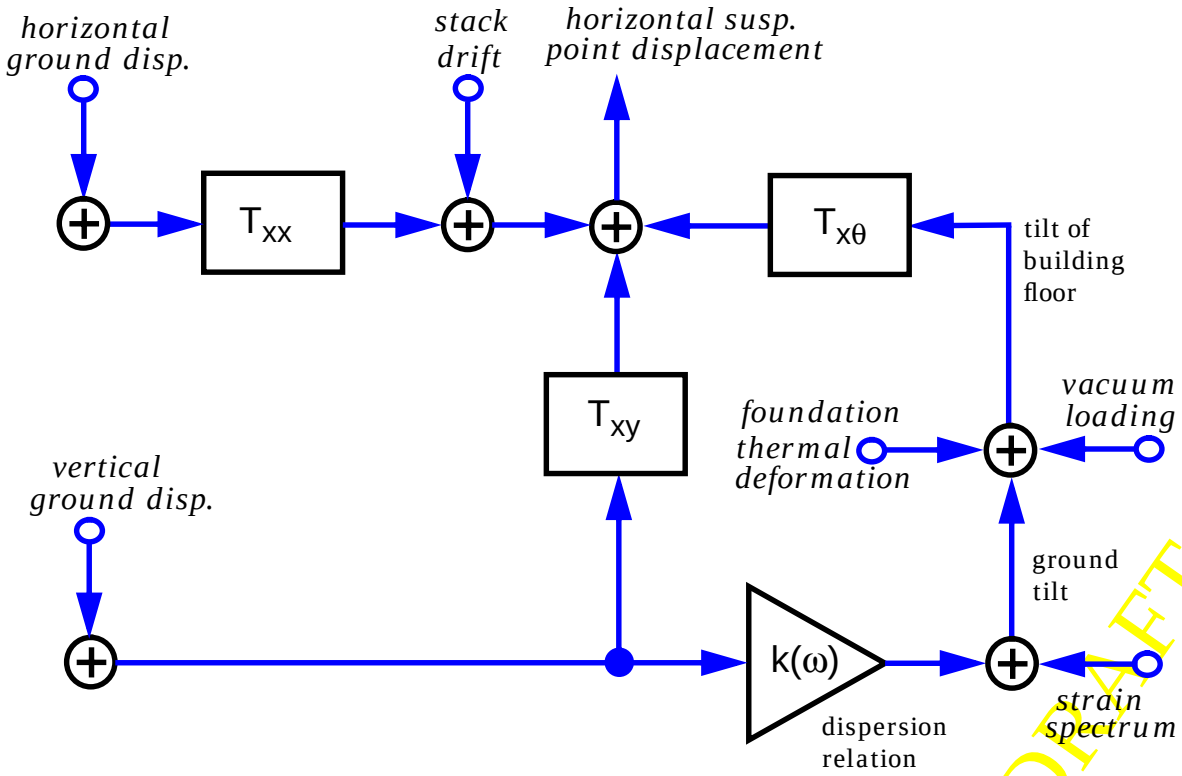

Figure 48: Schematic block diagram of ground noise propagation model. T_{ij} are the stack transfer functions relating the j-th degree of freedom at the bottom of the stack to the i-th degree of freedom at the top. Not shown, but included in the model, is the vertical suspension point displacement resulting from all the inputs.

LIGO DRAFT

The ground noise motion propagated through a stack transfer function model is assumed to be the motion of the suspension point of a particular optic, e.g. the recycling mirror, in an inertial coordinate system. The motions of the other optics of the interferometer and thereby their relative displacements along the optic axes are correlated at each frequency, f, by

$$S_{x_2x_2}(f) = J_0\left(2\pi f \frac{\Delta x}{v}\right) \tag{8}$$

where J_0 is a zeroth order Bessel function, $\Delta x = x_1 - x_2$ is the distance between two optics at positions x_1 and x_2, respectively, and v, the velocity of the seismic wave, is given by [2]

$$v = 450 + 1900 \exp\left(-\frac{f}{2\ \text{Hz}}\right)\ \text{m/sec} \tag{9}$$

In Figure 49 we show the ground noise spectrum, the displacement of the suspension point for a single optic and the relative displacements of two optics 13 m apart (e.g. RM and ITM), all in the horizontal direction.

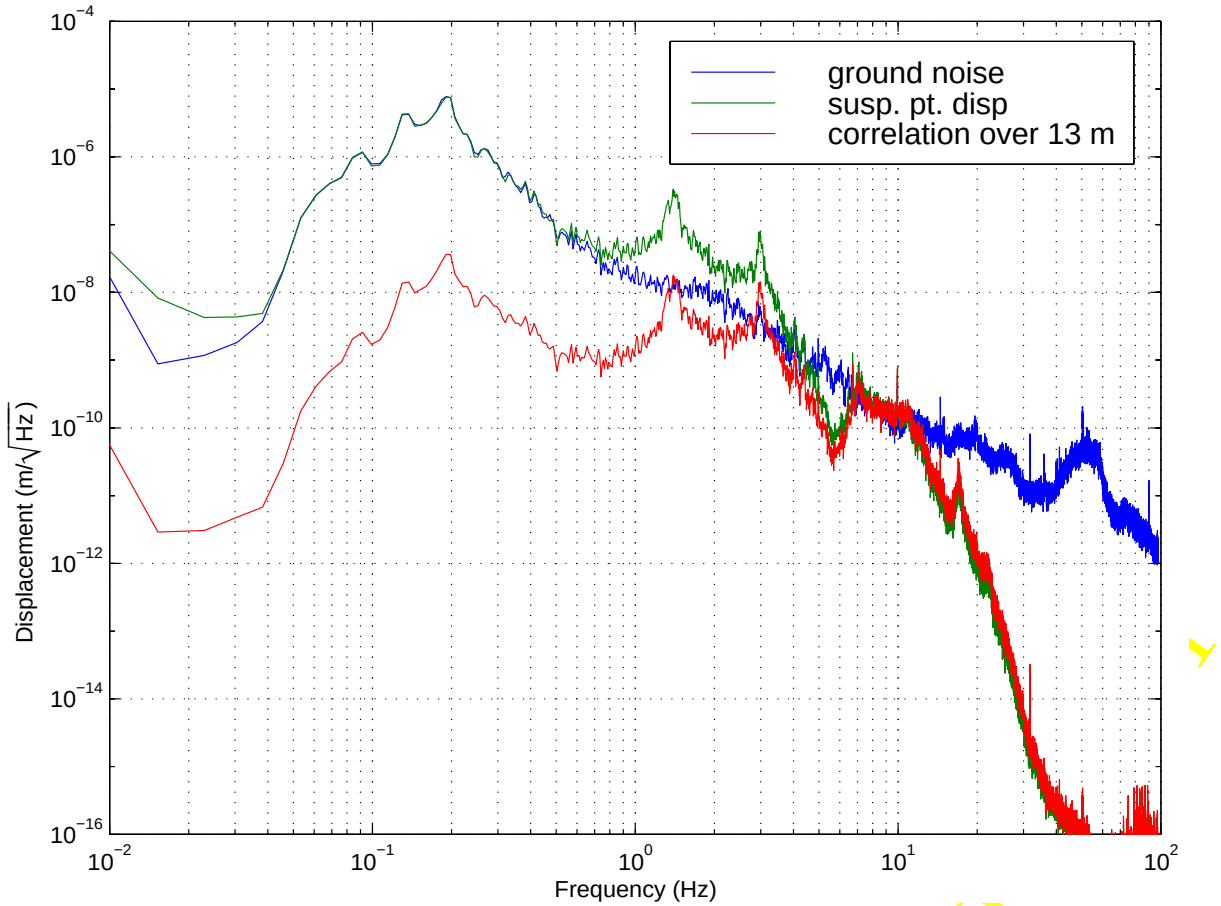

Figure 49: Amplitude spectral density of (i) the horizontal ground noise from a "noisy" 600 second time series measured at the LA site (blue); (ii) the motion of a single optic's suspension point calculated by propagating the ground noise through the horizontal-to-horizontal transfer function of the isolation stack (green); and (iii) the relative motion of the suspension points of two optics placed 13 m apart as give by the correlation model of eqns. (8) and (9) (red).

APPENDIX 2 SERVO EQUATIONS

A block diagram of the length-laser frequency control system for the interferometer is shown in Figure 50. The optical plant matrix, $\hat{P}$, is determined by the interferometer parameters; the controller matrix, $\hat{C}$, has dimensions of volts per volt and is designed to meet gain and phase requirements stated above; the pendulum block, p, comprises a pendulum (*pend*) with a resonant frequency of 0.74 Hz (corresponding to the Large Optics Suspension or LOS), a 1 Hz/40 Hz pole/zero pair included in the suspension controller (*Csus*) to meet noise requirements at 40 Hz and a constant gain factor (dm/dV) with dimensions of meters per volt.

Since we have four detection "ports" and five inputs to the optical plant, is a 5×4 matrix with dimensions of volts per meter or volts per Hertz (for the frequency noise input). The conversion of watts (light power in the interferometer) to volts at the demodulator output assumes a photodetection scheme with a 900 Volts/Watt efficiency. Referring to the servo system of Figure 50, we can write the generalized matrix equations. The residual length fluctuations are

$$\vec{L}_{res} = \hat{M}^{-1} \cdot (p \cdot \vec{L}_{seis} + \vec{L}_{therm} + p \cdot \hat{C} \cdot \vec{S}_{shot}) \tag{10}$$

where

$$\hat{M} = \hat{1} - p \cdot \hat{C} \cdot \hat{P} \tag{11}$$

Similarly, the signals at the detection ports are

$$\vec{S}_{res} = \hat{A}^{-1} \cdot (p \cdot \hat{P} \cdot \vec{L}_{seis} + \hat{P} \cdot \vec{L}_{therm} + \vec{S}_{shot}) \tag{12}$$

where

$$\hat{A} = \hat{1} - p \cdot \hat{P} \cdot \hat{C} \tag{13}$$

LIGO-DRAFT

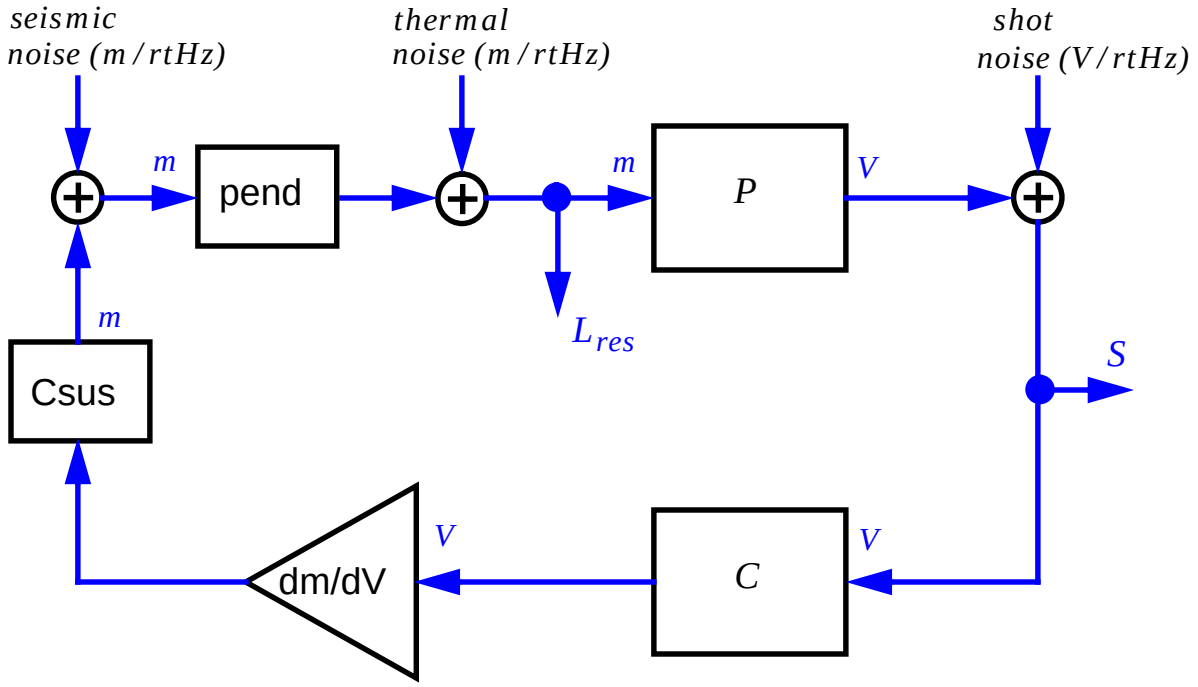

Figure 50: Block diagram of a multiple input multiple output (MIMO) servo system. The servo blocks P and C are m × n matrices, the noise inputs are n × 1 vectors and the residual outputs L_{res} and S are m × 1 vectors.

Since the plant matrix is mostly block-diagonal with little interaction between the common-mode and differential-mode degrees of freedom, it is convenient to model the common-mode and differential-mode loops independently. This assumes that the plant is the only coupling mechanism, which is valid provided the mirror actuation can be done without cross-couplings.

➤ Differential modes

The matrices $\hat{P}$ and $\hat{C}$ above are reduced to 2 × 2 for the differential-mode only. The noise inputs and residual outputs are 2 × 1 vectors. The optical plant matrix for the differential degrees of freedom is

$$\hat{P} = \begin{bmatrix} P_{Lm2AQ} & P_{lm2AQ} \\ P_{Lm2PQ} & P_{lm2PQ} \end{bmatrix} = \begin{bmatrix} \dfrac{-9.6\times10^{11}}{1+s/(2\pi\times 91\ \mathrm{Hz})} & 4.72\times10^{5} \\ \dfrac{-7.3\times10^{9}}{1+s/(2\pi\times 91\ \mathrm{Hz})} & 6.20\times10^{7} \end{bmatrix} \mathrm{V/m} \qquad (14)$$

The control matrix, also 2 × 2, can be written as

LIGO-DRAFT

$$\hat{C} = \begin{bmatrix} C_{11} & C_{12} \\ C_{21} & C_{22} \end{bmatrix} \tag{15}$$

and the matrices $\hat{M}$ and $\hat{A}$ are

$$\hat{M} = \begin{bmatrix} 1 - p \cdot (P_{11}C_{11} + P_{21}C_{12}) & p \cdot (P_{12}C_{11} + P_{22}C_{12}) \\ p \cdot (P_{11}C_{21} + P_{21}C_{22}) & 1 - p \cdot (P_{12}C_{21} + P_{22}C_{22}) \end{bmatrix} \tag{16}$$

$$\hat{A} = \begin{bmatrix} 1 - p \cdot (P_{11}C_{11} + P_{12}C_{21}) & p \cdot (P_{11}C_{12} + P_{12}C_{22}) \\ p \cdot (P_{21}C_{11} + P_{22}C_{21}) & 1 - p \cdot (P_{21}C_{12} + P_{22}C_{22}) \end{bmatrix} \tag{17}$$

A block diagram of the differential-mode servo is shown in Figure 51. There are two main loops, the *Lm* and *lm* loops, respectively, but they are coupled via the plant elements P_{lm2AQ} and P_{Lm2PQ}. Referring to Figure 51, the matrix elements of $\hat{P}$ and $\hat{C}$ in eqn. (16) are:

$$\begin{array}{llll} P_{11} = P_{Lm2AQ} & P_{12} = P_{lm2AQ} & C_{11} = CLm & C_{12} = C_{12} \\ P_{21} = P_{Lm2PQ} & P_{22} = P_{lm2PQ} \quad \text{and} & C_{21} = C_{21} & C_{22} = Clm \end{array} \tag{18}$$

For simplicity we would like to design the controllers such that the matrix elements C_{12} and C_{21} are zero. This scheme was presented in [13] and has a shortcoming: the shot noise at the relatively noisy recycling cavity pick-off port couples to the gravitational-wave signal via the matrix element P_{lm2AQ}. This is evident from eqns. (12) and (17). The residual signal $S_{11} = S_{AQ}$ is the gravitational-wave readout. Shot noise at the pick-off, S_{shot}^{PQ}, appears in S_{AQ} via the matrix element

$$(\hat{A}^{-1})_{12} = p \cdot (P_{Lm2AQ}C_{12} + P_{lm2AQ}Clm) \tag{19}$$

When $C_{12} = 0$, the coupling of shot noise at the pick-off to S_{AQ} is further amplified by the gain in the *lm* controller, *Clm*. In the results presented in [13], the gain above 40 Hz in the *lm* loop was severely limited to ensure that the gravitational-wave signal induced by shot noise at the pick-off remained below the allowed SRD/10 level. To circumvent this problem, we design C_{12} such that $(\hat{A}^{-1})_{12} \approx 0$, effectively minimizing this coupling. Ideally,

$$C_{12} = -\left(\frac{P_{lm2AQ}}{P_{Lm2AQ}}\right)Clm \tag{20}$$

which would remove all constraints on the *Clm* gain at all frequencies. Unfortunately, such a fine tuning of C_{12} would require that the optical plant remain very stable over long periods of operation. We design the servo system assuming a 5% variability of the optical plant.

Defining

LIGO-DRAFT

$$GLm = p \cdot P_{11} \cdot C_{11} = p \cdot P_{Lm2AQ} \cdot C_{Lm}$$
$$GLm = p \cdot P_{22} \cdot C_{22} = p \cdot P_{lm2PQ} \cdot C_{lm} \qquad (21)$$

and

$$\varepsilon_1 = \frac{P_{12}}{P_{11}} = \frac{P_{lm2AQ}}{P_{Lm2AQ}}$$
$$\varepsilon_2 = \frac{P_{21}}{P_{22}} = \frac{P_{Lm2PQ}}{P_{lm2PQ}} \qquad (22)$$

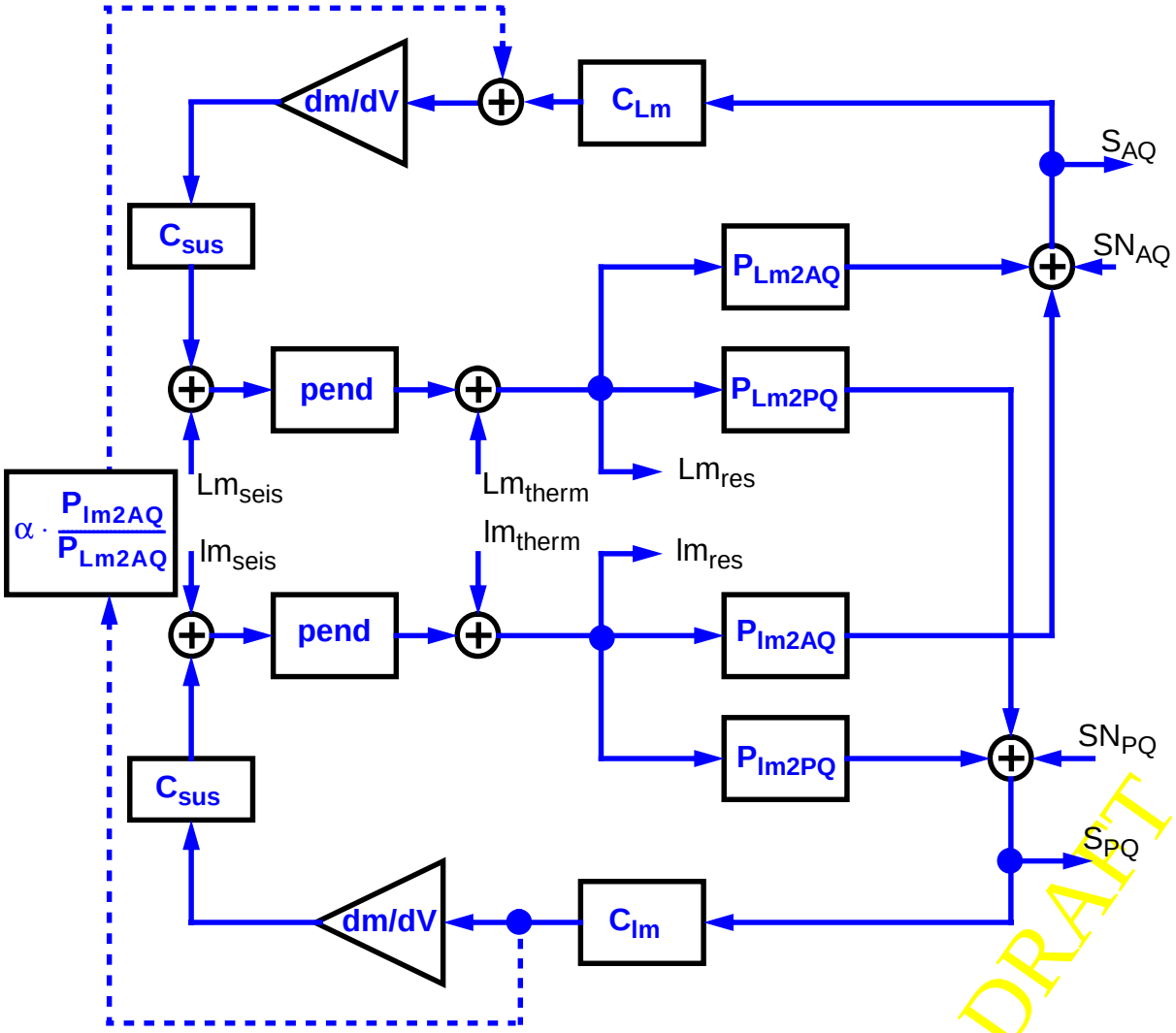

Figure 51: Differential-mode servo block diagram. Seismic, thermal and shot noise inputs lead to residual length deviations, Lm_{res} and lm_{res}, and to residual signals, S_{AQ} and S_{PQ}. Also shown is an control signal from the *lm* loop to added to the *Lm* loop. This is to suppress coupling of shot noise from the recycling cavity pick-off to the anti-symmetric port. The parameter α is a measure of the temporal variability of the plant ratio P_{lm2AQ}/P_{Lm2AQ}.

LIGO-DRAFT

and taking the off-diagonal terms of the control matrix to be

$$\begin{aligned} C_{12} &= \alpha \cdot Clm \\ C_{21} &= 0 \end{aligned} \tag{23}$$

where α is a parameter we set according to the expected plant variability over time, we invert $\hat{M}$ to get the closed loop gain of the system:

$$\hat{G}_{CL} = \hat{M}^{-1} = \frac{1}{\Delta}\begin{bmatrix} 1 - Glm & \varepsilon_1 GLm + \alpha Glm \\ \varepsilon_2 Glm & 1 - GLm - \alpha\varepsilon_2 Glm \end{bmatrix} \tag{24}$$

where

$$\Delta = det(\hat{M}) = (1 - Glm)(1 - GLm - \alpha\varepsilon_2 Glm) - \varepsilon_2 Glm(\varepsilon_1 GLm + \alpha Glm) \tag{25}$$

➤ Common modes

The optical plant is sensitive to three common-mode degrees of freedom: the arm cavities common length, δLp, the recycling cavity average length, δlp, and frequency fluctuations on the incoming laser light, δf. These are most conveniently written as phase fluctuations

$$\begin{aligned} \Phi &= k \cdot Lp = \frac{2\pi}{c}\delta f \cdot Lp + \frac{2\pi}{\lambda} \cdot \delta Lp \\ \phi &= k \cdot lp = \frac{2\pi}{c}\delta f \cdot lp + \frac{2\pi}{\lambda} \cdot \delta lp \end{aligned} \tag{26}$$

In this basis $\hat{P}$ and $\hat{C}$ are once again 2×2 matrices and the noise inputs and residual outputs are 2×1 vectors. The optical plant matrix is

$$\hat{P} = \begin{bmatrix} P_{\Phi 2RI} & P_{\phi 2RI} \\ P_{\Phi 2PI} & P_{\phi 2PI} \end{bmatrix} = \begin{bmatrix} \dfrac{3.8 \times 10^3}{1 + s/(2\pi \times 0.77\ \text{Hz})} & \dfrac{23 \times (1 + s/(2\pi \times 2.9\ \text{Hz}))}{1 + s/(2\pi \times 0.77\ \text{Hz})} \\ \dfrac{-90}{1 + s/(2\pi \times 0.77\ \text{Hz})} & \dfrac{-0.27 \times (1 - s/(2\pi \times 0.86\ \text{Hz}))}{1 + s/(2\pi \times 0.77\ \text{Hz})} \end{bmatrix} \text{ A/rad} \tag{27}$$

We write

$$\begin{aligned} P_{\Phi 2RI} &\equiv P_\Phi & P_{\phi 2PI} &\equiv P_\phi \\ P_{\phi 2RI} &\equiv \varepsilon_3 P_\Phi & P_{\Phi 2PI} &\equiv P_\phi / \varepsilon_4 \end{aligned} \tag{28}$$

where

$$\begin{aligned} \varepsilon_3 &= 0.006\,(1 + s/(2\pi \times 2.9\ \text{Hz})) \\ \varepsilon_4 &= 0.003\,(1 - s/(2\pi \times 0.86\ \text{Hz})) \end{aligned} \tag{29}$$

LIGO-DRAFT

A block diagram of the common-mode servo is shown in Figure 52. Seismically driven fluctuations of the interferometer lengths, Lp_{seis} and lp_{seis}, and fluctuations of laser frequency, δf, are converted into two error signals, S_{RI} and S_{PI}. There are three main loops: the interferometer length loops, *Lp* and *lp*, which actuate on the interferometer mirrors via length control inputs in the suspension controllers; and the frequency suppression loop which comprises two actuation paths, one pulls the mode cleaner length via the mode cleaner SOS controller and the other adds a signal to offset the error point of the mode cleaner frequency detection system. The laser frequency follows the mode cleaner length at all frequencies above a few hertz via the VCO.

In an exercise similar to that for the differential-mode servo equations we can write a matrix solution for the residual phase noise

$$\begin{bmatrix}\Phi\\ \phi\end{bmatrix}_{res} = \frac{1}{\Delta}\begin{bmatrix} 1 - Glp - \varepsilon_3\frac{lp}{Lp}(GMCl + GMCao) & \varepsilon_3(GLp + GMCl + GMCao) \\ \dfrac{Glp}{\left(\varepsilon_4 + \frac{lp}{Lp}(GMCl + GMCao)\right)} & 1 - (GLp + GMCl + GMCao)\end{bmatrix}\begin{bmatrix}\Phi\\ \phi\end{bmatrix}_{in} \tag{30}$$

where

$$\Delta = (1 - GLp + GMCl + GMCao)\left(1 - Glp - \varepsilon_3\frac{lp}{Lp}(GMCl + GMCao)\right) - \frac{\varepsilon_3}{\varepsilon_4}(GLp + GMCl + GMCao)\left(Glp + \varepsilon_4\frac{lp}{Lp}(GMCl + GMCao)\right) \tag{31}$$

$$\begin{bmatrix}\Phi\\ \phi\end{bmatrix}_{in} = \begin{bmatrix}\frac{2\pi}{\lambda}\delta Lp_{seis} + \frac{2\pi Lp}{c}\delta f_{IOO} \\ \frac{2\pi}{\lambda}\delta lp_{seis} + \frac{2\pi lp}{c}\delta f_{IOO}\end{bmatrix} \tag{32}$$

and

$$\begin{aligned} Glp &= P_{\phi 2PI}\cdot C_{lp}\cdot C_{sus}\cdot dmdV\cdot pend\cdot\frac{2\pi}{\lambda} \\ GLp &= P_{\Phi 2RI}\cdot C_{Lp}\cdot C_{sus}\cdot dmdV\cdot pend\cdot\frac{2\pi}{\lambda} \\ GMCl &= P_{\Phi 2RI}\cdot C_{MCL}\cdot MCleng\cdot\frac{2\pi Lp}{c} \\ GMCao &= P_{\Phi 2RI}\cdot C_{MCAO}\cdot dmdV_{SOS}\cdot pend_{SOS}\cdot MCaddoff\cdot\frac{2\pi Lp}{c} \end{aligned} \tag{33}$$

LIGO DRAFT

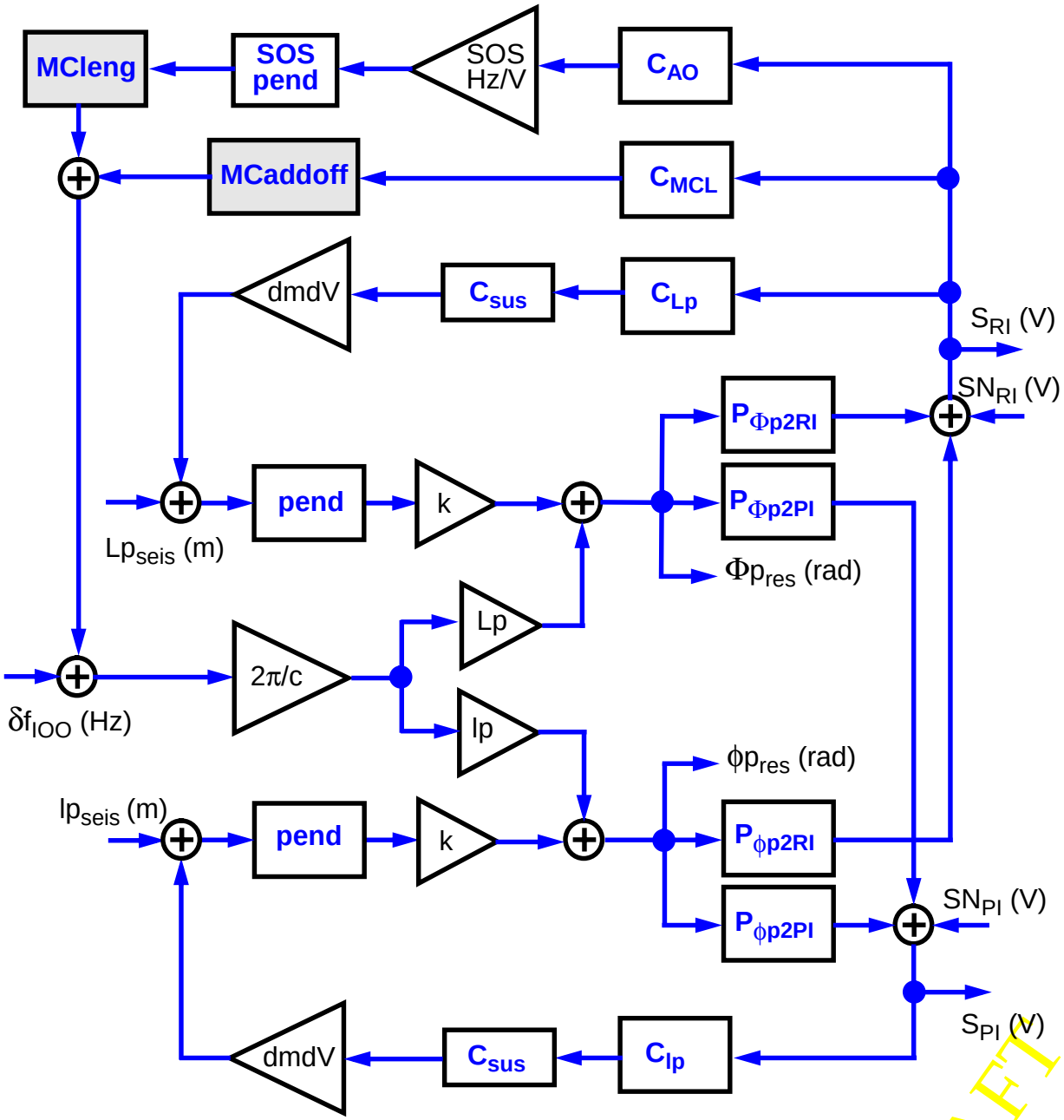

Figure 52: Common-mode servo block diagram. Seismically-driven motion of the suspension points, frequency noise from the IOO mode cleaner and shot noise at the sensors (inputs) lead to residual phase deviations, Φp_{res} and ϕp_{res}, and to residual signals, S_{RI} and S_{PI} (outputs). The shaded blocks, MCleng and MCaddoff, contain the dynamics of the closed loop response of the mode cleaner servo.

LIGO DRAFT

APPENDIX 3 OVERALL FREQUENCY STABILIZATION TOPOLOGY

The frequency noise requirements in LIGO are stringent enough that a frequency suppression factor of 200 dB at 100 Hz and 150 dB at 1 kHz is necessary to suppress the frequency noise of the 10 W laser. The frequency stabilization uses a nested loop control topology. This is illustrated in Figure 53.

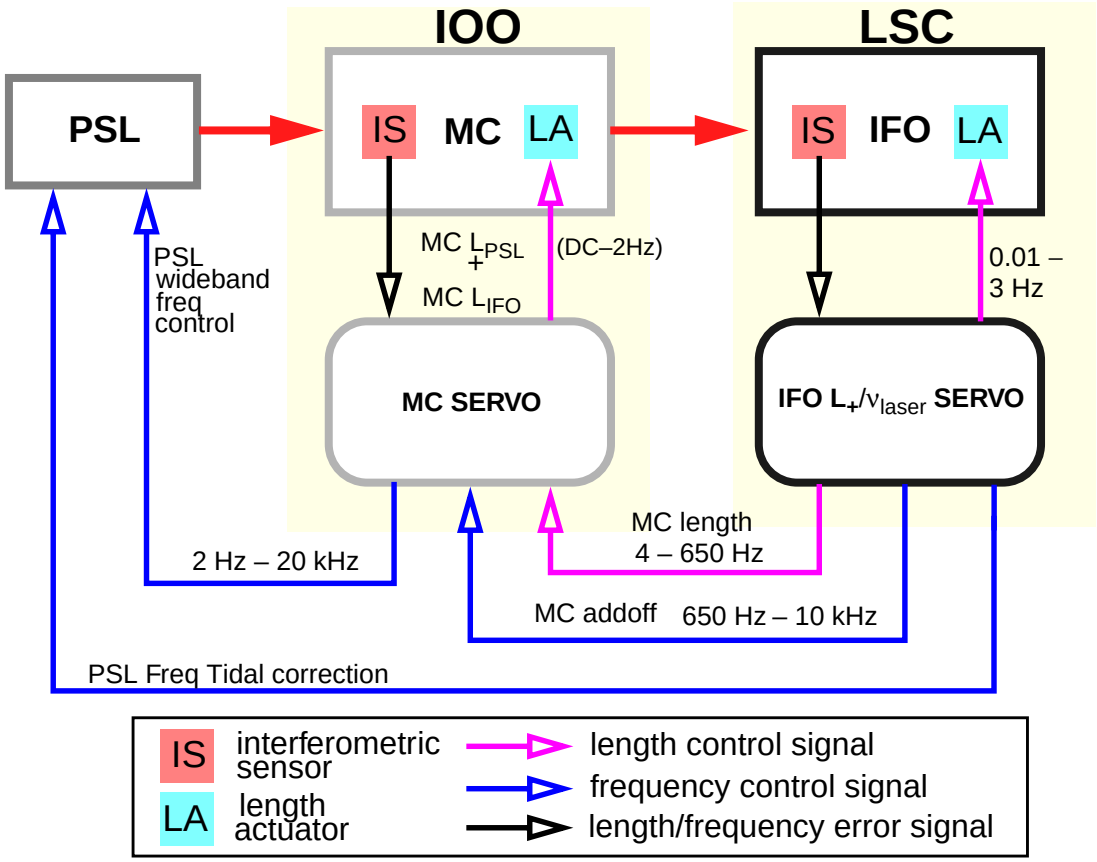

Figure 53: Laser Frequency Control — global configuration.

For the purposes of the interferometer length/frequency control design, it is necessary to calculate the dynamic response of the mode cleaner frequency output to the LSC control inputs, specifically, the mode cleaner length and mode cleaner additive offset (see shaded blocks in Figure 30). These response functions, calculated using a Simulink® model of the mode cleaner servo [12], are shown in Figures 54 and 55.

LIGO-DRAFT

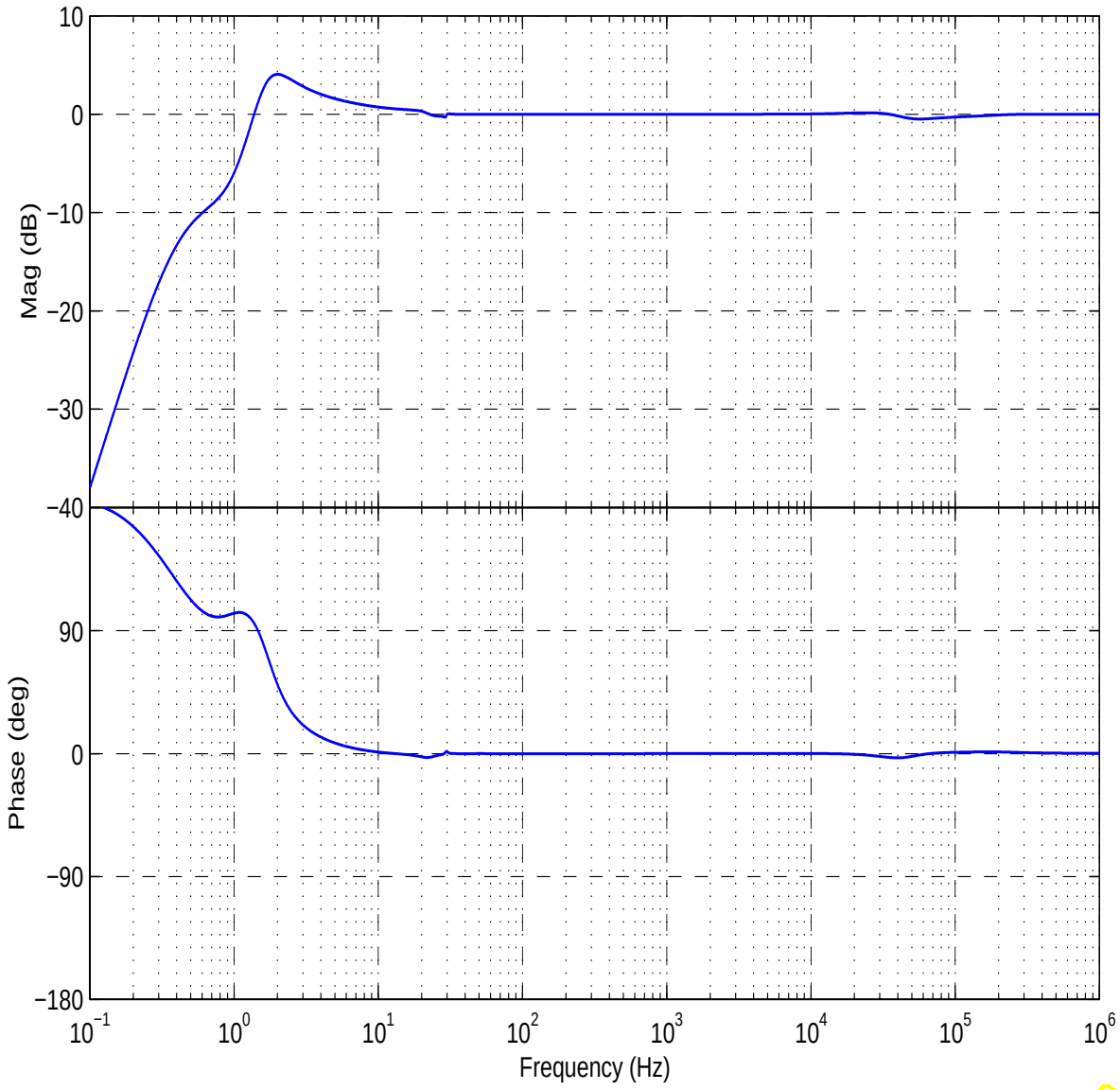

Figure 54: Closed loop response of the mode cleaner frequency output to an interferometer signal added to the mode cleaner length control signal.

LIGO-DRAFT

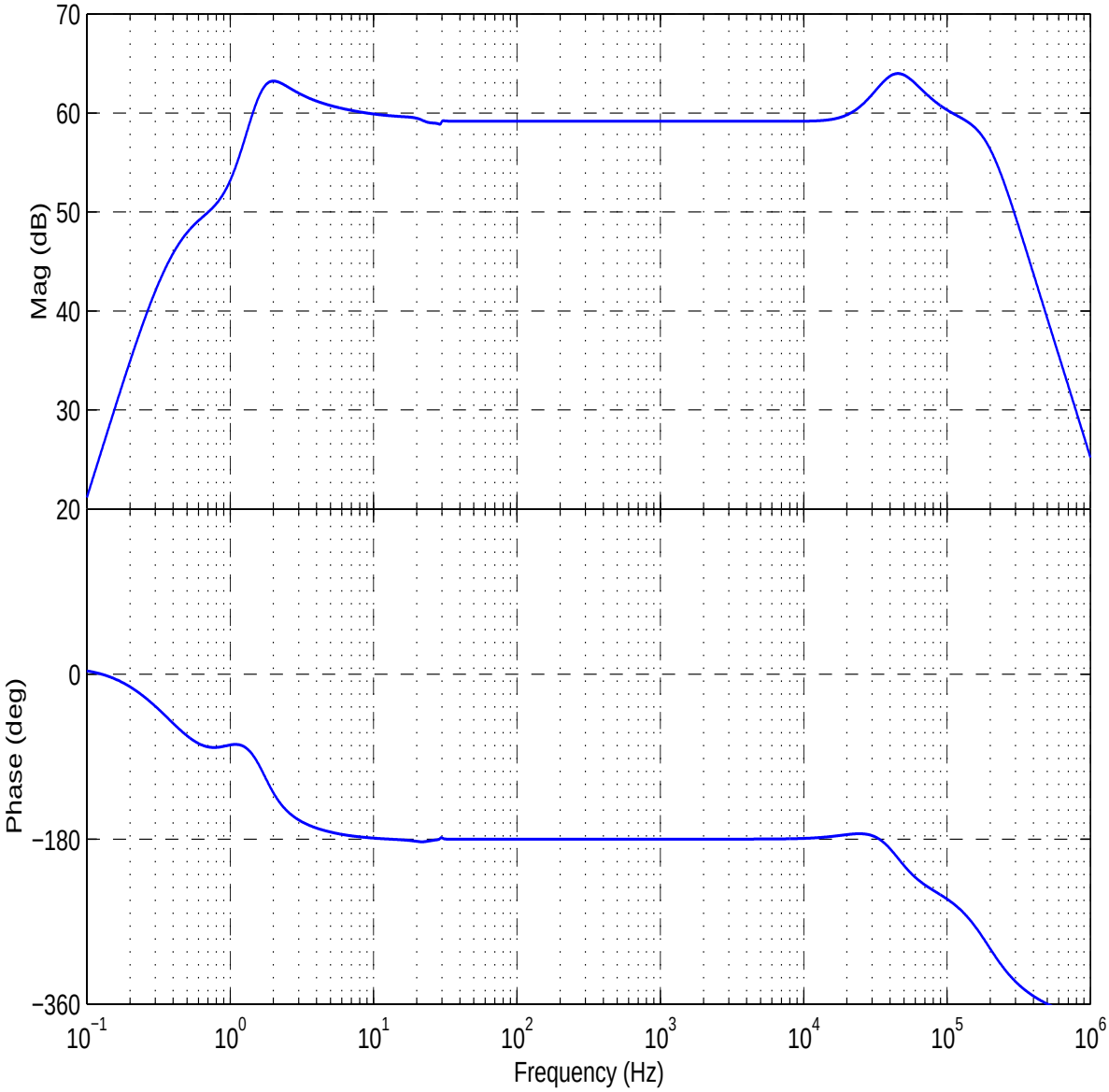

Figure 55: Closed loop response of the mode cleaner frequency output to an interferometer signal added to offset the mode cleaner error point.

LIGO-DRAFT

APPENDIX 4 COUPLING OF SHOT NOISE AT THE PICK-OFF TO THE GRAVITATIONAL-WAVE SIGNAL

The parameter α, defined in eqn. (23), is a measure of the plant variability. When $\alpha = 0$, the off-diagonal control element is zero; if $\alpha = 0.9$, we assume that the optical plant is variable at the 10% level; or if $\alpha = 0.99$, the optical plant varies by 1%. In Figure 56 we plot the coupling of shot noise at the pick-off to the gravitational-wave signal for different values of α, using the *lm* controller of Figure 24. The *lm* controller was designed assuming a plant variability of 3 to 5%.

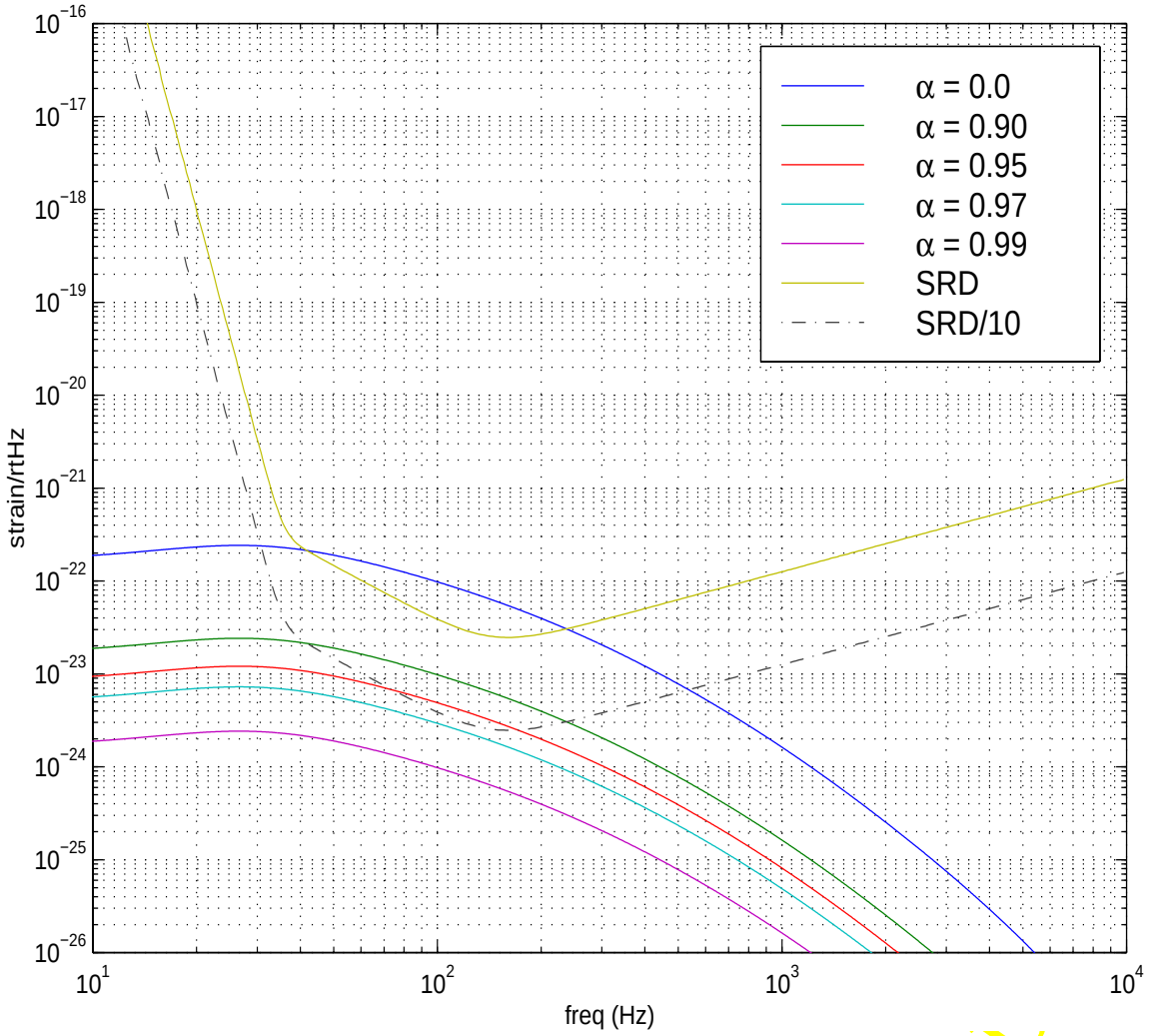

Figure 56: Coupling of shot noise at the pick-off to gravitational-wave signal for different values of α. The SRD and SRD/10 curves are plotted for comparison.

LIGO-I

APPENDIX 5 PNI DIGITAL SERVO TEST

A1.1 Aims of the PNI Digital Servo Test

A prototype for the LIGO digital L_m servo has been tested using the Phase Noise Inteferometer (PNI) at MIT. The questions addressed in this experiment were: (a) What are the noise contributions of the digital servo elements and associated analog circuitry? (b) How can a digital servo be used to lock a suspended inteferometer? (c) What is the phase noise of the PNI using the digital servo compared to that measured using the existing analog servo? (d) Can inteferometer diagnostics be implemented in the digital domain?

A1.2 The Digital Servo Prototype

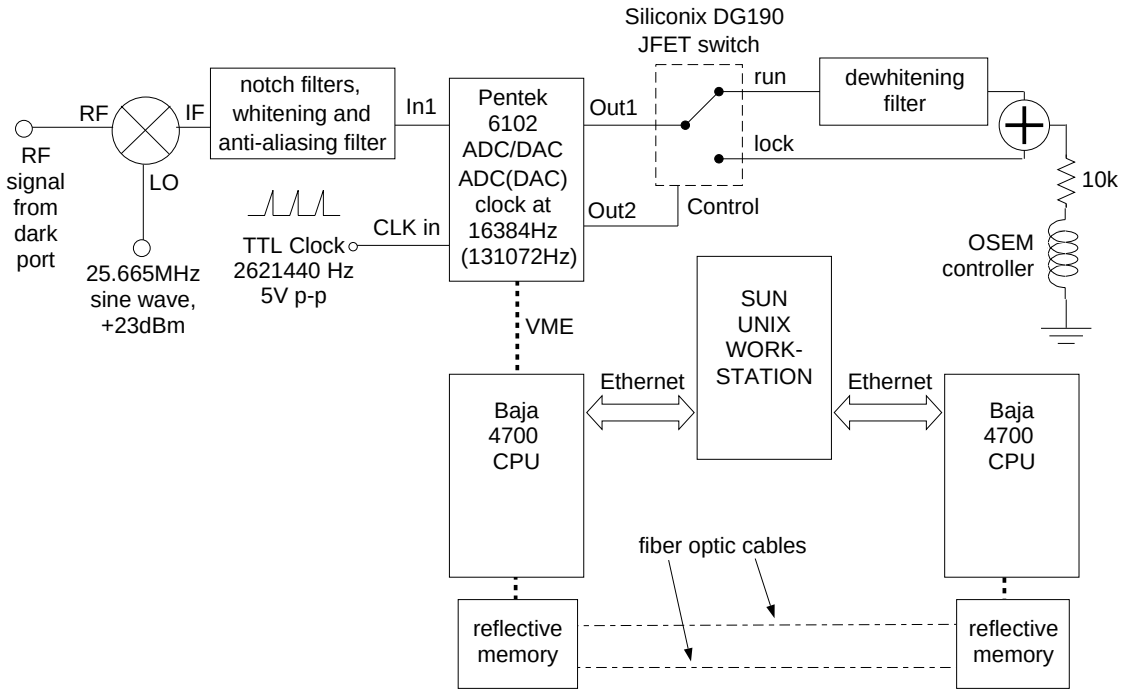

Figure 57: **Schematic diagram of the elements of the digital L_m servo prototype.**

Figure 57 is a schematic of the elements of the digital L_m servo prototype. The RF signal from the PNI dark port photodiode is de-modulated. The demodulated signal first passes through a set of 3 notch filters at 25.5MHz, 24.66MHz, and 36.99MHz. The resultant signal is fed to a whitening filter (WF), consisting of a zero at 15Hz and a pole at 150Hz. Its function is to boost the power spectral density (PSD) at frequencies above 150Hz so that the PSD at all frequencies up to the Nyquist frequency is within the dynamic range of the ADC. Following the whitening filter is a 5 pole Butterworth low pass anti-aliasing filter at 6.5kHz. The output of the anti-aliasing filter is fed to an input of a Pentek 6102 ADC/DAC. The sampling rate of the ADC is 16384Hz, so the Nyquist frequency is 8192Hz. The digitized signal is IIR filtered. The design of this IIR filter is a central part of this experiment.

LIGO-I

The output of the IIR filter is passed to a DAC converting at 131072Hz. The DAC clock rate is as high as possible to minimize time delay in converting from digital to analog. The resulting analog signal is fed to a 2-way JFET switch, which, in 'run mode', passes the signal through a dewhitening filter (DWF) to a summing junction or, in 'lock mode', passes the signal straight to the summing junction. The dewhitening filter consists of two poles at 15Hz and two zeros at 150Hz. Its function is to boost the response of the digital servo to signals at low frequencies (below 15Hz) for good phase noise performance. It was found necessary to bypass the DWF to increase the servo dynamic range when locking the PNI.

The output of the summing junction passes through a 10kΩ resistor which converts the voltage output of the summing junction to a current suitable for driving the PNI OSEM controllers.

A1.3 Dynamic Range of the Pentek 6102 ADC/DAC

The noise level measured at the output of the DAC was measured to be ~10μV_{rms}/rt(Hz) with no digital IIR filter. The noise level was measured in two ways. Firstly a fixed frequency sine wave was injected at the input of the ADC and the PSD of the noise far from the carrier frequency was measured. Secondly noise from a source filtered to mimic the PNI output when locked was injected ADC input, the filter also including a narrow notch at 2kHz - the PSD of the noise in this notch is the noise contribution of the ADC/DAC. The noise level appeared to be the same using the two methods. There was a weak dependence on the ADC sampling frequency; the noise level dropped roughly as the inverse square root of the sampling frequency.

Over the full bandwidth (8kHz) of the ADC, the noise level is 0.9mV_{rms}. This noise level is much higher than that resulting from quantization noise at the ADC - the excess noise may result from analog circuit components on the ADC chip itself, which is a charge storage (CDAC) device. The full scale voltage at the DAC output is 5V, so the voltage dynamic range of the Pentek ADC/DAC is ~4.5 orders of magnitude.

A1.4 The Digital Servo in the 'Lock' and 'Run' Modes

Switching between lock and run mode was performed by changing the value of a global variable defined in the real-time software running the digital servo. A low priority task polled the value of the external variable, and whenever a change in its value was detected, two changes were made at the Pentek ADC/DAC (refer to Figure 57). The first change was to alter the value of the voltage at the Out2 port of the DAC from 0V to 5V. As a result, the dewhitening filter, which in lock mode had been bypassed, was switched in to the servo. The second change was to alter the filter coefficients used in the digitally implemented filter, so that a different digital filter was used in the lock and run modes.

Initially, a relay was used to switch the dewhitening filter in to the circuit. We found out that the relay was too slow; switching transients on a timescale of ~18ms were severe enough to throw the inteferometer out of lock. Subsequently, a fast JFET switch was employed, eliminating the switching transient problem.

LIGO-DRAFT

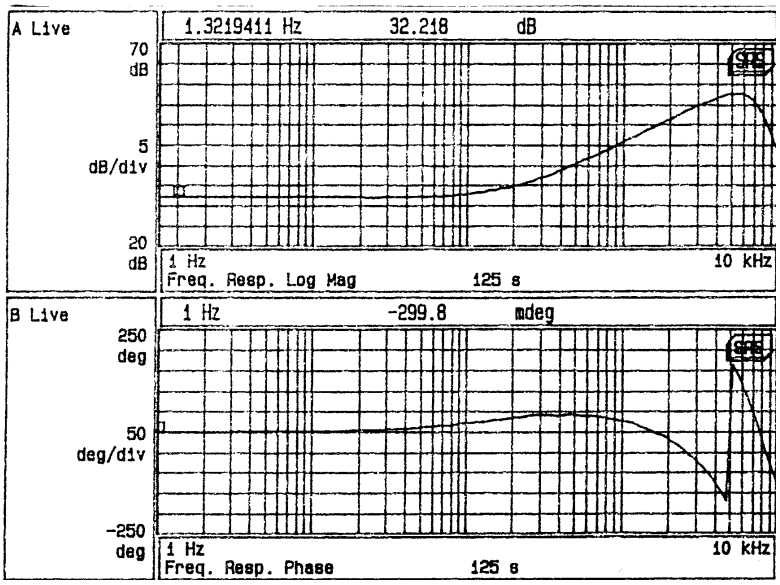

Figure 58: Open loop gain of the servo electronics in lock mode. The electronics consists of the whitening filter in series with the digital filter. The dewhitening filter is bypassed. The upper plot shows the amplitude of the circuit response to a swept sine wave at its input, the lower plot shows the phase.

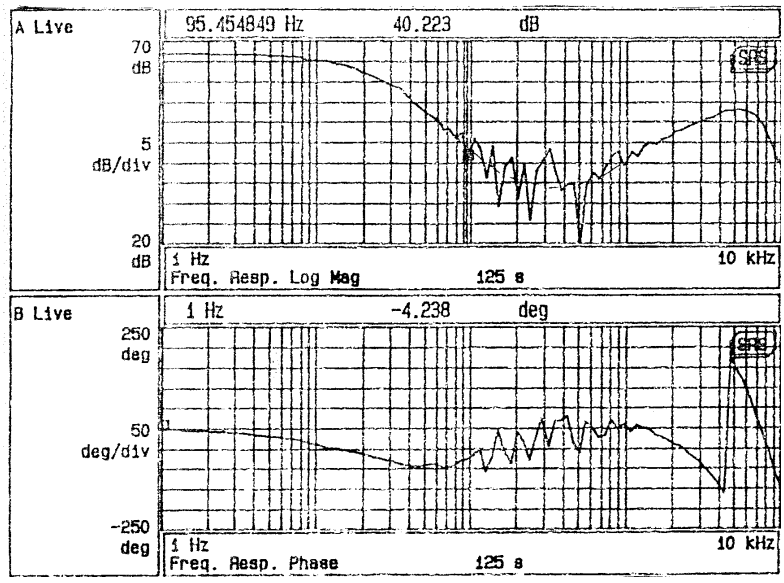

Figure 59: Open loop gain of the servo electronics in run mode. The electronics consists of the whitening filter, digital filter, and dewhitening filter in series. The upper plot shows the amplitude of the filter response to a swept sine wave at the input, the lower plot shows the phase at the electronics output relative to the input. The noise at ~400Hz is from the amplitude of the sine wave input being too small at this frequency.

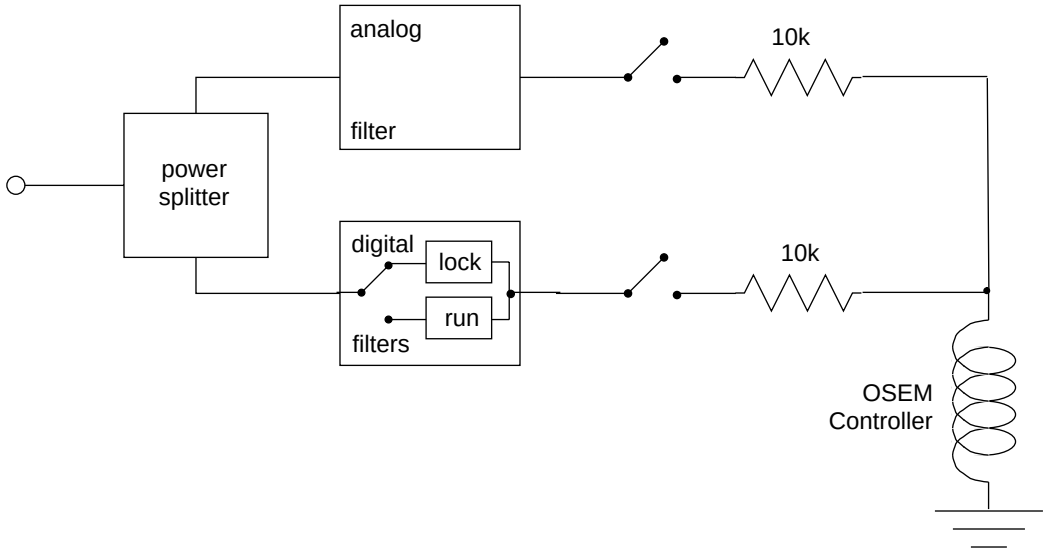

Figure 60: Schematic diagram of the arrangement of analog and digital servo elements for locking the PNI.

A1.5 Locking the Inteferometer

Two different locking techniques were used during the PNI test. At first, the inteferometer was locked using the digital servo in ‘lock’ mode. However, this method of locking proved difficult. The machine took too long to lock; about 20 minutes per lock acquisition. Possible reasons for the difficulty was limited dynamic range and restricted bandwidth of the digital servo. With more time it is possible that we could have changed the lock acquisition filter to improve the dynamic range. However, the voltage dynamic range of the digital servo is limited by the ADC noise to ~4 orders of magnitude.

For the purposes of the test a different locking procedure was adopted. Refer to Figure 60. The inteferometer was first locked using the analog servo. The digital servo electronics were connected in parallel with the analog servo, with the digital servo in ‘lock’ mode. When the analog servo was disconnected the PNI remained locked. Finally, the digital servo was switched into ‘run’ mode. This method takes advantage of the high dynamic range and bandwidth of an analog servo for locking. It was very robust; locking the PNI and connecting the digital servo usually took less than a minute. The PNI routinely stayed locked for more than 30 minutes with the digital servo in ‘run’ mode.

A1.6 Closed Loop Gain

Refer to Figure 57. The ‘primary’ Baja4700 processor connected by the VME backplane to the Pentek ADC/DAC was linked through a reflective memory ring to a ‘secondary’ Baja4700 processor in a different VME rack. This arrangement is a prototype for the reflective memory loop proposed for LIGO diagnostics. The secondary Baja4700 processor received interrupts every 1/16 of a second from the primary processor. On receiving an interrupt, the secondary Baja downloaded

LIGO-DRAFT

1024 data points to a reflective memory address space. These 1024 data points were read by the primary Baja processor and added to the digital signal in the servo loop. In addition, the data from the servo loop was written by the primary Baja processor to a second address space in reflective memory and subsequently read by the secondary processor.

Using this technique, a diagnostic to measure the closed loop gain of the servo was implemented in software. The resulting closed loop gain measurement is shown in Figure 61. These results are in agreement with measurements made using an SRS SR760 fft box.

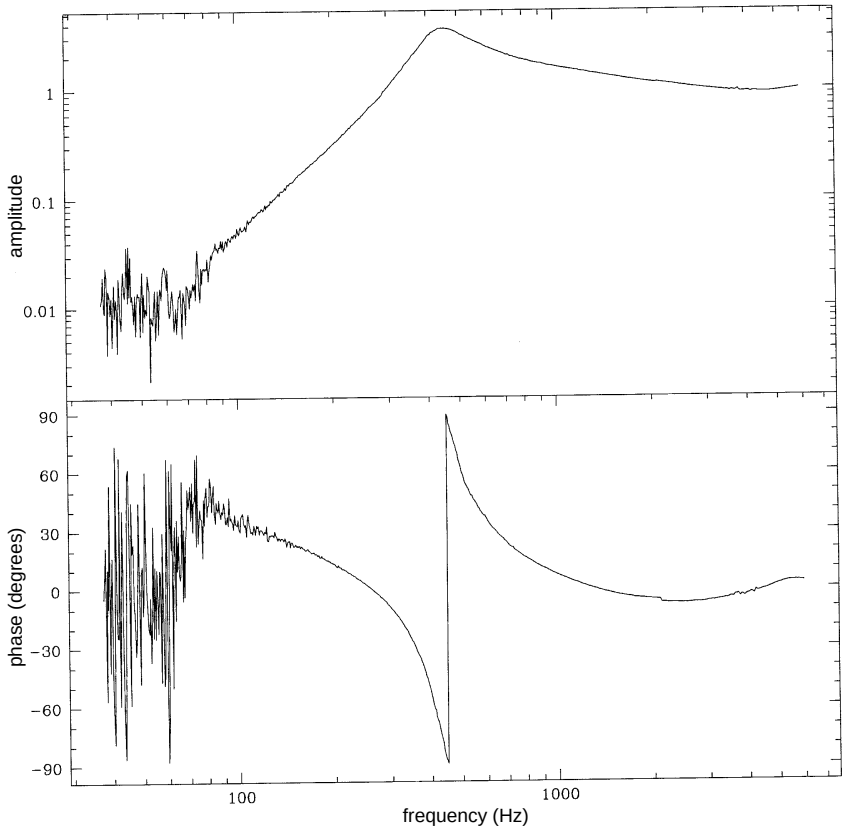

Figure 61: Closed loop gain of the PNI incorporating the digital servo in run mode. The upper plot shows the amplitude closed loop response to a swept sine wave injected digitally using a prototype for the LIGO diagnostic software. The lower plot shows the phase.

A1.7 Phase Noise

The phase noise of the PNI was measured using an HP3562A signal analyzer. Figure 62 shows the phase noise of the PNI with the digital servo, compared with the best phase noise obtained with the analog servo.

The most important noise source that was eliminated before this phase noise was obtained was high frequency noise in the whitening filter. This noise was eliminated by adding a 22nF capacitor

LIGO-D

to ground before the first amplification stage. This change yielded a factor of 2 improvement in the phase noise in the frequency range 100-300Hz. A second improvement involved increasing the gain in the whitening filter in run mode and decreasing the value of the series resistance (see Figure 1) at the servo electronics output such that the overall size of the signal at the servo output remains the same as before the adjustment, but more of the dynamic range of the ADC is used. This modification eliminated some narrow lines seen in previous measurements. We nave no explanation for narrow line series above 3kHz in the digital spectrum or the higher broadband noise level above 1kHz.

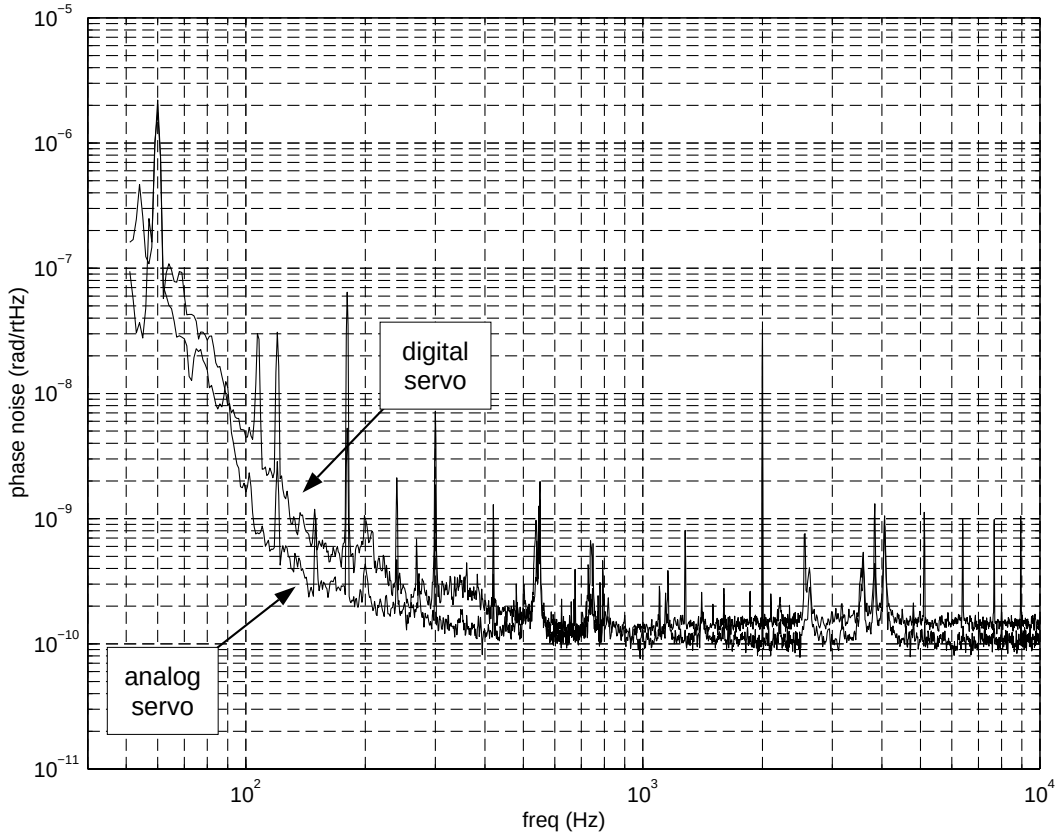

Figure 62: Comparison of the phase noise of the PNI with the analog and digital servos

A1.8 Conclusions

- The PNI digital servo experiment has shown that a digital servo can run a LIGO prototype inteferometer, yielding phase noise results comparable with those for the analog servo.
- The PNI digital servo experiment has successfully demonstrated application of software diagnostics similar to those being written for LIGO.
- The dynamic range of the digital servo using the Pentek 6102 ADC/DAC is ~4.5 orders of magnitude.
- The digital servo was used successfully to lock the PNI, however a more efficient locking method was locking the machine using an analog servo with a high dynamic range and bandwidth, and subsequently switching to a digital servo for data-taking.

LIGO-DRAFT

APPENDIX 6 REFERENCES

[1] Eric Ponslet, Hytec, Inc., *private communication*.

[2] LIGO-L960019-00-F: *memo on local seismic correlations*.

[3] Bill Kells, *private communication*.

[4] LIGO-T960058-03-I: *Length Sensing and Control System Design Requirements*.

[5] LIGO-E950018-00-E: *LIGO Science Requirements Document*.

[6] LIGO-T970091-00-D: *Determination of the Wedge Angles for the Core Optics Components.*

[7] LIGO-T970191-03-D: *Test Mass Transmissibilities*.

[8] LIGO-T980029-01-D: *Effect of Beamsplitter Vibration Resonance Excitation on the Optically Sensed Cavity Length*.

[9] LIGO-T970158-06-D: *Large Optics Suspension Final Design (Mechanical System)*.

[10] LIGO-T960103-00-D: *ASC: Environmental Input to Alignment Noise*.

[11] LIGO-T960139-00-D: *Shot Noise Sensitivity of the Length Control Error Signals*.

[12]LIGO-T970218-01-D: *Mode Cleaner Length/Frequency Control Desig*n.

[13]LIGO-T970122-00-D: *Length Sensing and Control Subsystem Preliminary Design*.

[14]LIGO-T970007-00-D: *Modeling the Performance of an Initial LIGO Detector with Realistically Imperfect Optics*.

[15]LIGO-E950099-04-E: *Core Optics Components Requirements*.

[16]LIGO-T970098-00-D: *Proposed Interferometer Parameters*.

[17] LIGO-T970084-00-D: *Frequency Response of the LIGO Interferometer.*

LIGO-DRAFT